Parabolic Trough Solar Collectors: Design for Increasing Efficiency

by

Stacy L. Figueredo

Submitted to the Department of Mechanical Engineering
in partial fulfillment of the requirements for the degree of

Doctor of Philosophy in Mechanical Engineering

at the

MASSACHUSETTS INSTITUTE OF TECHNOLOGY

June 2011

Author . . . .
Department of Mechanical Engineering
May 2011

Certified by. . . . .
Alexander H. Slocum
Pappalardo Professor of Mechanical Engineering
Thesis Supervisor

Accepted by . . . .
David E. Hardt
Chairman, Department Committee on Graduate Students

Parabolic Trough Solar Collectors: Design for Increasing Efficiency

by

Stacy L. Figueredo

Abstract

Parabolic trough collectors are a low cost implementation of concentrated solar power technology that focuses incident sunlight onto a tube filled with a heat transfer fluid. The efficiency and cost of the parabolic trough collector designs is influenced by structural stiffness, choice of materials, assembly tolerances, mirror cleanliness and wear. Current performance estimates of solar trough optical field efficiencies are 54.2% [1]. The goal of this research is to identify general methods and specific design concepts for achieving increased collector efficiency.

This thesis has investigated improvements in the design of a parabolic trough module by looking first at the overall structural concept of the collector to reduce complexity while maintaining structural stability under wind loading conditions. In the process of evaluating the feasibility of one such concept, a monolithic reflector panel with a mirror film front surface, details related to the mirror surface efficiency were investigated. At the panel-structure to mirror interface, surface roughness of the underlying structural backing was studied to understand performance effects on the mirror film surface that would make one backing material potentially more suitable than another would. In this case it was found that three materials tested: gel-coated fiberglass, rolled aluminum, and rolled steel were all similarly effective when compared to a more expensive mirrored aluminum backing material. When looking at the integration of the larger structural changes with the factors that affect surface reflectivity of parabolic mirrors, it became apparent that contamination of the surfaces and cleaning were major factors in reduced module effectiveness. Given that the conceptual development of the structure is ongoing, research into contamination factors and potential cleaning solutions were considered in such a way that panel cleaning solutions could be integrated into the trough module design from the start. A vortex generator cleaning concept, which uses V-shaped extruded forms to create vortices over a mirror panel in the presence of flow over the surface, was tested as a passive cleaning solution.

Thesis Supervisor: Alexander H. Slocum
Title: Pappalardo Professor of Mechanical Engineering

Acknowledgments

This thesis would not have been possible without the help and support of friends, family and colleagues. I would like to extend my deepest thanks to:

- Thesis committee members:

  - Professor Alexander Slocum for the opportunity to be part of his lab, for being an advisor that is open to new ideas, willing to listen and always supportive, and for making research fun.

  - Professor George Barbastathis for being a great advisor and mentor from the very beginning of my MIT career and for his generosity and dedication as my committee member.

  - Professor Alexander Mitsos for his detailed comments and suggests as a committee member which helped to shape and refine this project.

- Fellow members of the Precision Engineering Research Group (PERG), and in particular:

  - Gerald Rothenhofer for motor controller and labview support for wind tunnel measurements as well as last minute control system troubleshooting.

  - Keith Durand, for welding and vacuum layup help, latex templates and one awesome hammock.

  - Folkers Rojas for PIV processing and simulation suggestions.

  - UROP students Jennifer Hammond and Levon Thomas for running many of the test iterations for this project.

- Professor Bahaa Ibraheem Kazem, University of Baghdad, MIT visiting scientist and collaborator on cleaning concept development.

- MITEI Research Sponsors, and Lorenzo DiVita in particular for his thoughtful suggestions on the project focus and development details.

Contents

List of Figures

11

14

List of Tables

Chapter 1

Motivation and Outline

World demand for energy is projected to more than double by 2050 and to more than triple by the end of the century. Incremental improvements in existing energy networks will not be adequate to supply this demand in a sustainable way. Finding sufficient supplies of clean energy for the future is one of society's most daunting challenges [19, 20]. Neither the issues of increased demand for fossil fuels nor the alternative energy solutions proposed, such as solar and wind power generation, are new to this decade. More than thirty years ago, in his article regarding solar electric power generation, E. L. Ralph stated "Probably the only reason there is no crisis declared is that for the immediate time and short term future, fuel is plentiful and cheap. As long as this is the case, the earth will be looted and stripped of these resources because everyone is enjoying the power [21]." What remains to be realized are the engineering details to make such technologies effective despite fluctuations in environmental inputs and attractive regardless of fossil fuel prices. This idea necessitates the broader investigation of solar collector designs, from conceptual improvements in structural frame design and mirror surface details, as well as integrated cleaning technology and installation methodology.

1.1 The Demand for Large Scale Solar Energy Research

Sunlight provides by far the largest of all carbon-neutral energy sources. More energy from sunlight strikes the Earth in one hour (4.3×10^{20} J) than all the energy consumed on the planet in a year (4.1×10^{20} J). We currently exploit this solar resource through solar electricity — a \$7.5 billion industry growing at a rate of 35–40% per annum [1]. However, current solar energy generation remains only a sliver of current production. A survey conducted by the Stanford Research Institute found that in 1957 there were seventeen solar furnace installations in the United States, including parabolic troughs ranging from 36 inches to 120 inches as published in the first volume of Solar Energy [22]. These installations, supported by the availability of parabolic mirrors from military searchlights, were in some cases capable of temperatures on the order of 3500°C. Of the 2.01×10^{10} MWh generated in the US in the first half 2008, only about 4.26×10^{5} MWh or 0.02% of that was from solar thermal and photovoltaic sources [1]. Worldwide use of solar energy remains a small percentage of overall production, seen in Figure 1-1 as only a part of non-hydroelectric renewable energy. This reservoir of energy, which on the human timescale is inexhaustible, presents an attractive replacement for fossil fuels [23]. As with most energy systems, overall system efficiency determines to a large extent the quantity of output that will eventually compensate for fixed costs. In addition, finding inexpensive methods to reduce materials, installation, and maintenance costs will reduce cost of ownership of the system.

Solar collector shipments have increased to the current levels of approximately 4.5 million square feet in 2005 (Figure 1-2) [23]. Peaks in solar energy demand coincide with general peaks in energy prices, however, there has been evidence that the funding for research is not entirely influenced by oil prices [17]. The Department of Energy Office of Basic Energy Research awarded 27 Projects a total of \$22.7 million dollars for capture conversion and use of solar energy. A recent report on the basic needs for solar energy utilization, from the Department of Energy stated "The key challenge in

By Source, 1970-2006
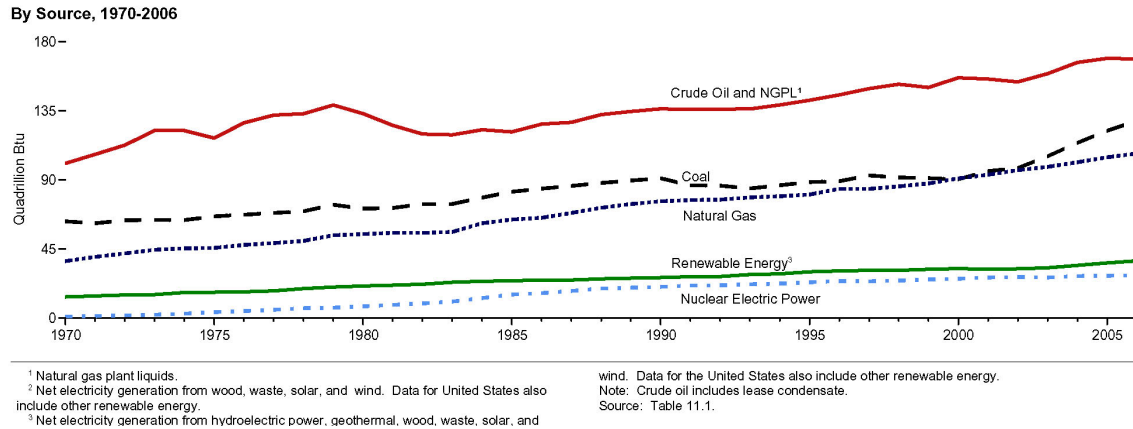
Figure 1-1: World Primary Energy Production by Source (1 quadrillion Btu= 2.93×10^8 MWh) [1].

solar thermal technology is to identify cost-effective methods to convert sunlight into storable, dispatchable thermal energy." This panel also stated that research "should lead to the cost reductions required to make this technology competitive with conventional electricity production within five to ten years, assuming fossil fuels remain at present prices." Despite recent spikes of \$150/barrel, the U.S. energy sector has delivered an average price of electricity in June 2008 of 10.33 cents per kilowatt-hour (Figure 1-3) [1]. To reach such a competitive market price, future solar research will have to focus on cost reduction and efficiency for mass production [24, 25, 26, 27].

1.2 Motivation for System Level Error Management and Efficiency Improvements

Where the potential for system level improvements may be made is worth noting. Analysis of solar energy systems, both from cost and efficiency perspectives, has been conducted to a large extent on both individual modules of collector subsystems, as seen in Table 1, as well as for entire arrays of solar collectors [17, 18, 28, 29].

Among the many areas identified by a study from Pitz-Paal et al, as having cost reduction potential for parabolic trough concentrator modules are [2]:

- Multilayer plastics and innovative structures

23

Figure 58. Solar Collector Shipments and Trade
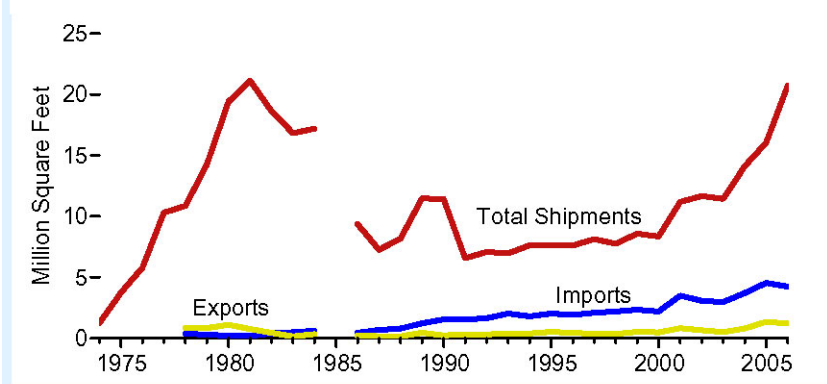
Notes: • Data were not collected for 1985. • Shipments include all domestically manufactured collectors plus imports.

Shipments of solar collectors grew strongly in the 1970s and reached a peak of 21 million square feet in 1981. Uneven performance was recorded over the next decade, followed by a mild upward trend during the 1990s and a bump up in 2001 and again in 2004 through 2006. Imports reached a record level of 4.5 million square feet in 2005.

Figure 1-2: Solar Collector Shipments and Trade [1].
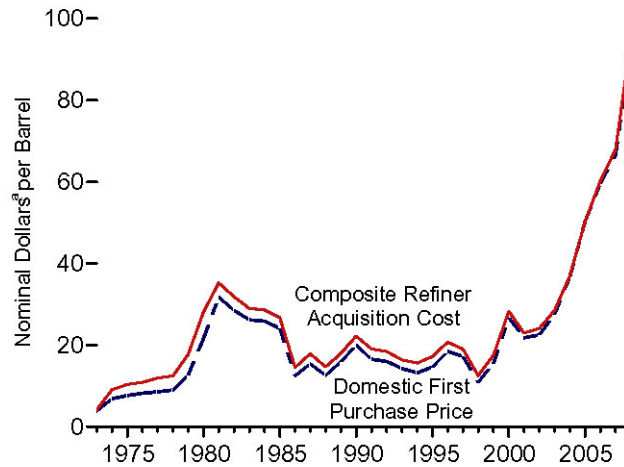
Figure 1-3: Petroleum Prices [1].

Table 1.1: Cost Breakdown for 1.5 meter aperture paraboloids [17].

Table 1. Cost breakdown for paraboloids of 1·5 meter aperture; 16 per module* (85% reflectivity; 80° rim angle)

Item	$/M²	% of Total
Materials		
Aluminum shell	13.00	25.5
Steel framing for shell	1.40	2.7
Gears and motors	6.50	12.7
Other	1.50	2.9
Labor and overhead to manufacture	3.80	7.4
Pipe supports	7.10	13.9
Foundation	6.60	12.9
Tracking mechanisms and controls	3.70	7.3
Transportation	1.10	2.2
Installation of modules	4.00	7.8
Contingency (5% of the above)	2.40	4.7
Total	$51.10	100.0%

*Costs in 1972 dollars are per square meter of projected area, exclusive of the absorber.
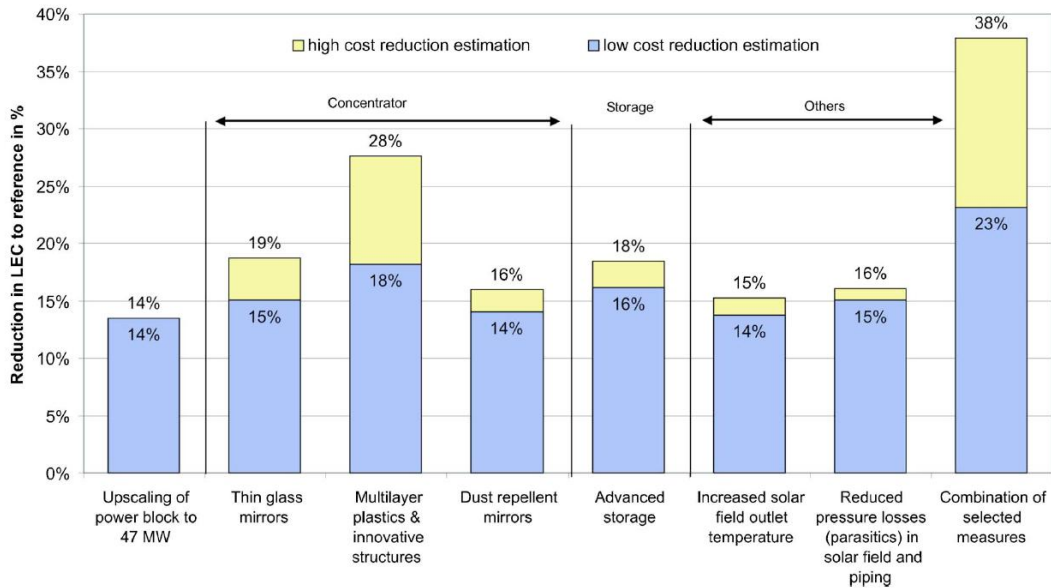
Fig. 5 Cost-reduction potential of different innovations for parabolic trough DSG systems compared to parabolic trough DSG reference system. For all systems shown in this figure, a 47 MW$_e$ single power block unit was assumed.

Figure 1-4: Cost reduction potential of parabolic trough innovations [2].

- Thin glass mirrors

- Dust repellent mirrors

These subareas of efficiency improvements form the focus of this thesis, both because they represent potential efficiency improvements of up to 28% reduction in LEC and because they represent a broad cross-section of scales in the field of precision machine design. In particular, thin glass mirrors, or lightweight mirror technologies allow for smaller actuator sizing, and represent potential LEC reductions of $15\% - 19\%$. Multi-layer plastics and innovative structures present the opportunity to reduce part count, provide stiffer and more precise mirror alignment, while also lessening actuator load through lighter concentrator supports. Such improvements in structures represent a potential savings of $18\% - 28\%$ reduction in LEC alone. Thirdly, dust repellent mirrors, or more generally, mirror surfaces with self-cleaning technologies integrated into the design itself, present opportunities to reduce LEC $14\% - 16\%$ in large part by improving efficiency of the mirror while reducing the cost of maintenance and cleaning. Additionally, the Pitz-Paal study suggested that increased solar field outlet temperatures and parasitic losses in solar field piping could contribute to realizing more affordable solar field arrays. Along this vein, this thesis evaluates areas where efficiency is affected by concentrator design from the component level of the collector module to the cleaning and maintenance of the collector. By evaluating each of these areas and presenting results for improvements, this thesis looks at system errors and efficiencies from large scale deformations, to surface level errors, to particle level contamination issues, all of which must come together for a competitive design to be realized.

1.3 Thesis Outline

This thesis began with the intent of improving the design of parabolic trough structural concepts, both to increase their efficiency in the field and to lower their cost of manufacturing and installation. Innovations in the direction of a monolithic structure

led to the need to investigate surface level specifications of mirror films and structural backing materials both in terms of surface roughness and durability. Evaluation of resulting structure and surface performance increasingly lead to the understanding that surface contamination and cleaning is a necessary component of the initial design process, and that if considered early in the design process, could be integrated into module concept itself. Details of this investigation both from a broad design perspective, and in details of parabolic trough specific issues are contained in the following chapters:

Chapter 2: Presented in this chapter is background information of relevant incoming solar characteristics which affect system performance as well as existing concepts for solar thermal installations, including details for module-level parabolic trough technologies.

Chapter 3: Problem identification and functional requirements of an improved parabolic trough solar collector are given, as well as references to relevant Nation Renewable Energy Lab performance and cost target tables.

Chapter 4: Support structure details are covered, first with respect to wind loading requirements according to ASCE (American Society of Civil Engineering) structural requirements. This outline for wind loading specifications is followed by details of a prototype 1/10th scale modle design, the subsequent wind tunnel testing, as well as resulting measurements of load on the monolithic panel structure.

Chapter 5: Mirror surface effects due to material selection for the structural backing surface are presented in this section. Details for mirror film surface roughness for a calibrated surface finish standard as well as for potential backing materials are provided. Surface reflectance information of a mirror film surface is given after particle jet erosion to understand the impact of surface degradation on performance.

Chapter 6: Contamination of reflective mirror surfaces on parabolic troughs can

drastically reduce performance with respect to theoretical mirror reflectivity. This section presents an outline for characterization of contamination particle size distribution and resulting performance reductions. Results of contamination studies with calibrated dust samples are provided along with resulting mirror efficiencies.

Chapter 7: Cleaning concepts which could be integrated into existing parabolic trough designs as well as new structural concepts are given in this section. Contamination results were used to focus on passive features in the form of vortex generators as a cleaning method. Results of flow simulations, particle image velocimetry studies, and surface cleaning effecting on efficiency are included in this section.

Chapter 8: Conclusions and recommendations for testing of cleaning concepts on larger trough panels are provided in this section, with an outlook for how the results from previous chapters may be used to increase efficiency of both parabolic trough systems in operation as well as for future installations.

Chapter 2

Background

As with most power systems, efficiency is the key to overall success. What begins as a perfect idea for a system is often chipped away by incremental losses until only a trickle of the original amount of power remains. Here we present an overview of system level errors and their relative effect on solar concentrator performance.

2.1   Incoming Solar

In order to understand the amount of energy one can possibly harness from any solar plant, it is useful to understand the inherent limitations of the sun as a source of energy. When modeled as an ideal radiative source, known as a blackbody, the spectral distribution of solar output follows that of the Planck distribution for a source at approximately 5800K. Accordingly, the thermal emission spectra as a function of wavelength is of the form shown in Equation 2.1 [30].

$$B_\lambda(T) = \frac{C_1}{\lambda^5(e^{C_2/\lambda T} - 1)} \tag{2.1}$$

The first and second radiation constants are

$$C_1 = 2\pi h c^2 = 3.741 \times 10^{-16} W \cdot m^2 \tag{2.2}$$

and

$$C_2 = \frac{hc}{k} = 1.439 \times 10^{-2} m \cdot K \tag{2.3}$$

where

$h = 6.6252 \times 10^{-34} J \cdot s$ is Planck's constant, $c = 2.998 \times 10^8 m/s$ is the speed of light in a vacuum, $k = 1.3806 \times 10^{-23} J/K$ is the Boltzmann constant, and T is the absolute temperature of the blackbody in Kelvin.

This equation, as shown in the dashed line of Figure 2-1, shows the flux, $F_\lambda(W/m^2)$ per wavelength being emitted from the source.

The wavelength at which the peak value of the Planck distribution occurs can be found from Wien's displacement law, [30]

$$\lambda_{max} = \frac{C_3}{T} \tag{2.4}$$

where C_3 is $2897.8\,\mu m \cdot K$.

For the sun, assuming a temperature of 5800K, the peak wavelength is

$$\lambda_{max,sun} = 0.50\mu m \tag{2.5}$$

If one were to integrate the Planck distribution curve to calculate the total flux emitted by the surface, using the Stefan-Boltzmann law [6]

$$F_{total} = \int_0^\infty \epsilon_\lambda B_\lambda(T)d\lambda = \sigma T^4 \tag{2.6}$$

where $\sigma = 5.670 \times 10^{-8} W/m^2 K^4$ is the Stefan-Boltzmann constant and the emissivity $\epsilon = 1$ for a blackbody, $F_{sun,total} = 6.414 \times 10^7 W/m^2$ is emitted. This flux, which decreases proportionally to the square of the distance from the earth to the sun, $r^2_{earth-sun}$, can be used to determine the flux reaching Earth using the following equation:
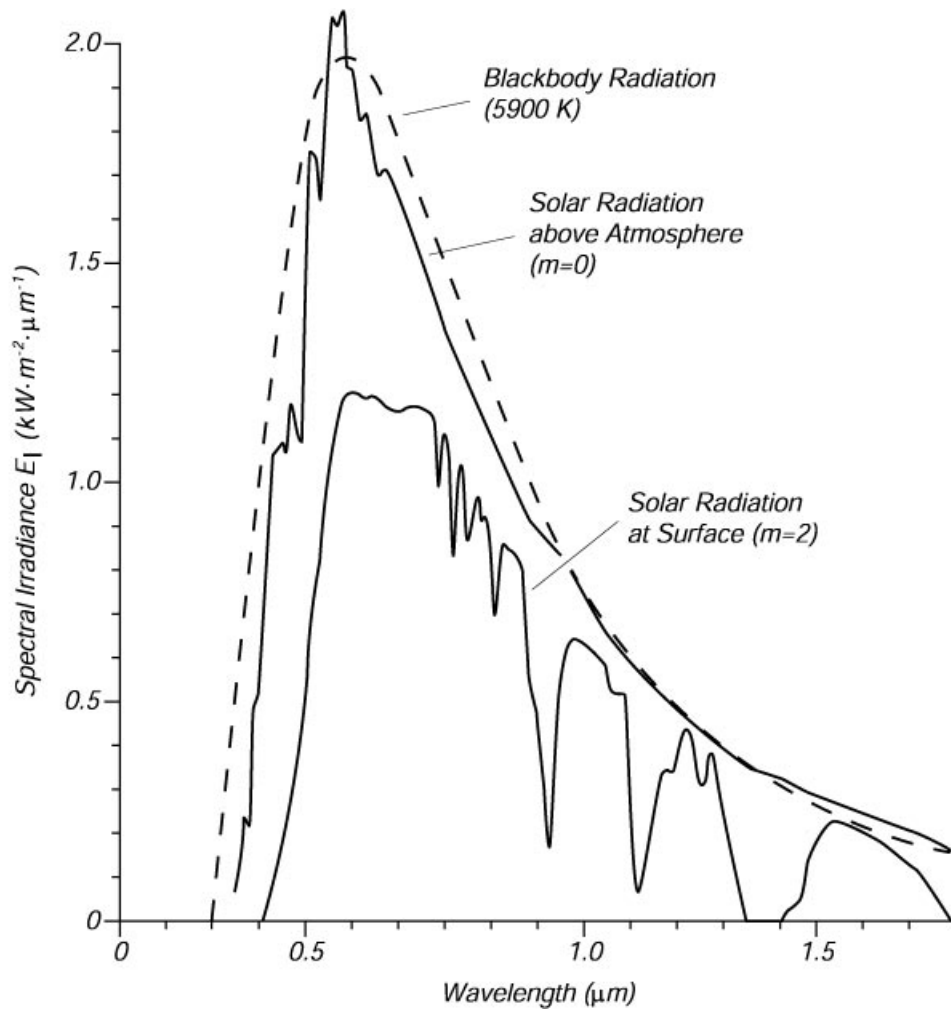
Figure 2-1: Insolation (spectral irradiance) of sunlight at top of the atmosphere and at the sea surface on a clear day. The dashed line is the best-fitting curve of blackbody radiation the size and distance of the sun. The number of standard atmospheric masses is designated by m. Thus m = 2 is applicable for sunlight when the sun is 30° above the horizon [3].
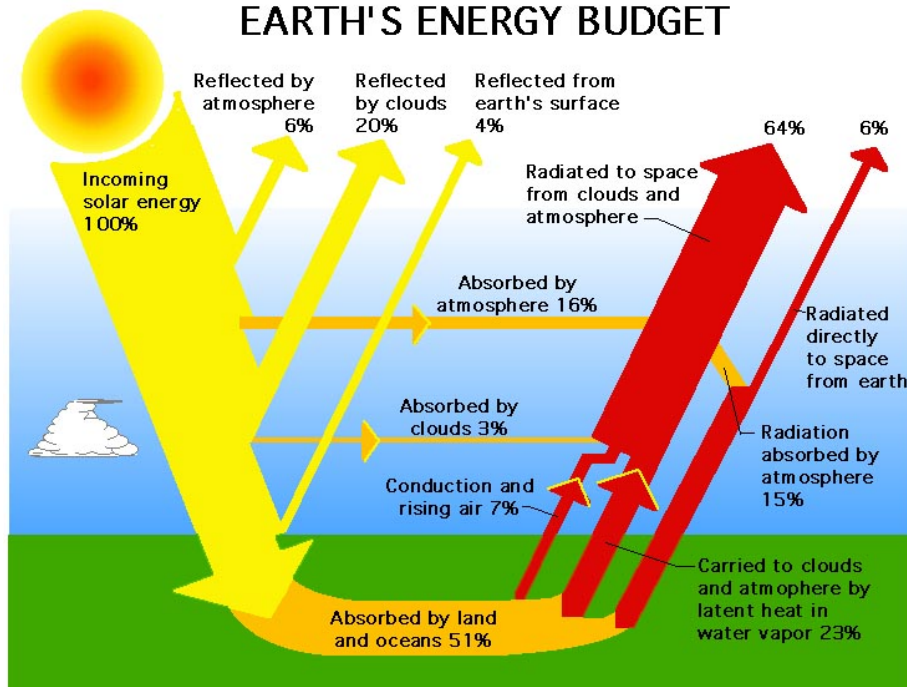
Figure 2-2: Incoming solar energy and breakdown of reflection, absorption and radiation [4].

$$F_{earth} = F_{sun,total} \left(\frac{4\pi R_{sun}^2}{4r_{earth-sun}^2} \right) \text{W/m}^2 \tag{2.7}$$

When using the $R_{sun} = 6.96 \times 10^8$m for the radius of the sun and $r_{earth-sun} = 1.5 \times 10^{11}$m, which is the average distance from the earth to the sun, one arrives at a flux, known as the *solar constant*, which has a value of approximately $1381\,W/m^2$, depending on the time of year.

In addition to the power incident on an area of the globe, amount of power contained within a given portion of the frequency spectrum is important for understanding how reflective materials must behave in order to focus incoming light.

$$F_{total(\lambda_1 \to \lambda_2)}(T) = \frac{\int_0^{\lambda_2} \epsilon_{\lambda_2} B_{\lambda_2}(T) d\lambda_2 - \int_0^{\lambda_1} \epsilon_{\lambda_1} B_{\lambda_1}(T) d\lambda_1}{\sigma T^4} \tag{2.8}$$

Based on this calculation, approximately 11% of the emission is in the ultraviolet (<390nm) range, 43% of the solar emission is within the visible range(390nm-750nm) and 46% of the available emission is in the infrared range (>750nm). In total, 93%
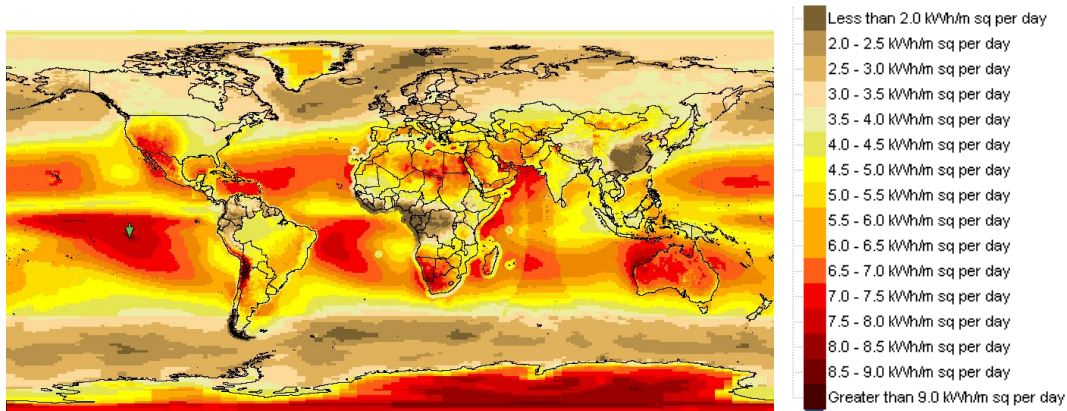
Figure 2-3: Global Direct Normal Irradiance [5].

of the emission occurs in the wavelengths between $0.29\mu m$ and $2.3\mu m$ of the spectra of solar radiation.

Unfortunately, the amount of solar energy available on the earths surface is significantly less than what is available above the outer atmosphere (Figure 2-2). In coming solar radiation experience changes both in directional distribution and in spectral distribution due to absorption and scattering [6]. The result of such a transformation is that incoming radiation can be either diffuse or direct, of which only the direct portion, generally referred to as *direct normal irradiance(DNI)* can be predictably used for concentrated solar thermal applications. Essentially, DNI is the solar radiation that would strike a solar-tracking collector at an angle perpendicular to the incoming radiation directly from the sun. The variation of diffuse radiation can be between 10% and 100% of the total solar radiation, which is what causes regional changes in ground level irradiance as well as temporal changes with shifting atmospheric components [30]. In areas of the world where concentrated solar power may be implemented on an industrial scale, direct normal irradiance from the sun can range from 7 kWh/m² per day to greater than 9kWh/m² per day. Figure 2-3 shows global direct normal irradiance reported from SWERA [5]. From a pure energy content perspective, ignoring power distribution demands, regions that are particularly attractive to solar development projects occur where direct normal irradiance is high, such as the southwest United States, regions in northern Chile, the northeast and southwest regions of the African continent, and much of Australia.

2.2 Directionality and Tracking of Incoming Solar Energy

In addition to the frequency distribution and atmospheric effects on solar irradiance on a region, the tracking of the incident angle of the sun is important for understanding how to effectively align and measure solar trough effectiveness. Such angular geometric relations of the suns path are well known, however due to the irregularity and dependence on latitude, time of day, and day of the year, tracking to obtain optimum efficiency is often a trade off between efficiency of collection and cost of additional tracking motions. Briefly, we mention the relation between some the relevant angular parameters, and note how this can affect the efficiency in design of concentrating solar trough systems.

As shown in Figure 2-4, the simultaneous rotation of the earth about an elliptical path around the sun and rotation about its own axis, which is inclined 23.5° with respect to the elliptic plane, results in a multiangular path with respect to Earth's center. The sun's location is defined using the *hour angle H*, which is the angle between the suns rays projected on the equatorial plane and the local meridian, as well as the *codeclination angle D'* (complement of the declination angle), which is the angle between the angle of the sun's rays and the North Pole [6]. These two angles depend on the number of days after the vernal equinox n, and the number of hours after solar noon, t as described by Equation 2.9 and Equation2.10 *[6]*.

$$\cos D' = \sin 23.5° \sin \frac{360° \times n}{365.25} \tag{2.9}$$

$$H = \pm \frac{360° \times t}{24} \tag{2.10}$$

From the perspective of a particular location, it is more convenient to use local coordinates based on the *latitude* L or *colatitude* L', where the *zenith angle* Z measures the angle of the sun from the local normal, and the *azimuth angle* A measures the angle between the solar noon and the sun position (Figure 2-5). The relationship

34
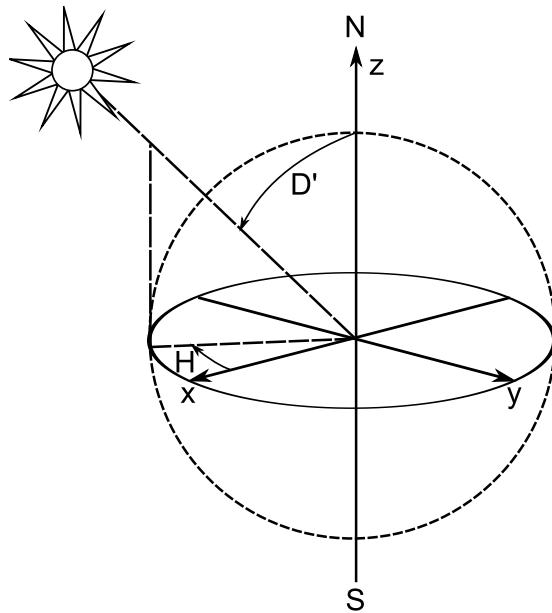
Figure 2-4: Geocentric Solar Coordinates
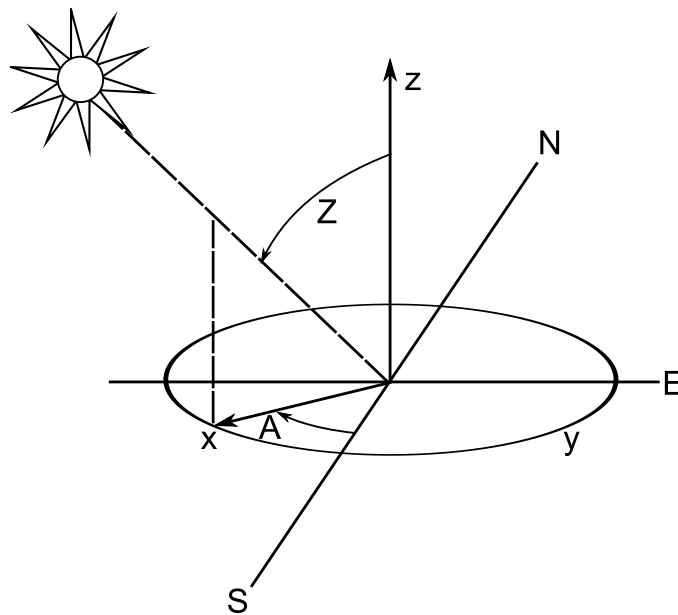
Figure 2-5: Local Solar Coordinates at a latitude L, with zenith angle Z and azimuth angle A.
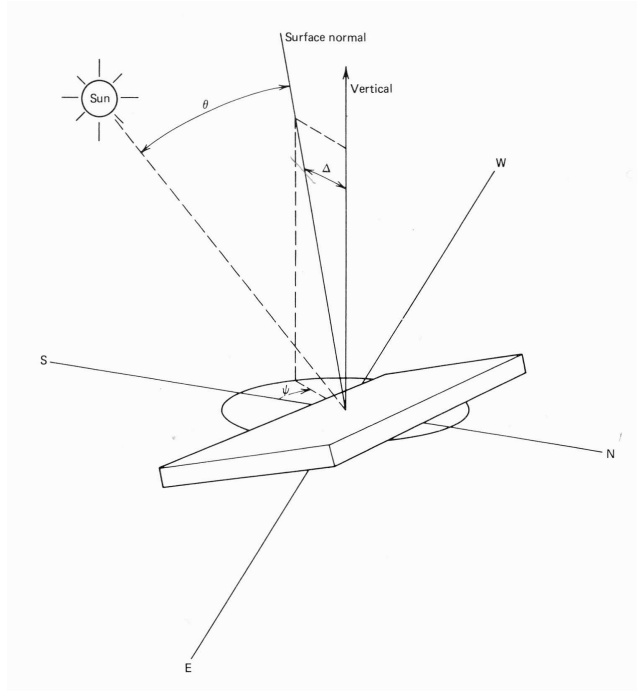
Figure 2-6: Surface Normal Relative to Local Coordinates [6].

between local coordinates and geocentric coordinates is given by Equations 2.11 and 2.12 *[6]*.

$$\cos Z = \cos D' \cos L' + \sin D' \sin L' \cos H \qquad (2.11)$$

$$\tan A = \sin D' \sin H / (\sin D' \cos L' \cos H - \cos D' \sin L') \qquad (2.12)$$

These equations allow one to determine the relative angle of a collector surface to the angle with respect to the sun, as determined by the Equation 2.13 *[6]*:

$$\cos \theta = \cos Z \cos \Delta + \sin Z \sin \Delta \cos(A - \psi) \qquad (2.13)$$

where $\cos \theta$ is the *obliquity factor*, Δ is the angle between the surface normal and vertical, and ψ is the angle between the surface normal projection on the earth's surface and due south (Figure 2-6).

In order to capture the maximum amount of sunlight over a day, solar collectors

36

are often equipped with tracking systems, which allow them to move such that they are directed to the sun as its relative position in the sky changes throughout the day. To maximize the amount of direct normal irradiance on a surface, tracking of solar concentrating systems attempt to minimize the angular difference between the surface normal and the sun angles [31, 32, 33]. Figure 2-7 shows four tracking concepts, which may be evaluated independently of structure in terms of efficiency. Full tracking, tracks the sun path in two directions, and is therefore the most efficient, although often costly to implement due to the additional actuation and control hardware required. Tracking in the E-W direction with the axis of the system aligned with the polar axis is the most efficient single axis tracking system, from a single-module perspective, however shading and compact spacing of such a system does not necessarily translate into overall efficiency for a large-scale multi-row installation. Thirdly, a system aligned with E-W axis and N-S tracking generally is more efficient, however is less efficient during the winter months than a N-S axis E-W tracking system (Figure 2-8).

2.3 Existing Solar Collector Technologies

A solar collector can generally be described as an element which concentrates the solar energy incident over a large surface onto a smaller area. Using reflecting elements, the flux density onto an absorber surface is increased compared to the that of the concentrator. In addition, the shape of the concentrator will define whether the area of incoming solar energy is focus onto a line or a point. In order to quickly develop new collector technologies, it is important to understand what has already been achieved in the field of large scale solar. Developments in smaller designs may also become relevant to larger designs with the right modifications. This section provides and overview of solar collector types, which can be categorized by the method of concentration, whether the collector is tracking or non-tracking, and whether the mirror elements are monolithic curves or faceted in a Fresnel-type construction. Advantages of each focusing concept are discussed below.
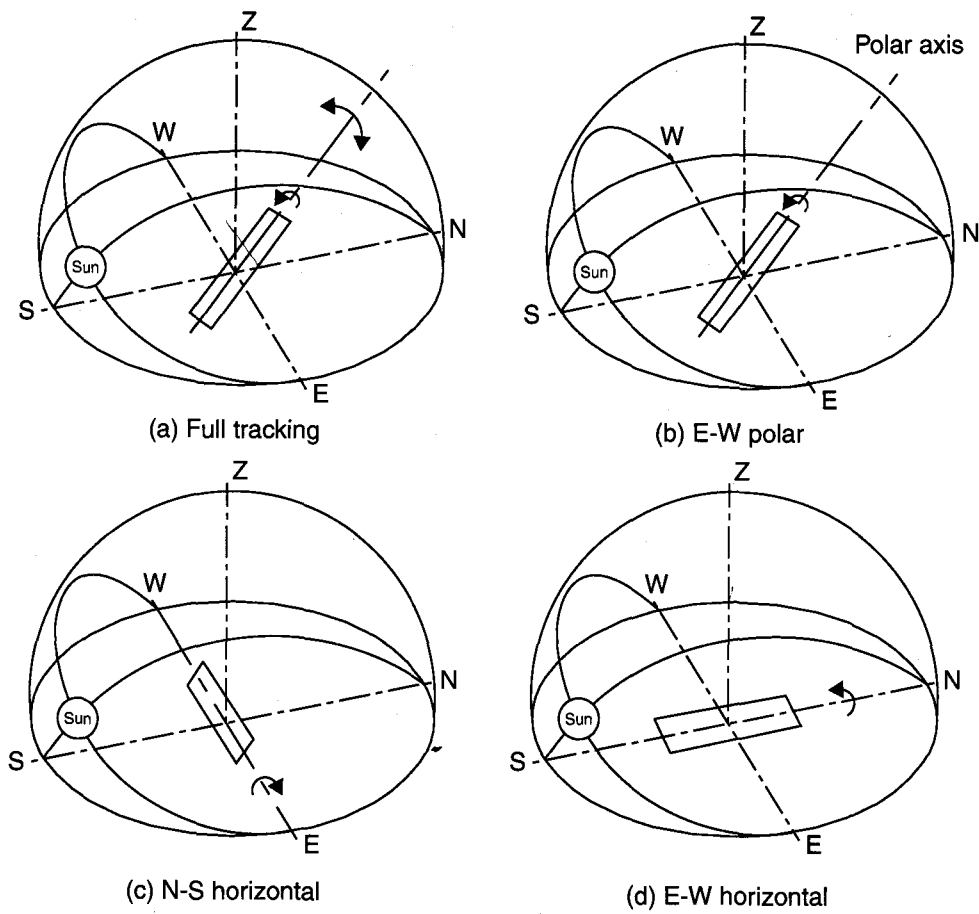
Figure 2-7: Solar Tracking Schemes [7].

Tracking mode	Solar energy received (kWh/m^2)			Percentage to full tracking		
	E	SS	WS	E	SS	WS
Full tracking	8.43	10.60	5.70	100	100	100
E-W polar	8.43	9.73	5.23	100	91.7	91.7
N-S horizontal	7.51	10.36	4.47	89.1	97.7	60.9
E-W horizontal	6.22	7.85	4.91	73.8	74.0	86.2
Notes: E = equinoxes, SS = summer solstice, WS = winter solstice.						

Figure 2-8: Comparison of Solar Energy Received [7].
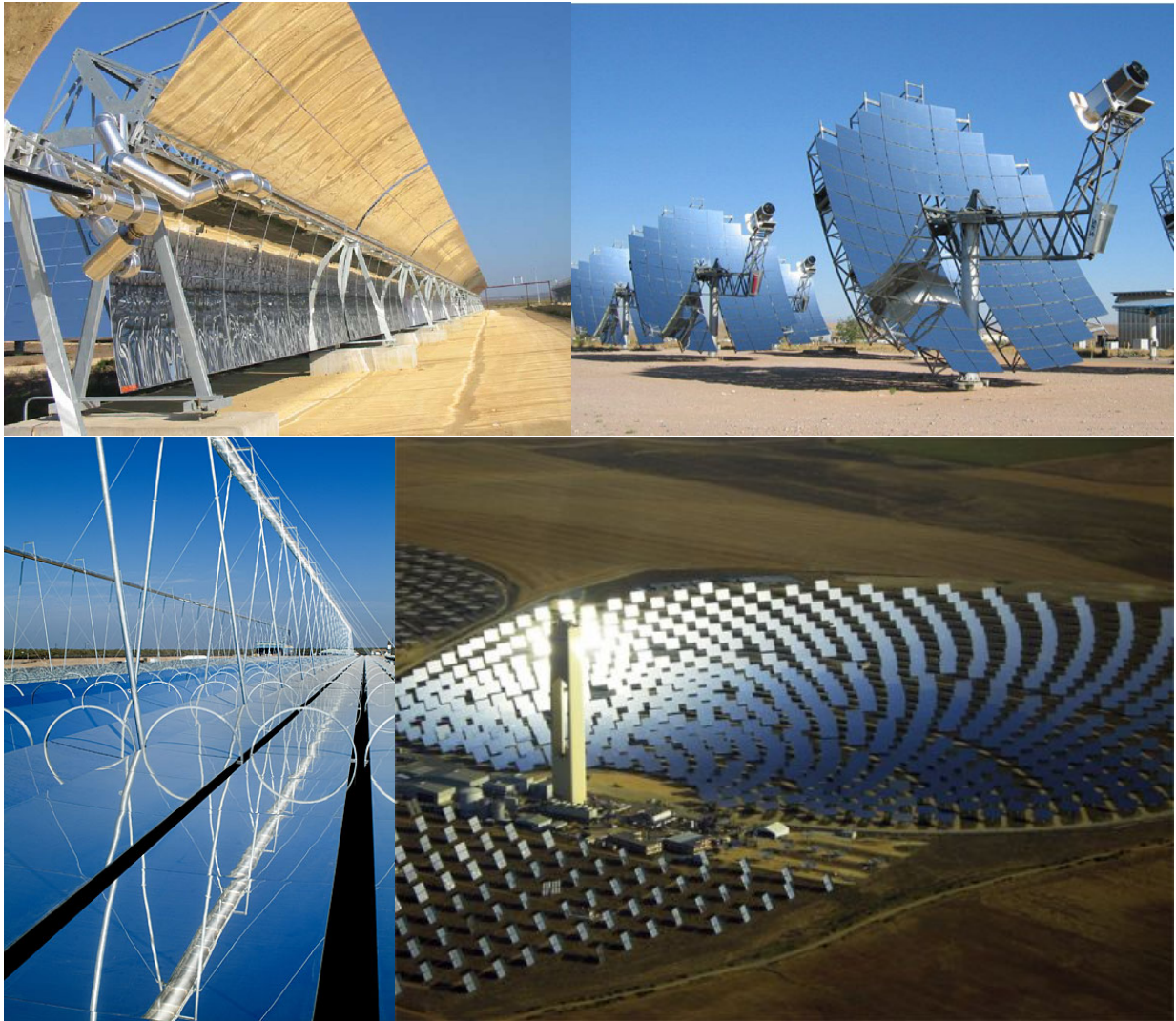
Figure 2-9: Clockwise from upper left: Parabolic line concentrating system showing collection of incoming solar [8], Stirling Engine Systems Dish Concentrator [9], Aerial view of PS10 central receiver facility in Spain, Industrial scale Fresnel-type linear reflector concept [10].
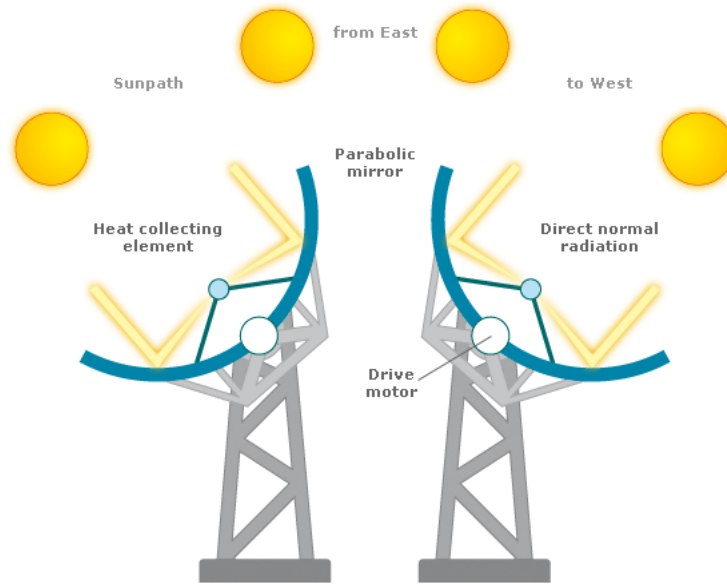
Figure 2-10: Parabolic line concentrating system showing collection of incoming solar.[8]

2.3.1 Line Concentrating

Using a continuous or faceted set of reflectors, line concentrators generally use a spherical or parabolic shape to concentrate incoming light onto an absorber tube, as is shown in Figure 2-10. Aperture diameter, rim angle, absorber size and shape may define the concentrator [34, 35, 36]. Tube may be mild steel or copper and is coated with a heat resistant black paint. Selective coatings may be used for better performance. A heat transfer fluid flows through absorber tube, is heated by incoming energy, and carries heat to a heat exchanger or similar system for driving a turbine [37, 38, 39, 40]. Commercially, the parabolic trough concept has been used in several plants, including the Solano plant shown in Figure 2-9. The parabolic trough has generally been shown to be the least expensive collector design, however, cost is still more expensive than for traditional power plants.

Depending on the complexity of the parabolic mirror elements, it is often less expensive to create a line concentrator using a series of flat mirrors which are focused at one central line absorber. In this linear concentrating concept, reflectors are mounted such that all incident parallel rays of light after reflection are focused at a common

line [41]. Generally, mounting errors and edge effects of this method often impinge upon ideal concentration ratios. The Ausra concept of a Fresnel-reflector type linear concentrator is shown in Figure 2-9.

2.3.2 Point Concentrating

Another concept for solar collectors is concentration of incident solar energy onto a point. To focus at a theoretical point, a parabolic dish is often used to direct incoming energy onto a receiver. The parabola then rotates about its optical axis to track the sun over the day (Figure 2-9). Often the surface is not strictly parabolic due to misalignment of supporting elements, which misdirect incoming light resulting in a degraded image. The travel distance of incoming rays also results in spreading, which forms and ellipsoid on the imaging plane of the system.Thermal losses from dish systems are primarily radiative and can be reduced be reducing the aperture of the absorber, however this often conflicts with the desire to maximize the amount of reflected light coming into the system. Delivery temperatures of this systems are typically very high, and collection is more efficient that other systems, but there is a limit on size with respect to manufacturability of a such a dish, without moving to a central tower concept.

The central tower concept (Figure 2-9), incorporates a series or larger mirrors, known as heliostats, into a field that concentrates incident light onto a central area. The frames of the heliostats can be used to track the sun as desired. Concentration ratios as high as 3000 can be achieved, however proper tracking arrangements are needed to avoid self shading. Dust is known to degrade performance of the large mirror arrays, which also require large fields of level ground. Advantages of such a system are that the working fluid that is fed into a steam generation plant, no longer needs to be transferred from a field of individual heating elements. Due to the centralized focusing location, heat losses over length of fluid travel such as those seen for individual systems, are relatively minimal and reduce the amount of insulation and piping. As with other field concepts, the large mirror array must withstand wind loading and extremes in weather, such as dust storms, which can damage mirror

Figure 2-11: Worldwide implementation of CSP technology[11].

surfaces.

2.3.3 Industrial Scale and Research Facilities

To a large extent, the designs that have been implemented in industrial solar power plants have come from joint partnerships between large funding initiatives and national research centers, such as the National Renewable Energy Lab (NREL) and the European Non Nuclear Energy Programme [42]. These scientific groups have worked to develop commercial facilities such as the LUZ collector design and Eurotrough concepts, which have been built in southern California and in Spain [43, 44]. In addition, fundamental research contributions have been published by smaller universities and research centers that make full scale solar plants possible [45]. According to the National Renewable Energy Lab's current estimates, existing US solar fields occupy Solar field areas 80,000-480,000 m^2 (20-119 acres), and in areas of the world with high insolation values, additional thousands of megawatts are being planned, tested and are in operation [12]. More detailed information is online for specifics of concentrated solar power sites worldwide [11]. In addition to the parabolic trough facilities, several central receiver tower facilities are in construction and testing stages of operation. The PS10 central receiver, developed with several partners including Abengoa of Spain is shown in Figure 2-9.

Table 2.1: Summary of US solar facilities, with associated trough design, power capability, frame type, and reflector type.

Project/ Location	Trough Design	Power (MW)	Frame	Mirror
SEGS I–IX Kramer Junction, CA '84-93	LUZ	13.8/30/80 (354 total)	Box truss LS-2, LS-3	Glass
APS Saguaro Tucson, AZ '06	Solargenix	1	Truss	Glass
Nevada Solar One Boulder City, NV '07	Solargenix	64	Truss	Glass

2.4 Parabolic Trough Technology

Particular details related to components of parabolic solar troughs include the mirror support structure, mirrors, and receiver tube. To understand more about compatibility with existing components and areas for improvements some details about existing solutions are mentioned below.

2.4.1 Existing Trough Structure Designs

Existing trough designs currently make up 30% of a solar field cost with the cost per square meter as seen in Table 2.2. Of the structures mentioned details of the frames are as such:

- LS-2 Frame uses six torque-tube collector modules, three on either side of the drive system. The steel structure requires precise manufacturing to build and uses a significant amount of steel which is both heavy and expensive. The galvanized steel structure uses what is known as the LUZ frame design. SEGS VI, a 14-year old 30-MWe plant currently in operation in California, is used as a reference plant to evaluate future efficiency improvements. SEGS VI was selected because it was the last plant built using all second-generation Luz collector (LS-2) technology (Figure 2-12).

- LS-3 requires less steel than the LS-2 with a similar frame design, which resulted in similar manufacturing costs. The bridge truss structure didn't lower manufacturing costs as much as expected had insufficient torsional stiffness and lower than expected optical and thermal performance. The later third-generation Luz collector (LS-3) is used at the larger 80-MWe SEGS plants had alignment prob-

Table 2.2: Costs of Existing Trough Structures [18].

LS-2	$58/m^2$
LS-3	$66/m^2$
EuroTrough	$58/m^2$
Duke Solar	$48/m^2$
IST	$48/m^2$

lems and never operated at the same level of performance achieved at SEGS V.

- Solargenix uses an aluminum frame design that attempts to avoid welding and specialized manufacturing but has the the issue of using fasteners. Although it weighs less than steel designs on-site assembly times may be large for fastener designs and alignment errors due to stacked errors present a challenge to both east of setup and overall structural accuracy.

- The Eurotrough design has a galvanized steel torque-box and is used at PSA (Plataforma Solar de Almería) Spain as well as newer installations such as the SkyFuel installation. The torque-box design. integrates torsional stiffness of a torque tube and the lower steel content of a truss design. Downsides of this design include the requirement for on-site assembly, which is expensive, cost and weird of the metal structure, and individual mirror alignment that must occur in the field.

Although targeted at lower temperatures and smaller scale production, several commercial and research stage parabolic trough technologies offer innovative structural concepts which arise in larger collector designs as well (Figure 2-13). A relevant concept on a much smaller rooftop-scale (1meter aperture) using a resin structure offers inspiration for alternative structural materials [45, 33, 46, 47, 13].

Receiver Tube

At the center of parabolic trough concepts is a receiver tube. The envelope tube consists of coated, highly-transparent and robust borosilicate glass. Anti reflective

Figure 2-12: Structural designs of existing parabolic troughs [12].

Figure 2-13: Sopogy parabolic trough design, a smaller scale trough concept [13].
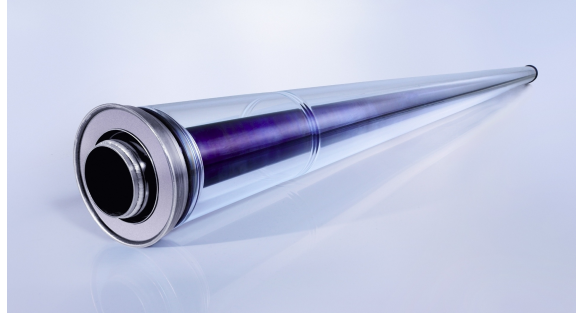
Figure 2-14: Schott PTR70 receiver tube [14].

coatings for glass have been improved in the last 10 years to improve durability. The new receiver tubes have anti-reflective coatings that deliver solar transmittances of 96.5% compared with earlier coating that only allowed 92.5% [48]. The weak point with most coatings is that they cease to adhere to borosilicate glass over time. Receiver tubes are generally approximately 13 feet (4 meters) in length, with several tubes connected for each module. Inter-module receiver tube connections often use baffles or rotating couplings, which cause flow related losses in the system. The tubes must be chemically compatible with heat transfer fluids, such as Syltherm. A standard Schott PTR70 receiver tube is shown in Figure 2-14.

Reflective Mirrors and Mirror Films

Traditional mirror technologies, such as curved glass mirrors, and thin reflective films, which have recently made gains in the market by introducing materials with 94% reflectivity, are used as parabolic surfaces that focuses onto the receiver tube [49]. New front surface reflectors with solar-weighted reflectivity of 95% are desired, compared the current 93.5% of traditional thick glass mirrors [50, 51].
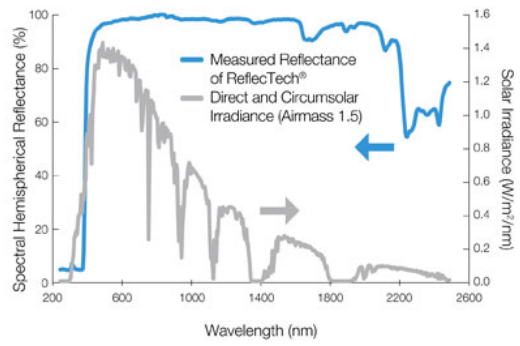
Figure 2-15: Reflectech Mirror Film [15].

Chapter 3

Problem Identification and Functional Requirements of an Improved Solar Collection System

The performance of mechanical structures have a profound effect on the ability of optical elements to properly concentrate incoming light onto the absorber tube. In order to enable new structural designs that are adequately stiff and also light, the mirror-structure interface is important for compatibility. Thirdly, by comparing new structures and mirror concepts, opportunities for mirror cleaning arise. Below are details of solar collector modules with module structure, mirror and cleaning details highlighted, in terms of current efficiency, future outlook of the technology, and target costs for the designs. An excellent source of data for such information should be pointed out in particular is a report by Sargent and Lundy in cooperation with the National Renewable Energy Lab in 2003 [12, 18]. This information, cited in tables below, provides a good overview of existing system efficiency and costs, and sets a target for both this research and for the field of solar energy systems.
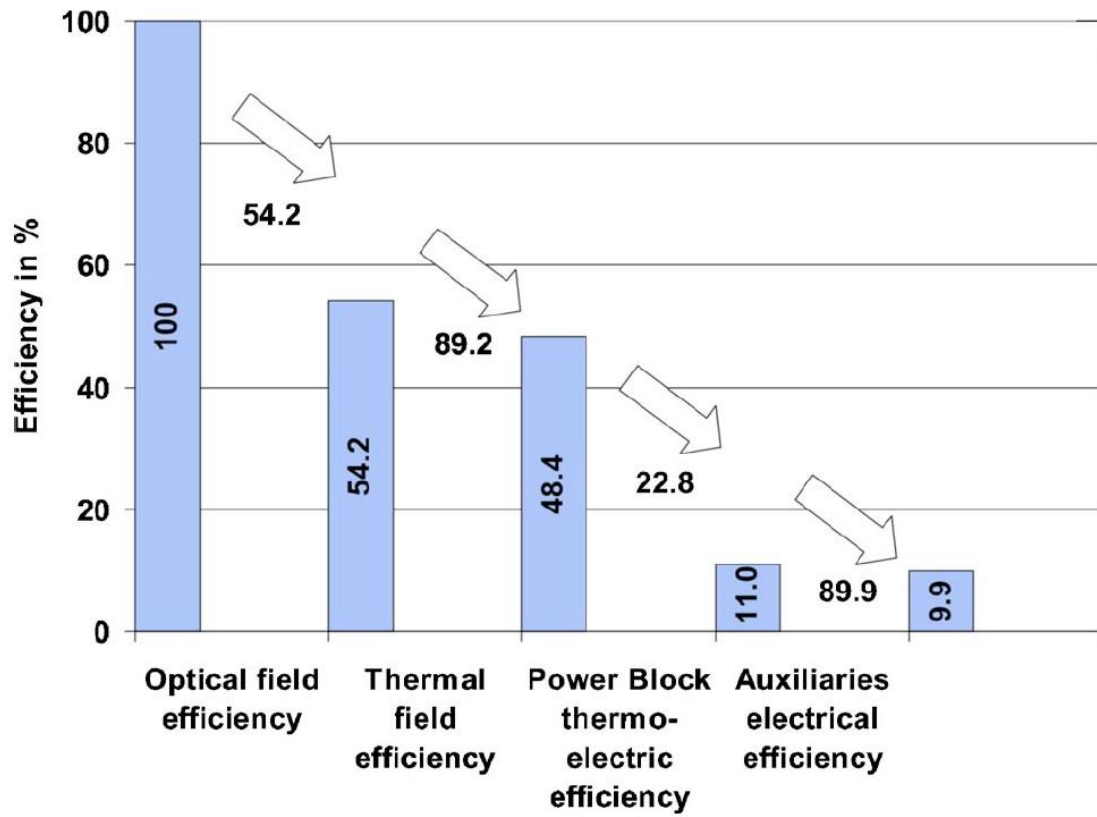
Figure 3-1: Performance calculation of DSG parabolic trough plant as reported by Pitz-Paal showing a 54.2% optical field efficiency [2].

3.1 Optical Field Efficiency

A study by Pitz-Paal et al in 2007 found that standard solar trough installations have optical field efficiencies of 54.2%, which means that almost half of all energy that could be captured using a solar collector unit is lost due to system deficiencies [2]. According to S&L 2003, the solar field optical efficiency includes "incident angle effects, solar field availability, collector tracking error and twist, the geometric accuracy of the mirrors to focus light on the receiver, mirror reflectivity, cleanliness of the mirrors, shadowing of the receiver, transmittance of the receiver glass envelope, cleanliness of the glass envelope, absorption of solar energy by the receiver, end losses, and row-to-row shadowing [18]." In addition to these losses, auxiliary electrical devices, such as controllers and sensors, account for another 10.1% loss in potential power Figure 3-1. This estimate matched the baseline solar field efficiency of the SEGS VI plant reported by Sargent & Lundy in their trough efficiency summary [18].

Focusing on module-level improvements, what is important to consider from a mechanical perspective of the collector design, is how to modify existing structure to increase overall optical field efficiency to the 2020 target of 57%, while minimizing additional thermal losses to the receiver and piping systems and without excessive electrical demands of additional sensors and peripherals. It should always be kept in mind that overall system efficiency is the target, even when designing only a module of that system. Keeping in mind that the major component costs in the solar field are the receiver (20%), the mirrors (19%), and the collector structure (29%), these elements are highlighted in particular, with cleaning and water use also having an impact on operational costs.

3.1.1 Functional Requirements

Current concentrator structures are capable of being combined into 50 meter long sections. A S&L/Sunlab report projects the need for longer concentrator lengths of 150 meters for trough designs in 2020, in order to reduce losses from the ends of the system by approximately 2.2% [18]. In order to increase the working fluid tempera-

Table 3.1: Functional Requirements of an Improved Parabolic Trough Module

Functional Requirement	Current	Target	Rationale
Collector Structure			
Trough Module Row Length	50m	150m	Reduce end losses
Increase Collector Aperture	5m	6m	Increase concentration ratio for increased efficiencies at higher operating temperatures
Structural Stability	ASCE 7-02	ASCE 7-02 + Larger Aperture	Increase concentration ratio while minimizing spillage of light due to collector deformations
Reflector Surface			
Reflector Material	Glass Mirrors	Mirror Films	Reduce module weight and required actuator load as well as mirror breakage
Mirror Cleaning			
Less Expensive cleaning	Manual Water Cleaning	Automatic Waterless Cleaning	Reduce cost of water use and transport as well as personnel

ture to a desired goal of 500C, collector apertures will need to increase such that the concentration factor also increases. Structural durability and stiffness should remain capable of supporting reflective surfaces in wind conditions without significantly degrading focusing ability. Cost of the collector should decrease despite efficiency and size increases. Costs of current structures have been reported as ranging from $48/m^2$ to $66/m^2$. Cost projections for such a structure are anticipated. NREL identifies potential for additional cost reductions by minimization of the number of required parts, simplification of fabrication and field erection reducing labor costs for on-site assembly and erection, production of metal parts using worldwide suppliers that can compete for orders. New structures will have to accommodate advances in receiver tube designs and maintain compatibility with tube couplings and supports.

Supports for alternative mirror designs and materials such thin-glass with non-metallic structural elements or using thin reflective films to reduce weight, cost, and maintenance, while increasing reflectivity. Table 3.1 gives an overview of the function requirements for mirror structure, with Table 3.3 giving projected cost savings associated with the use of mirror films.

In order to reduce contamination on the mirror surface, dust repellent and easy cleaning materials and coatings could be integrated into the trough module, with support systems for maintenance incorporated into the concept of the collector structure. Lower water use and operational complexity should also be goals of the cleaning system, since estimates of current US collectors suggest $22\,L$ of water are used per square meter of collector per year for cleaning [18]. In addition, each additional 50MW solar

trough capacity is estimated to require two additional cleaning personnel [18].

The collector requirements identified above have been found throughout the literature and are well summarized in the NREL advancement in solar trough technology investigation Table 3.2.

3.2 Target Costs for Improved Solar Collector Systems

In order to reduce component, installation and maintenance costs, it is useful to know current baseline numbers and the anticipated future costs. A detailed table of cost current system costs provided by SunLab (Partnership between National Renewable Energy Lab and Sandia National Lab) is shown below in Table 3.3.

Projections for solar collector systems are with a total cost from the current estimate of $1493/kWe to a price of $1132/kWe are estimated as target goals, which would increase the technological benefits of such a system globally. Although reductions in collector cost are only estimate at $16/unit less than current prices, the understanding that this structure must also be larger to accommodate other design requirements is a significant challenge. Increased concentration factors to support higher temperatures, longer individual collectors with larger apertures, and improved focusing, will all place demands on concentrator stiffness at a time when prices of raw materials such as steel and aluminum will continue to increase with global demand. The overall system architecture will be expected to cost less than half that of current systems, which will mean that part counts will need to decrease along with overall part complexity.

Table 3.2: Trough Projections for 2015 through 2020 (S&L Table 4.21)

Table 4-21 — Trough 200 – 2015 to Trough 400 – 2020

	Trough 200 - 2015	Trough 400 - 2020		Basis
		Sun Lab	S&L	
Plant Size	200 MWe	400 MWe		
Field Aperture Area	1,955,200 m^2	3,910,400 m^2	4,348,931 m^2	Greater aperture area required for S&L estimate due to lower estimated annual efficiency
Thermal Storage	12 hours Thermocline Direct	12 hours Thermocline Direct		
Annual Plant Capacity	56.2%	56.5%		
Heat Transfer Fluid	Hitec XL	Hitec XL		
Operating Temperature	500°C	500°C		
Receiver	Advanced 2	Advanced 2		
Coating	Advanced 2	Advanced 2		
Collector	Next Generation	Advanced Generation 1		
Annual solar-to-electric efficiency	**17.1%**	**17.2%**	**15.5%**	
Solar Field Optical Efficiency:	59.8%	60.2%	57.0%	S&L & SunLab estimates assume no change from earlier case.
IAM, end loss	91.8%	91.8%	91.8%	
Mirror reflectivity	95%	95%	93.5%	
Envelope transmittance	97.0%	97.0%	96.5%	
Solar absorption	96%	96%	94.4%	
Mirror cleanliness	96%	96%	95%	
Envelope cleanliness	98.5%	99%	98.5%	
Dumped energy	95.2%	95.2%	95.2%	
Concentrator length	150 meters	150 meters	150 meters	
Receiver Efficiency:	85.3%	85.3%	81%	
Thermal emittance	0.070 at 400°C	0.070 at 400°C	0.100 at 400°C	

54

Table 3.3: Sunlab Cost Projections (S&L Table D.1)

	SEGS VI	Trough 100	Trough 100	Trough 150	Trough 200	Trough 400
	1999	2004	2007	2010	2015	2020
Heat Transfer Fluid System						
HTF Type	VP-1	VP-1	Hitec XL	Hitec XL	Hitec XL	Hitec XL
Fluid Volume, gallons	115,500	688,380	637,560	907,830	1,201,200	2,402,400
Direct Capital Cost:						
Structures & Improvements	2,526	7,279	6,538	8,097	9,596	16,284
Collector System	44,793	249,654	181,533	226,753	259,852	452,825
Thermal Storage System	0	95,807	42,475	57,426	76,567	153,135
Steam Gen or HX System	4,304	9,964	9,227	11,161	12,772	19,394
EPGS	15,805	36,713	34,877	44,008	51,134	78,915
Balance of Plant	9,190	21,346	20,279	25,588	29,732	45,884
Total Direct Costs	76,619	420,763	294,929	373,033	439,654	766,438
Solar Collection System, $/m^2 field	250	234	184	161	140	122
Receivers, $/m^2 field	43	43	34	28	22	18
$/unit	847	847	762	635	508	400
Mirrors, $/m^2 field	40	40	36	28	20	16
Concentrator Structure, $/m^2 field	50	47	44	42	39	36
Concentrator Erection, $/m^2 field	17	14	13	12	11	10
Drive, $/m^2 field	14	13	6	6	6	5
Interconnection Piping, $/m^2 field	11	10	3	3	3	2
Electronics & control, $/m^2 field	16	14	4	4	4	3
Header piping, $/m^2 field	8	7	7	6	6	5
Foundations/Other Civil, $/m^2 field	21	18	17	15	14	12
Other (Spares, HTF, freight), $/m^2 field	17	17	11	10	9	8
Contingency, $/m^2 field	12	11	9	8	7	6
Direct Capital Cost, $/kWe						
Structures and Improvements, $/kWe	84	73	65	54	48	41
Solar Collection System, $/kWe	1,493	2,497	1,815	1,512	1,299	1,132
Thermal Storage System, $/kWe	0	958	425	383	383	383
Steam Generator or HX System, $/kWe	143	100	92	74	64	48
EPGS, $/kWe	527	367	349	293	256	197
Balance of Plant, $/kWe	306	213	203	171	149	115
Total Direct Cost, $/kWe	2,554	4,208	2,949	2,487	2,198	1,916

Chapter 4

Support Structure

To reduce cost while maintaining structural compatibility, concepts for a simpler monolithic structure were investigated. This concepts follows from the idea that the structure that supports the mirrors can be made simpler when lighter weight mirror films are used instead of traditional mirrors. Rather than having a truss-like structure, the concepts compare a large panel design whose front surface doubles as the mirror backing surface. Details and initial testing of such a design are given in this section.

4.1 Monolithic Structural Concept

Rather than break up the mirror surface into a series of glass panels that are then supported using a metal frame. The simplification of the panel structure concept was based on the idea of using a mirror film (such as 3M's or Reflectech's commercially available films) that is directly applied to a structural surface. This structural concept, where monolithic thin shell forms the entire module structure allows for the mirror surface to be formed in one layup operation if made of a fiberglass design. Reinforcement of the structure while saving weight could be accomplished with a foam-core sandwich structure. It would also allow for sheet metal panels to be formed into the parabolic shape. Stackability of modules during transport also could reduce cost installation. Figure 4-1 shows a CAD model of the simplicity of the design proposed.
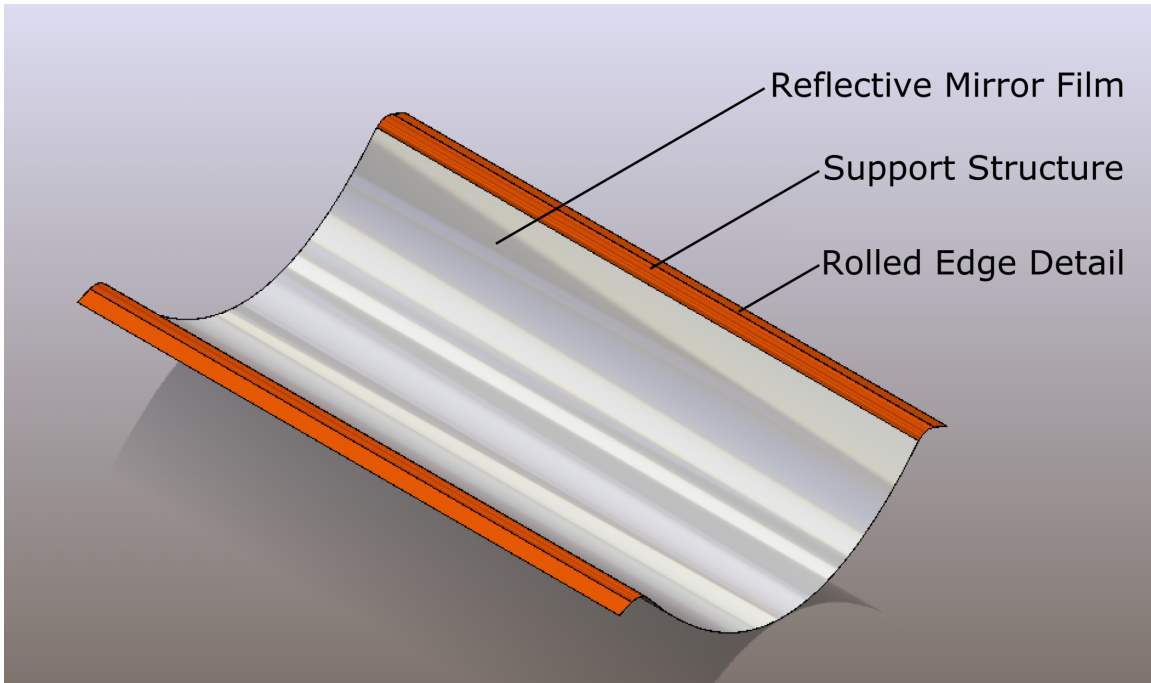
Figure 4-1: Simplified panel structure concept.

4.2 Structural Material Selection

Depending on cost, availability or materials, and manufacturing capabilities in a region composite structures or sheet metal panel designs could both potentially provide sufficient panel stiffness and surface accuracy to be used as the structural layer for a collector module.

Structural Fiberglass Layup

To test the feasibility of using a composite structural panel, a 1/10th scale parabolic trough panel was manufactured using a bi-axial knit fiberglass and vinyl ester resin, both lower cost composite options that can later be optimized for structural loading conditions and modified to include more sophisticated sandwich structures and inserts. Nylon matting sheet was used as a central structural layer between the bi-axial knit layers with a diagram of the layup cross section shown in Figure 4-2. A gel-coat layer was added during the final fiberglass prototype to create a smoother inner surface and as a filler for pinhole irregularities that could possible impact the mirror film
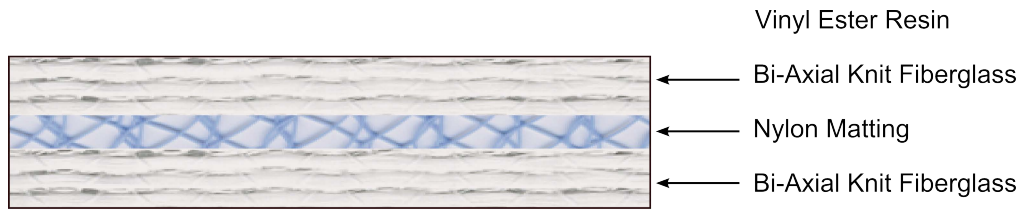
Figure 4-2: Cross-section of fiberglass trough layup construction.
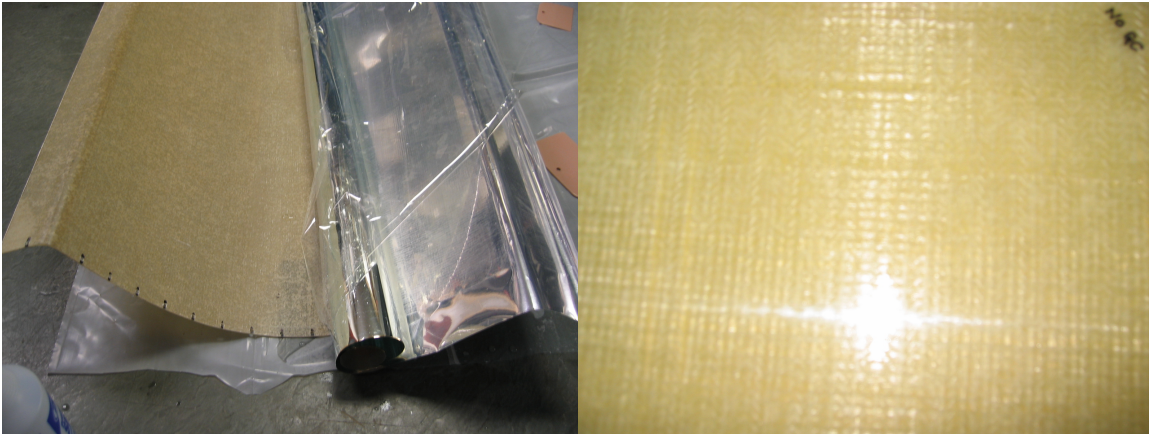
Figure 4-3: Final fiberglass trough module being in process of mirror film application (left) with detail of surface (right).

application process. To create the scale trough panel, a the composite layers were vacuum formed on a convex parabolic mold to ensure a smooth inner trough surface. Details on the mold construction, trough layup, and specifications can be found in Appendix A.

The trough prototypes formed from the vacuum layup process were capable of a 4-6mm layup thickness requirements, were able to produce a sufficiently smooth surface to apply an adhesive mirror film, and were later used to test panel loading on the structure (Figure 4-3).

Sheet Metal

In addition to using fiberglass as a structural backing material, sheet metal panel designs using aluminum and galvanized steel were considered, because the materials are produced in a variety of thicknesses and in large sheets that could be stretched or bent into a parabolic shape. Sheet metal panels have the advantage that they are

recyclable when considering long term replacement costs and are not susceptible to UV damage. Figure 4-4 shows a mock-up of a small galvanized steel panel section bent over a parabolic outer frame. The formed bend at the edges of the sheet gives the sheet the stiffness needed to ensure that between the parabolic bulkheads, the flat sheet is pulled into parabolic form. The structural design philosophy utilized is that of a thin walled shell with stiffeners, similar to an airplane fuselage. Parabolic circumferential stiffeners to serve as precision forms against which thin sheet metal sections are easily bent. Once curved, however, the sheet metal panels become very stiff along its length. To add them as a separate part would be expensive, so instead, they can be integrally formed from the sheet metal panels.

Testing of panel loads was conducted for the fiberglass panel, however ultimately recyclability and manufacturing costs will determine which material to use. Details on the surface roughness and loading on the panel are covered in Sections 4.5,4.7, and 5.2.

4.3 Module Integration

In addition to details of the trough panel structure, concepts for reducing field complexity were considered and are mentioned here briefly. When considering an overall trough module concept, the placement of the receiver tube was selected to coincide with the center of rotation of the trough so that the trough could move independently of the receiver tube if necessary. Collocation of the receiver tubes with the pivot axis could also allow for simplification or even elimination of inter-module receiver tube couplings, which currently are a major source of thermal fluid leakage and heat loss in the field. Secondly, to allow for lighter-weight panel structures to operate without excessive torsional deformation, actuators on individual modules were considered as a viable alternative. While costs of the actuators and control systems may be larger than for the large scale hydraulic systems, this configuration has the advantage that, if the troughs move independently of the receiver tubes as mentioned previously, breakdown of a single actuator only affects a single module. With hydraulic systems
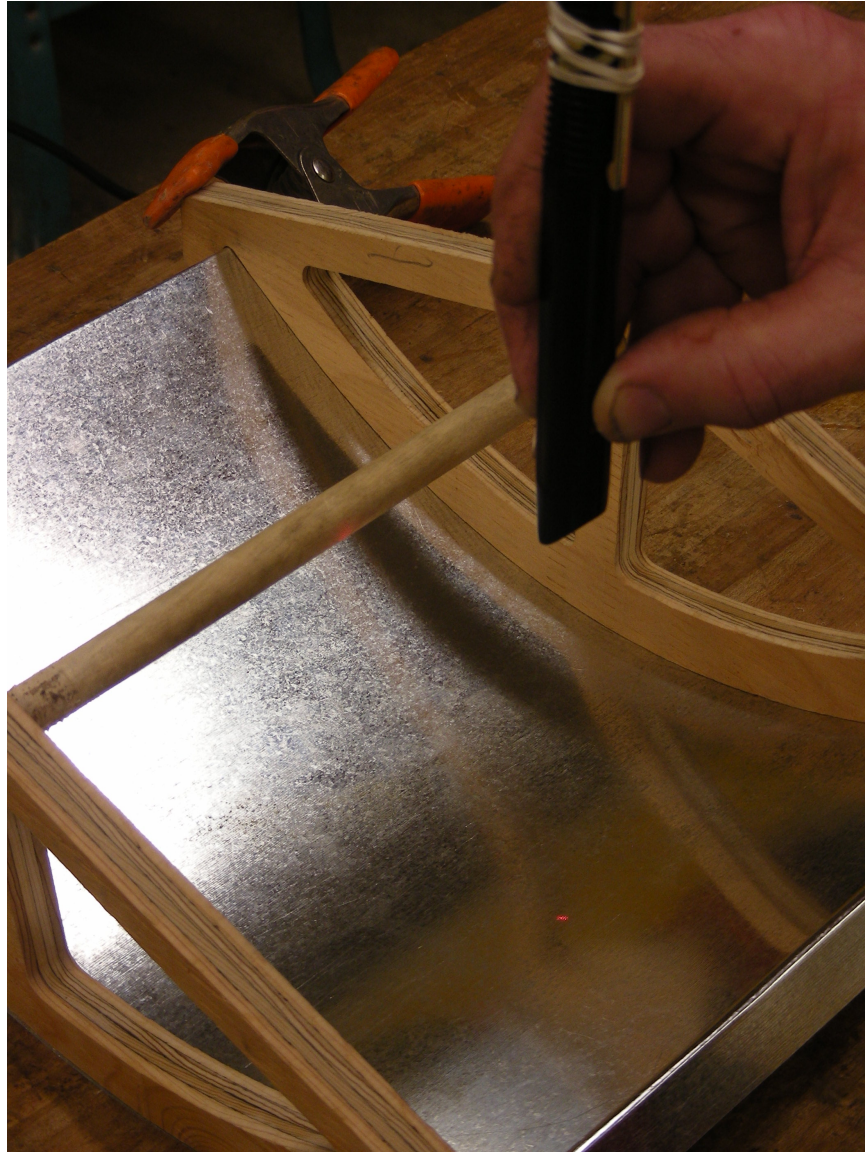
Figure 4-4: Mock-up of galvanized steel panel concept.

that drive 50meter long sections or more, breakdowns or maintenance of one actuator would have a large affect on plant output because five to ten modules would no longer be able to track the sun. A third module integration modification that was considered briefly was a leveling ability built into the pylon support structure. By enabling individual pylons to be adjusted slightly for local height changes, leveling of the solar trough site, which currently requires 2% or less grading, could potentially be eliminated. Such a measure could reduce installation costs significantly, has the potential to better integrate with local habitat by allowing existing vegetation to remain in place, and could even reduce local dust levels that may be exacerbated by removal of ground-level plant species. While these measures were considered as potential additions to the trough design, integration of these details into module concepts that would need to be tested on a larger scale trough module.

4.4 Loading and Required Stiffness

Parabolic trough solar collectors are considered a viable technology for solar thermal alternative energy generation; however efficiency of the trough field array has been limited by structural deformations of modules resulting from actuator loading and wind loading, which disturb collector focusing. In order to maximize the economic competitiveness of new designs, parabolic trough modules must be designed at a lower cost than those of current collector fields while maintaining equal or better focusing efficiency through structural stiffness, and allowing for higher field operating temperatures with larger module apertures [52].

In order to heat a fluid that will deliver energy to a steam turbine, incoming solar energy focused onto the receiver tube located at the center of the parabolic trough focal line. A parabola may be generated as the envelope of two concurrent line segments by connecting opposite points on the two lines. and in manufacturing of three-dimensional structures, many forming operations have been considered to create the parabolic shape [53, 54, 51]. In generating a parabolic shape the optical efficiency can easily be degraded. The solar field optical efficiency includes incident angle effects,
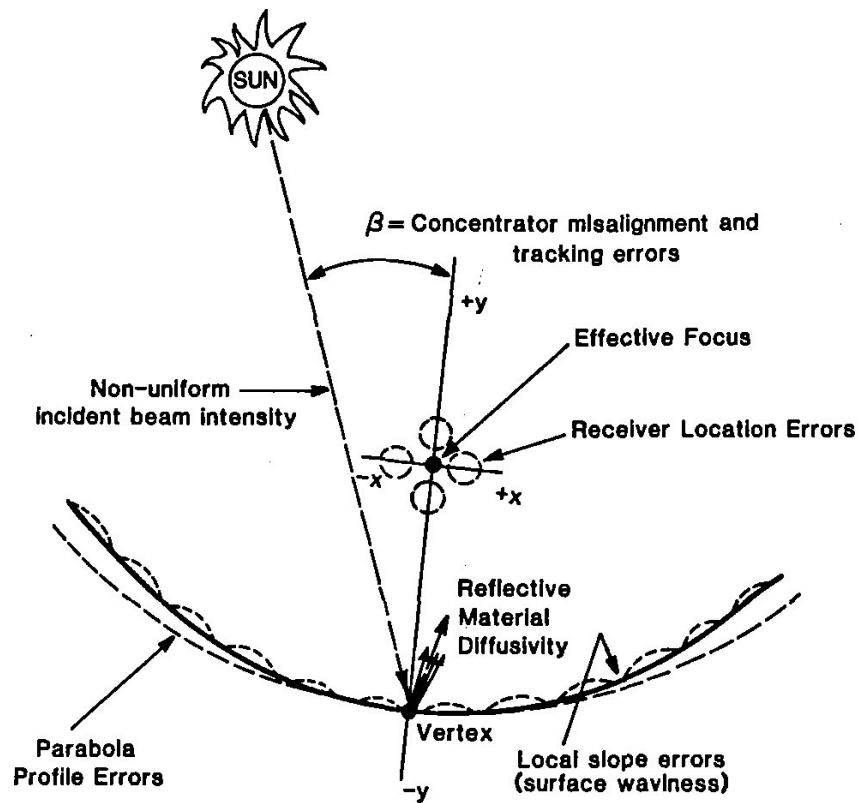
Figure 4-5: Optical Errors in Parabolic Trough Collectors [16].

solar field availability, collector tracking error and twist, the geometric accuracy of the mirrors to focus light on the receiver, mirror reflectivity, cleanliness of the mirrors, shadowing of the receiver, transmittance of the receiver glass envelope, cleanliness of the glass envelope, absorption of solar energy by the receiver, end losses, and row-to-row shadowing [3, 12]. A detailed statistical study of the effects of trough errors on focusing has been conducted by Guven et al with a diagram of the parameters considered in Figure 4-5 [16].

Manufacturing and assembly defects play a large role in the overall shape that a parabolic reflector has in the field. The collector structure, which consists of the metal support system of the collectors is made of supporting elements, each of which if not properly aligned can lead to overall warping, and misalignment such that not all sunlight is absorbed. Wind loads during maximum wind speeds dictate the required strength of these units. Recent wind tunnel testing has provided improved data for use

in optimizing field layouts but more detailed analysis of loading is needed to reduce the weight of the structure and to ensure long-term reliability. Future goals involving longer collector sections still require cost reductions and structural improvements in stiffness for larger plants [12, 55].

4.5   Wind Loading Standards

Solar structures in the United States are generally designed to withstand loading conditions according to ASCE 7 specifications . This publication, Minimum Design Loads for Buildings and Other Structures allows for a simplified procedure, analytical modeling or wind tunnel testing to meet the requirements [56]. ASCE 7-02 requires that the design load be no less then $10\,\mathrm{lb/ft^2}$ ($0.48\,\mathrm{kN/m^2}$) multiplied by the area A_f defined as the area of a structure normal to the wind direction or projected on a plane normal to the wind direction. Using this measure, a typical solar trough module 10 meters in length and with a 5 meter aperture would then need to withstand at least $24\,\mathrm{kN}$ as a design load from wind alone. This design load is slightly higher when using the analytical procedure outlined for panel structures and an example for location is given below. While simplifications regarding the solar structure are made, this analysis is a starting point for understanding structural loading until specific requirements are outlined for solar structures and reflector panels.

4.5.1   Analytical Method 2 of ASCE 7-02 for a Parabolic Trough Located in the Southwest United States

In order to use the ASCE analytical method, the specification requires a regular shaped building and a structure that is not subject to cross-wind loading, vortex shedding, or instabilities related to flow over the panel. These conditions, while highly dependent on the structural details, can be assumed for a solar trough such that other static loading concerns may first be evaluated. In order to evaluate loading of a parabolic trough the design procedure in 4-6 was used to determine the basic wind

1. *The basic wind speed V* and *wind directionality factor K_d* shall be determined in accordance with Section 6.5.4.
2. An *importance factor I* shall be determined in accordance with Section 6.5.5.
3. An *exposure category or exposure categories* and *velocity pressure exposure coefficient K_z or K_h*, as applicable, shall be determined for each wind direction in accordance with Section 6.5.6.
4. A *topographic factor K_{zt}* shall be determined in accordance with Section 6.5.7.
5. A *gust effect factor G or G_f*, as applicable, shall be determined in accordance with Section 6.5.8.
6. An *enclosure classification* shall be determined in accordance with Section 6.5.9.
7. *Internal pressure coefficient GC_{pi}* shall be determined in accordance with Section 6.5.11.1.
8. *External pressure coefficients C_p or GC_{pf}*, or *force coefficients C_f*, as applicable, shall be determined in accordance with Section 6.5.11.2 or 6.5.11.3, respectively.
9. *Velocity pressure q_z or q_h*, as applicable, shall be determined in accordance with Section 6.5.10.
10. *Design wind load p or F* shall be determined in accordance with Sections 6.5.12 and 6.5.13, as applicable.

Figure 4-6: ASCE 7-02 Design procedure for wind loading analysis.

speed V, wind directionality factor K_d, the importance factor I, exposure category, velocity pressure coefficient K_z, topographic factor K_{zt}, gust effect factor G, enclosure classification, internal pressure coefficient GC_{pi}, force coefficient C_f, velocity pressure q_z, and design wind load F.

The basic wind speed was found assuming a site that would be located in the southwest United States, since this area is generally known to receive the most solar energy per square meter in the continental US. Other areas of the world can be analyzed similarly, with differing assumptions about the site conditions and wind speeds. Using Figure 4-7a basic wind speed, V, of $40 \, \text{m/s}$ (90 mph) for a 3 second gust was used at this location. No special wind regions were assumed at the location, which could otherwise increase the suggested basic wind speed. However, such analysis may be required once more specific site is chosen.
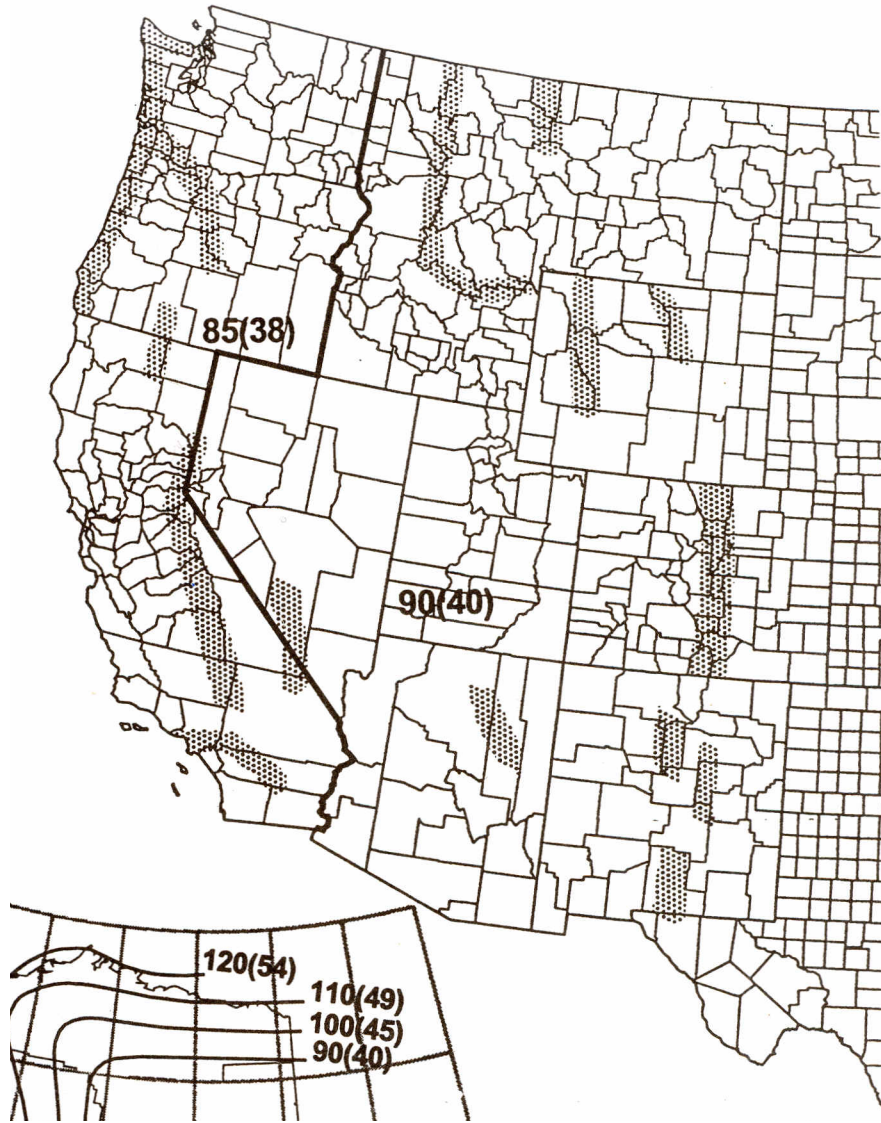
Figure 4-7: ASCE 7-02 chart of wind speed for western United States, mph (m/s).

Although the ASCE code is used for trough structures, the code is focused largely on traditional building details and so the assumptions about the shape, were made to best approximate a thin structure. For this reason, the wind directionality factor, K_d, was assumed to correspond to a 'solid sign' structure type and was assigned a value of 0.85. This factor ranges for structure types such as buildings, arched roofs, trussed towers, and chimneys, with values of 0.85, 0.90, or 0.95 assigned to the structures.To assign the importance factor I, the nature of the solar field and associated modules was rated as a Category III Structure under "Power generating stations and other public utility facilities not included in Category IV," where category I-IV were described ranging from low hazard buildings to emergency structures. Using ASCE Tables 1-1 and 6-1, and assuming the structures would be located in a non-hurricane prone region, a final importance factor I of 1.15 was assigned, where the range of possible values was between 0.77 and 1.15. An exposure category was found by assuming a Surface Roughness "C" for the open terrain that usually surrounds solar fields, and an Exposure of "C", meaning the Surface Roughness holds for more than 800 m. Table 4.5.1 of Terrain Exposure Constants suggests values for determining the final terrain exposure. Assuming a height above ground of 7.6m (25ft), greater than the 15ft minimum recommended, and using the equation

$$K_z = 2.01(\frac{z}{z_g})^{2/\alpha} \tag{4.1}$$

it was found that a value of K_z= 0.94 could approximate the situation for a parabolic collector in its tallest configuration.

The topographic factor, which accounts for topographical wind effects, K_{zt}, can be determined from the equation:

$$K_{zt} = (1 + K_1 K_2 K_3)^2 \tag{4.2}$$

However, for the situation of a trough module installed in a field,the topographic factor can be ignored because the device is assumed to be on a flat surface. Therefore

Table 4.1: ASCE 7-02 Exposure Constants (ASCE Table 6-2)

Exposure	α	z_g (ft)	$\hat{a}$	$\hat{b}$	$\bar{\alpha}$	$\bar{b}$	c	ℓ (ft)	$\bar{\in}$	z_{min} (ft)*
B	7.0	1200	1/7	0.84	1/4.0	0.45	0.30	320	1/3.0	30
C	9.5	900	1/9.5	1.00	1/6.5	0.65	0.20	500	1/5.0	15
D	11.5	700	1/11.5	1.07	1/9.0	0.80	0.15	650	1/8.0	7

*z_{min} = minimum height used to ensure that the equivalent height $\bar{z}$ is greater of $0.6h$ or z_{min}.
For buildings with h ≤ z_{min}, $\bar{z}$ shall be taken as z_{min}.

we determined the topographic factor to be, $K_{zt} \sim 1$ according to ASCE7-02 6.5.7.

The velocity pressure, q_z, is determined by section 6.5.10. It is given by the equation below:

$$q_{z\ (SI-units)} = 0.613 K_z K_{zt} K_d V^2 I \tag{4.3}$$

Since the structure is classified as 'rigid' according, requiring a fundamental frequency $\geq$ 1Hz, a gust effect G factor of 0.85 was used for the structure as specified according to 6.5.8.1. The external pressure coefficient or force coefficients, C_f, is determined in accordance with section 6.5.11.3. With a Poisson's ratio of less than 0.3, a ratio height to width of less than 3, a vertical diameter of approximately 5-6meters, and a height above the ground of approximately <15m gives us a force coefficient, $C_f \sim 1.2$, a there was no internal pressure coefficient for this particular experiment. The enclosure classification for this structure is open according to section 6.2 definitions and the area of the structure normal to oncoming wind, A_f, can be calculated as such:

$$A_f =\sim 5m * 10m =\sim 60m^2 \tag{4.4}$$

The design force (wind load), F, which is designated by the following equation:

$$F = q_z G C_f A_f \ (lbf/Newtons) \tag{4.5}$$

Table 4.2: ASCE 7-02 design coefficient with values determines for a solar trough module and associated units (if necessary).

	Coefficient	Value	Units
Nominal Design, 3sec Gust	V	40	m/s
Importance Factor	I	1.15	
Wind Directionality Factor	K_d	0.85	
Exposure Category	K_z	0.94	
Topographic Factor	K_{zt}	1	
Velocity Pressure	q_z	901.2	
Gust Effect Factor	G	0.85	
Force Coefficient	C_f	1.2	
Normal Area	A_f	60	m^2
Design Force	F	55	kN

is also known as the equivalent static force and is approximately, 55kN, given all other factors. This force acts perpendicularly to the face on a vertical line passing through the geometric center. The resultant force is perpendicular to the face at a distance from the vertical line passing through the geometric center equal to 0.2 times the average width of the sign. In our case, $0.2 * 5m = 1m$ off from the center. Given this static force from the analytical method of ASCE code, an understanding of design specifics and loading of such structures can be made in more detail for a particular trough design and solar plant installation site.

4.6   Prototype Results

To test panel loads in a wind tunnel, which can give more accurate drag coefficient information and force data, a 1/10-scale dual motor modular trough concept was designed and built based on the model in Figure 4-8. Key elements of this concept include an actuator on either side of a solar trough module, which reduces the overall torsional stiffness required for the fiberglass structure which acts as the mirror film backing surface. The trough panel itself is an open structure manufactured using a vacuum layup technique described in Appendix A and with flanged edges increase bending stiffness. With the parabolic end bulkheads, each of which is position controlled by a motor, the net result is a parabolic section with very high apparent
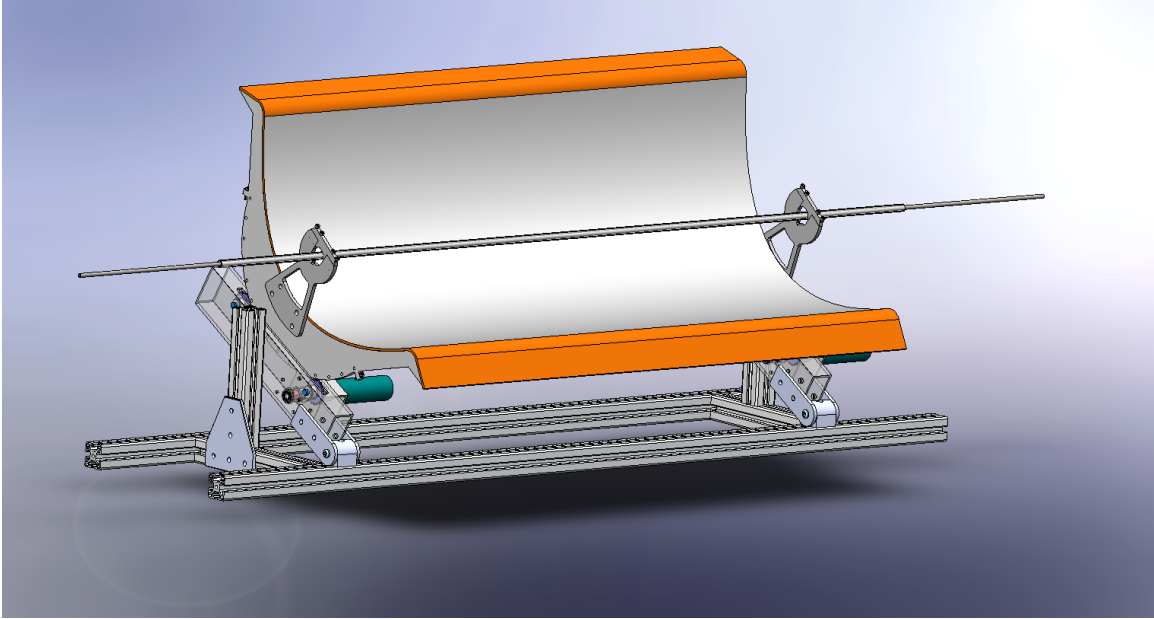
Figure 4-8: Dual motor solar trough concept with monolithic composite structure.

stiffness. By driving both ends of the trough section, the torsional stiffness of the parabolic trough structure can be lower without concerns for errors in parabolic position relative to the sun and deformations due to actuation. The chain drive system used to drive each end of the prototype module is shown in Figure 4-9 and an exploded view of the assembly is shown in Figure 4-10.

The final prototype trough, which was capable of both thermal measurements as well as panel measurements depending on the sensor configuration is shown in Figure 4-11. In the top image, the full trough prototype is shown with the mirror film applied to the panel surface, however the protective coating that prevents the film from scratching has not been removed. The actuation systems is visible in the from the side of the unit, with the lower images showing a small pump system for thermal measurements. In the lower right, the loading and positioning measurement system on the lower right is shown.
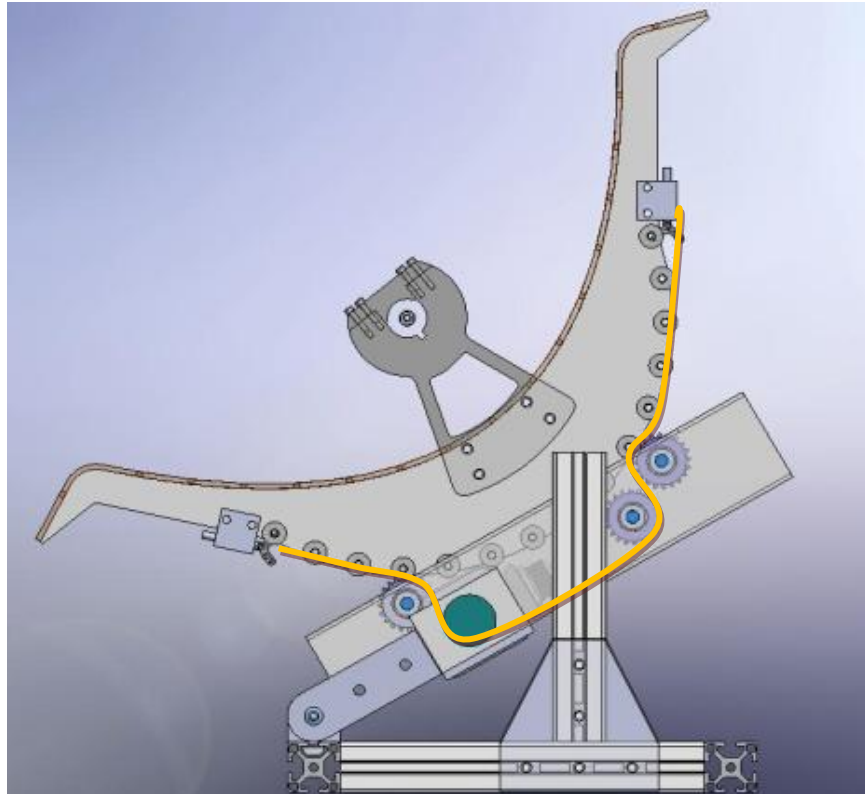
Figure 4-9: Side view of parabolic trough with chain drive. Transparent view through the drive section shows actuator (teal green) and sprockets. Chain path is overlaid in orange.
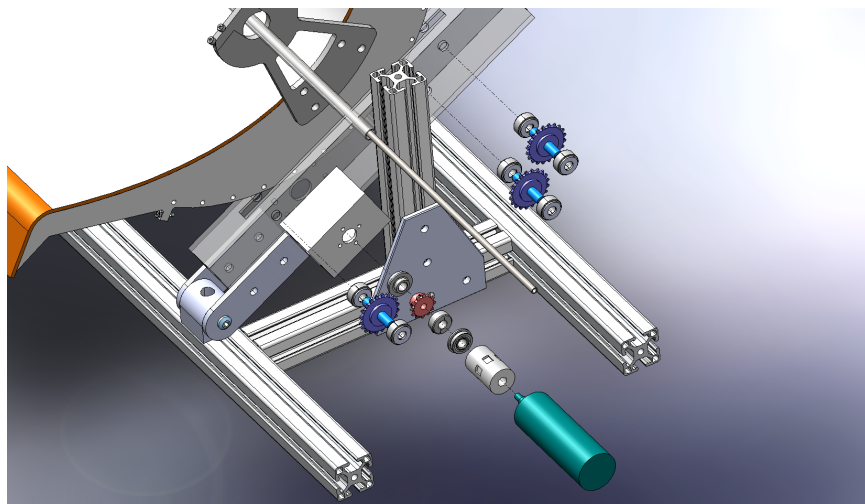
Figure 4-10: Exploded view of motor concept.
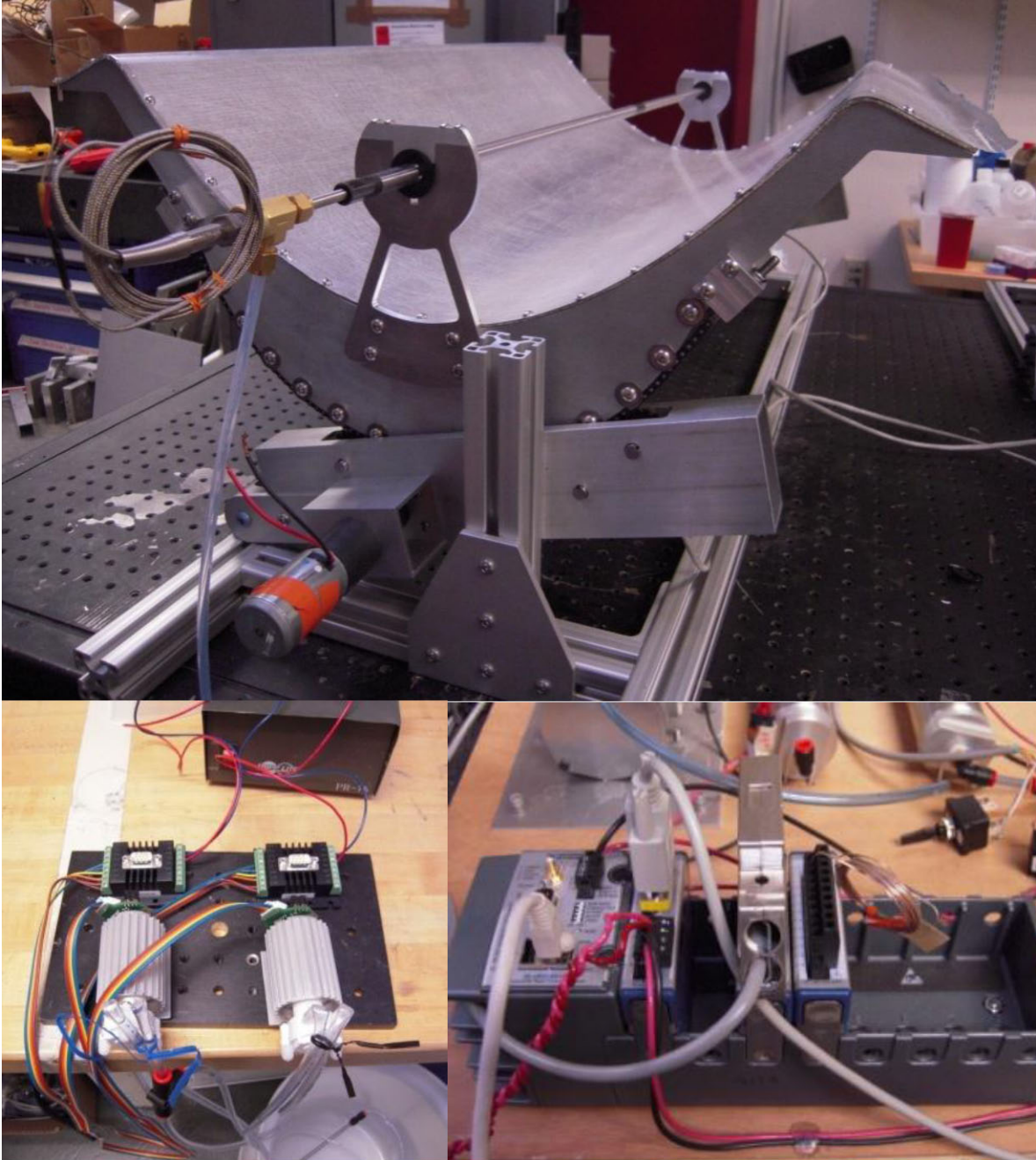
Figure 4-11: Fully assembled trough prototype (top) with pump system (left) NI compact RIO (bottom right).

4.7 Wind Tunnel Testing

To truly optimize for structural stiffness, it is necessary to understand the magnitude and directionality of loads on trough modules as well as the resulting deformations. Previous wind loading studies of parabolic trough collectors evaluated forces and moments on a 1/25-scale field of modules as well as a single collector in that field, however deformations and vibrations were not evaluated and a larger scale model was not used to verify single trough module results [55]. In addition, advances in flow simulation and modeling of structural loading current since Randall et al. allow for more detailed computational aerodynamic analysis than previously available [57, 58, 59]. To understand more about the loading conditions of a large-scale parabolic trough module, a series of wind tunnel tests have been conducted on a 1/10-scale trough module. Results of these wind tunnel tests were then used to compare FEA loading predictions of a 1/10th scale parabolic trough module as well as to simulate flow over a series of modules. Vibrations on the center of the trough module and relative displacement of the trough were also recorded to understand some of the dynamic effects of wind loading on the trough structure. Additionally, use of a prototype monolithic trough module as the test structure allows for evaluation of a new generation of structural concepts. A comparison with finite element analysis and flow modeling simulations may build upon previous wind tunnel studies to provide a more detailed understanding of solar trough collector module loading conditions.

4.7.1 Experimental Setup and Test Procedures

Experimental testing of a parabolic trough prototype was conducted in the MIT Wright Brothers wind tunnel, with a scaled model of a trough having a monolithic fiberglass reflector surface as well as position and acceleration instrumentation that is described below.

Table 4.3: Frontal area, Ac, for varying trough pitch angle and yaw

Pitch Angle (degrees)	Frontal Area, Ac
0 and 180 Yaw	-
0	0.2906
30	04485
45	0.5782
60	0.6658
90 Yaw	-
0	0.1031

Wind Tunnel

Initial testing was conducted in the MIT Wright Brothers wind tunnel ($3\,m \times 2.3\,m$ elliptical section with $5.5\,m^2$ cross sectional area), a closed-section wind tunnel with 1.8×10^6 operating Reynolds number at atmospheric pressure [60]. The cross sectional area of the trough structure was 1.8-12% of the total test section cross sectional area, which was within standard allowance with respect to blockage requirements [61].

Measurements of drag, lift, and side forces as well as trough pitch, yaw, and roll moments were measured using an external six-component pyramidal balance located beneath the test section of the wind tunnel [61]. Simulatneous measurement of tunnel conditions including temperature and percent relative humidity allowed for measurement correction of velocity. Bulk force measurements were recorded in LabView at a sampling rate of approximately $992\,Hz$ and averaged twice per second to give 107 averaged readings per test configuration, which was sufficient for the determination of static loading conditions. Further characteristics of the MIT Wright Brothers Wind Tunnel and associated correction factors have been previously reported [60, 62, 63].

Trough Structure

To evaluate loading on a parabolic trough structure, a 1/10-scale model was constructed with a composite monolithic reflector surface of 1meter in length, 0.5 meter aperture and 103 degree rim angle Figure 4-12. The composite trough thickness was not scaled but rather set at 4mm, to ensure a vacuum layup part could be produced.

The trough model was actuated using a chain drive that allowed for motion from
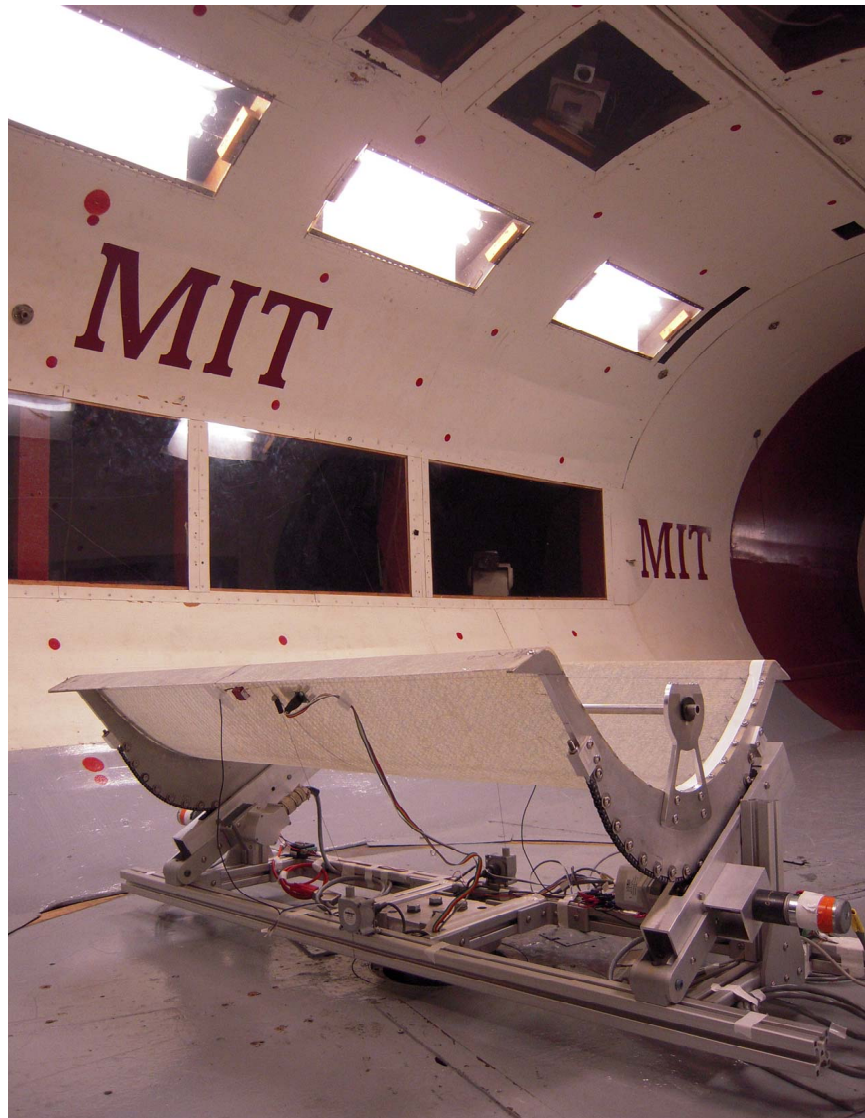
Figure 4-12: 1/10th scale parabolic trough module in MIT Wright Brothers Wind Tunnel
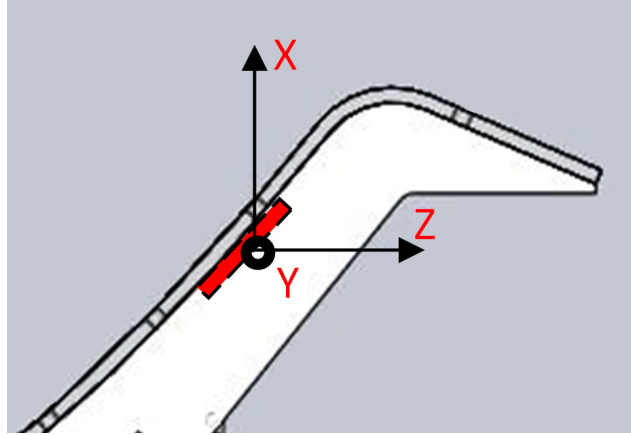
Figure 4-13: Orientation of three-axis accelerometer on parabolic trough receiver surface during wind tunnel experiments.

a $0-60$ degree pitch, where 0 degrees corresponded to the focal plane of the parabola being normal to the ground and the aperture plane being parallel with the ground plane of the tunnel test section. The accuracy of pitch angle positioning was less than 0.1 degrees and position control was implemented to allow for automated pitch adjustment from the control room of the wind tunnel. Table 4.7.1 shows the projected cross sectional area of the scaled trough including support structure and actuating system.

Three-Axis Accelerometer Measurement of Trough Motion

Measurement of trough panel acceleration was measured using an Analog Devices ADXL326 3-axis accelerometer that is capable of measuring $\pm 16\,g$. This sensor was mounted on the backside surface of the forward edge of composite reflector structure along the center of the trough lengthwise (Figure 4-13). Values for acceleration measured are reported with respect to the orientation of the trough structure, which requires geometric transformation of raw data to account for pitch angle adjustments. In this reference frame, yawing of the trough, which would represent a change in wind direction, does not affect the accelerometer orientation.
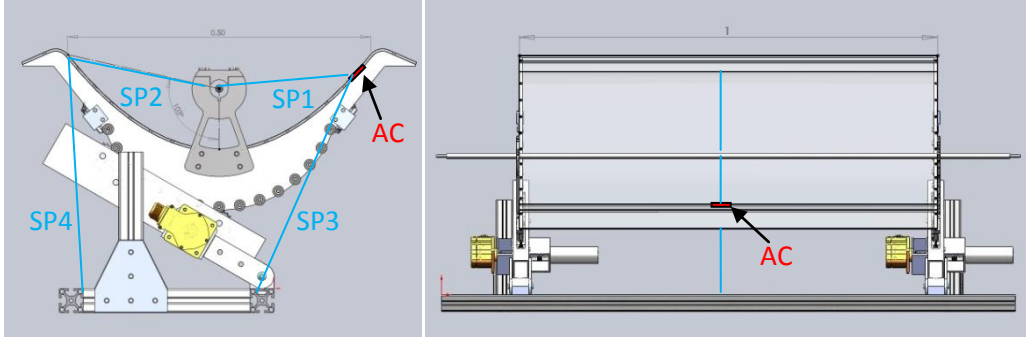
Figure 4-14: Locations of four string potentiometers (SP1-SP4) and accelerometer (AC).

String Potentiometers

Relative displacements between the reflector surface and the receiver tube can cause defocusing of incoming light at the focus of the parabolic trough. To understand the effect of wind loading on the displacement, four string potentiometers were attached to the trough surface (Figure 4-14). Two ultralight 14gram Celesco M150 string potentiometers with 1% accuracy and $76.2\,mm$ (3in) total travel potentiometer were used for measurements of deflection from both ends of the central trough plane to an aluminum rod at the focal line of the trough, which served in placed of a glass receiver tube. Larger Celecso SP2-25 string potentiometers with 635mm of travel were attached to the base of the test setup and connected to the center-line of the trough. Displacements were measurable for nominal lengths of $250\,mm$ from the reflector surface to the receiver tube and $390\,mm$ from the reflector surface to the base of the trough support structure. A $3\,V$ DC power supply with 3mV ripple was used for sensor measurements. Purely vertical motion of the receiver tube would be represented in the data as lengthening of SP1 and SP2 with no change in SP3 or SP4. Purely horizontal motion of the receiver tube would appear as a change in SP1 that is opposite in sign as SP2 with no motion in SP3 or SP4. Motion of the trough structure that results in an increasing aperture would appear as an increase in the length of SP1 and SP2 while SP3 and SP4 also decrease in length. Loads that result in an aperture decrease would cause SP1 and SP2 to decrease while SP3 and SP4 increase.
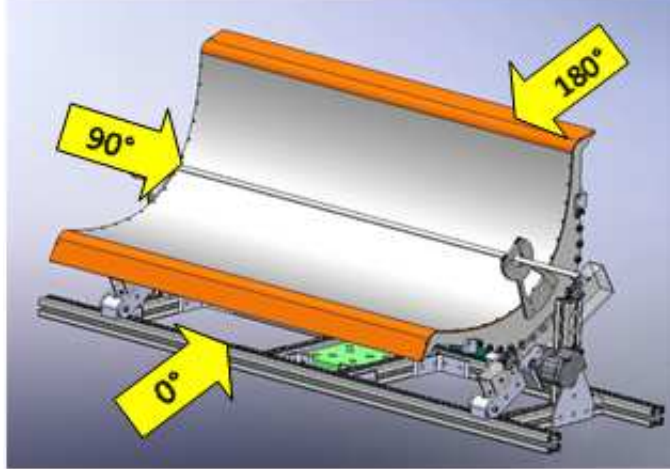
Figure 4-15: Wind direction shown for trough yaw orientations of 0 degrees, 90 degrees, and 180 degrees.

4.7.2 Test Procedures and Parameters

Bulk force and moment measurements as well as string potentiometer displacements and accelerometer voltages were measured at trough pitch angles of 0, 30, 45, and 60 degrees relative to the vertical focal line of the parabolic cross section (Figure 4-16). For each of these positions, the wind speed was set to 0, 10, 20, 30, 40, 50 and 90 mph (0m/s to 40.2m/s) in the wind tunnel. Measurements were repeated for trough yaw positions of 0, 90, and 180 degrees (Fig 4-15) to represent differing wind directions. Because the cross-section of the parabolic trough does not vary significantly with pitch at the 90 degree yaw angle, only one trough pitch angle of 0 degrees was tested.

4.7.3 Results

Drag force on the trough sections is shown in Figure 4-16 for the three yaw directions and four pitch angles. At 0 degree yaw, drag force on the panel at 0 degree pitch ranges from 9.2N at 4.5m/s (10mph) to 100N at 22.3m/s (50mph). At the most extreme wind conditions tested 40.4m/s (90mph) the loading on the panels increases to 352N for the same configuration. For increasing pitch angle, where the aperture of the parabola faces toward oncoming wind, the forces on the panel increase even more dramatically. A 0 degree yaw and 60 degree pitch the trough sees loads of 11N at

4.5m/s (10mph) and 281N at 22.3m/s (50mph). For the extreme 40.4m/s (90mph) case, the change in pitch angle results in loading of 892N on the panel.

For the 90 degree yaw direction, where oncoming wind is directed at the side of the panel, the drag force was tested for 0 degree pitch (Figure 4-16 center) and loads on the panel were expectedly lower than for 0 degree yaw. At 4.5m/s (10mph) drag force measures 1.6N, with 22.3m/s (50mph) loads of 51N and 40.2m/s (90mph) loads at 322N. These values are significantly lower than the 0 degree yaw and 0 degree pitch measurements, but with the frontal area for this orientation being one third that that of the 0 degree yaw position, suggest that they are relevant for appropriate structural design.

The drag force for 180 degree yaw, where the wind direction faces the convex back side of the trough is shown in the upper section of Figure 4-16. Results are similar to those for 0degree yaw, which is expected given the same frontal area but different curvature. For the 0 degree pitch at 4.5m/s wind-speed, loading was 4.2N, and 22.3m/s (50mph) measured 89N loads. At 40.2m/s (90mph) 278N loading was measured on the panel. At the 60 degree pitch angle, loads for 4.5m.s, 22.3m/s and 40.2m/s measured 11N, 284N and 873N respectively.

Side forces on the panels for varying pitch and yaw angles are plotted in Figure 4-17. Side forces are significantly lower than the drag forces on the panel and generally show an increase in magnitude with increasing pitch. Side forces for the 0 degree and 180 degree yaws consistently measured less than 10N for wind-speeds below 22.3m/s (50mph) and less then 30N even at 40.2m/s (90mph). The 90 degree yaw of the panel showed much higher loads at 4.5m/s, 22.3m/s and 40.2m/s, measuring 16N, 167N and 526N. This could be the result of the panel not being exactly 90 degrees in the wind tunnel, resulting in a larger projected area and also due to the larger side area where flow differences on the panel have a much larger effect.

Lift forces on the panel are shown in Figure 4-18 and show loads ranging up to 525N for 40.2m/s wind-loads and 0 degree yaw. In this direction, forces do not increase as regularly with an increase in pitch angle for the same yaw position. Lift forces for the 90 degree yaw position are much smaller, with magnitudes of a magnitude of 20N

at 40.2m/s.

Given the discussion of forces on the panel, the drag coefficient, which can be used for scaling the loading effects to larger panels is shown in Figure 4-19. Ideally, drag coefficient is independent of wind-speed, and the plots of drag coefficient all show reasonably stable values of the drag coefficient for any given pitch and yaw orientation. Drag coefficients for 0 degree yaw range from 1.35 to 1.45 for the pitch angles measured. Drag coefficient for the 90 degree yaw position was 0.57 on average with the 40.2m/s measurement appearing as an outlier. Finally, the drag coefficient when wind approaches from behind the panel is slightly lower, as 1.06 to 1.33 with 0 degree to 60 degree trough pitch angles.

Measurements of panel displacements and vibrations did not reveal significant vibrations or displacements, even under the largest loading situations. At wind-speeds of 40.2m/s (90mph) and 60 degree pitch, string potentiometer measurements on the inner panel structure measured a total displacement of 0.86mm which as only 0.2mm more than the recorded 0.65mm measurement with the sag in the center rod of the trough. This magnitude of the measurement was not significant when compared effects such as movement of the center rod and flutter of the cable connecting the string potentiometer to the rod in the center of the focal line. Vibrations measured using the 3-axis accelerometer also did not measure significant panel flutter at the outer edge of the panel center-line, where the larger vibration effects would be measurable. A baseline measurement of the system of the test setup in the wind tunnel at nominal 0m/s (0mph) wind-speed registered average vibrations of $3.8m/s^2$ (0.37g) and vibrations at 22.3m/s (50mph) were measured as having a maximum panel acceleration of $12.8m/s^2$ (1.3g).

Visual observations of the panel at the maximum wind-speed and panel pitch confirmed displacements that were not of a visible magnitude. It should be noted that in all but one instance of automated positioning, the motor system consistently was able to position the trough so that both sides were accurately positioned when checked with an electronic level. In the exceptional case, the trough was unintentionally positioned during wind-speeds of 40.2m/s and slipping on one side of the trough
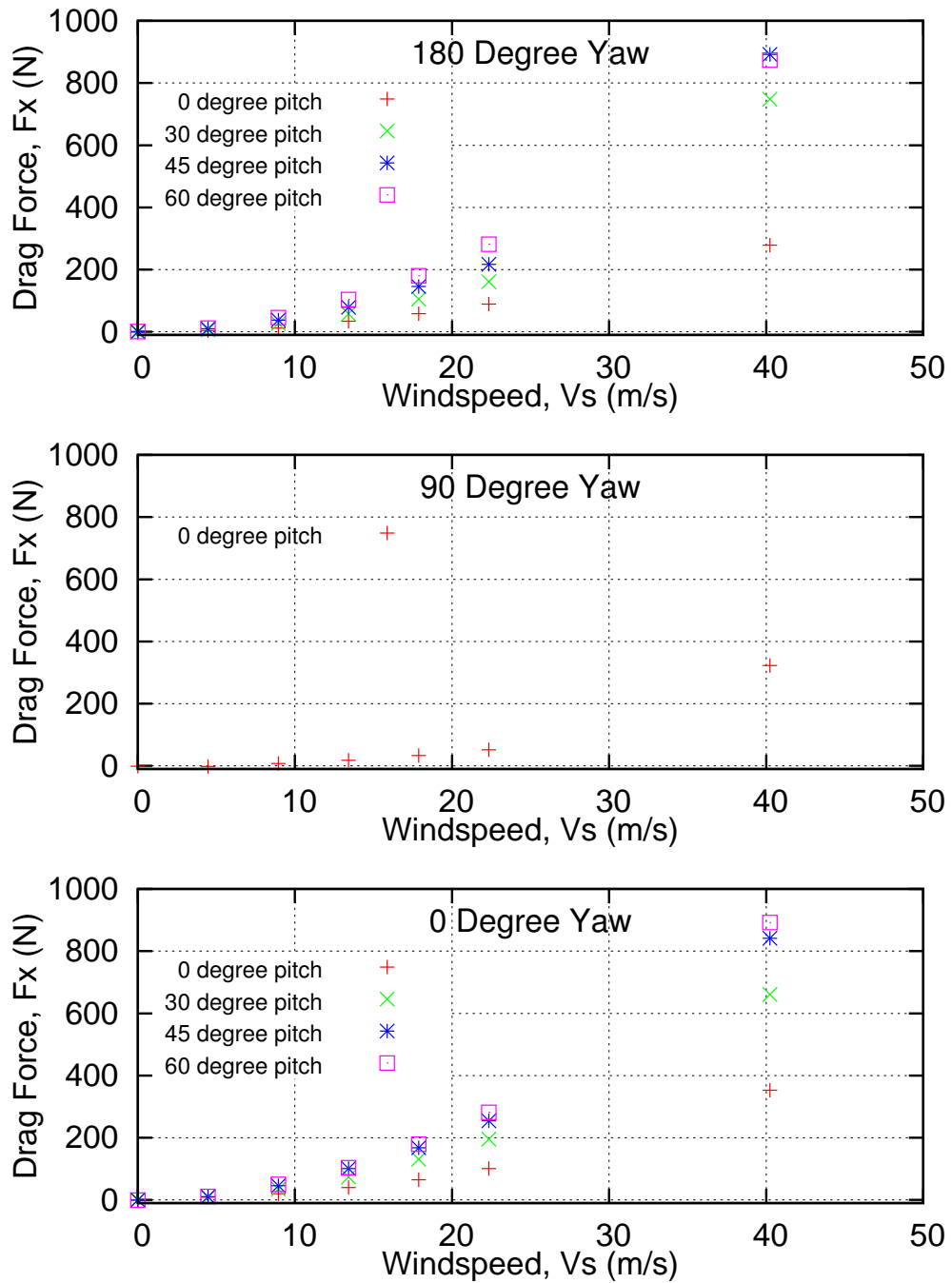
Figure 4-16: Drag Force, Fx, as a Function of Wind-speed, Vs.
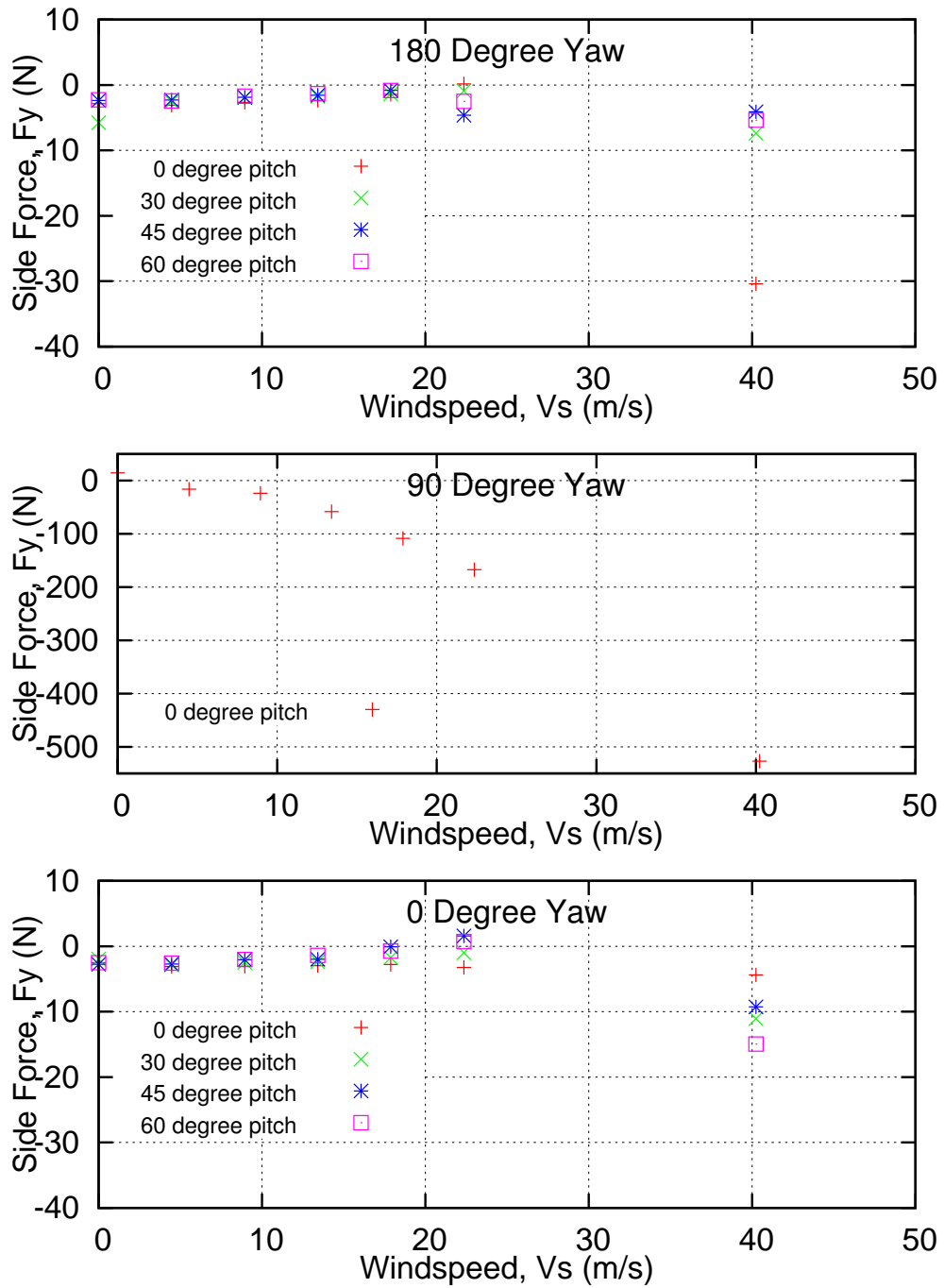
Figure 4-17: Drag Force, Fy, as a Function of Wind-speed, Vs.
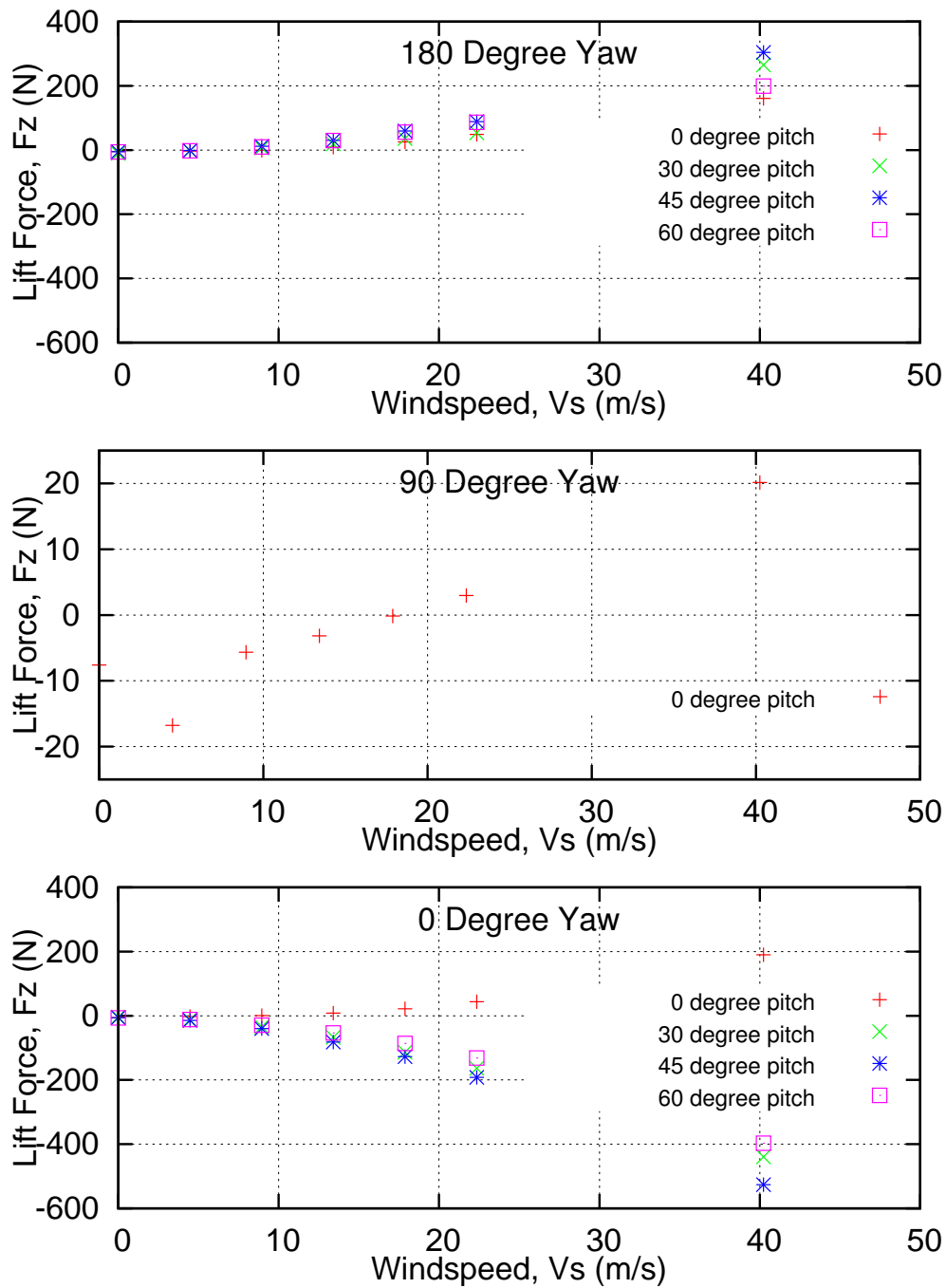
Figure 4-18: Drag Force, Fz, as a Function of Wind-speed, Vs.
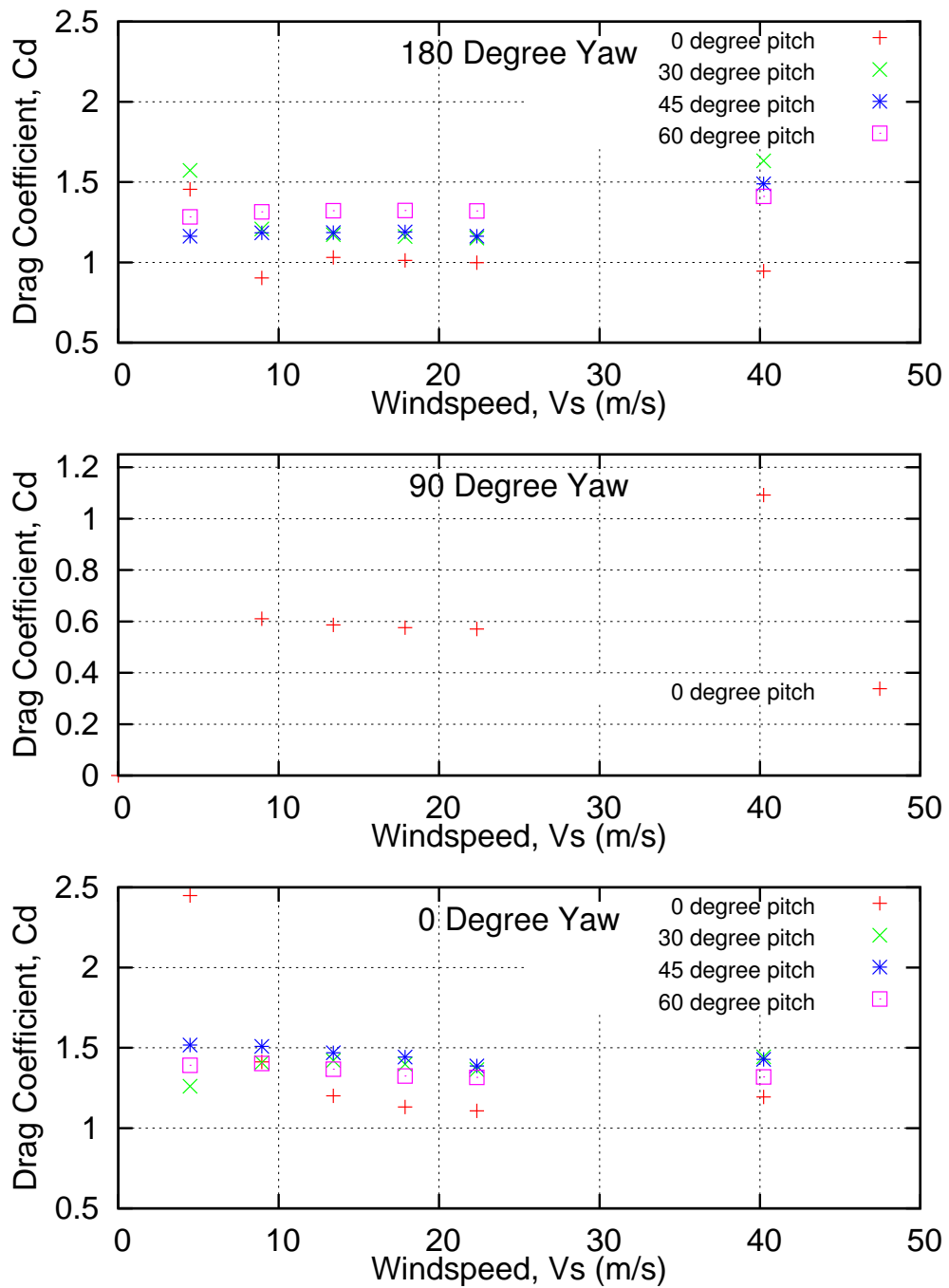
Figure 4-19: Drag Coefficient, Cd, as a Function of Wind-speed, Vs.

occurred, which resulted in a permanent positioning offset between the panel edges. No damage was observed in the panel, and such cases would be avoided with the use of an absolute encoder. In this setup, motor controllers were only compatible with incremental encoders.

4.8 Conclusion

When evaluating the ASCE 7-02 wind loading codes as well as measured panel loads on a parabolic trough module, a thin structural frame that is supported and driven on both ends can withstand expected loads on the front surface while maintaining positional accuracy during operation. This dual drive system would allow parabolic trough actuation on both ends with smaller actuators, while preventing the torsional inaccuracies of actuation schemes that use one large actuator for an entire row of trough modules.

Chapter 5

Mirror Surface

Reflective mirror films, which have been introduced to concentrated solar technology as an alternative to mirrored glass reflectors, present an opportunity for compatibility with less expensive, lighter weight, and more robust structural mounting surfaces. While existing mirror films have a measured reflectivity of up to 94%, the surface roughness of the mounting surface affects overall focusing efficiency of a curved collector panel to a receiver [64]. Understanding to what extent mounting surface roughness affects the performance of mirror films allows for manufacturing specification on the surface of raw materials, which could reduce overall solar concentrator costs, and may allow for alternative structural materials to be used.

5.1   Material Options

One major requirement in the implementation of the thin-shell trough module described in the previous chapter is that materials that form the structure are also compatible with the mirror film that covers the front-side surface. To reduce the module design from a structural frame with glass mirror attachments to one where the structure itself is covered with a reflective film, it is important to understand how the structural backing material to mirror film affects the theoretical performance of the film. In particular, surface quality of the backing material was a point of concern in initial concept development. If the surface roughness requirement of the sheeting

material was such that a polished surface was needed to ensure mirror film performance, costs of large panels may be prohibitively expensive. However, if reflective films that are currently becoming commercially available could be used with standard materials, they are more likely to have a central role in new concept developments.

Of particular interest rolled galvanized steel, rolled aluminum, polished aluminum, fiberglass composite and gel-coated fiberglass composite were chosen for their availability and lower cost in sheet form. Galvanized steel sheeting, can easily be formed into the desired structural shape and is available in a range of thicknesses, however the surface quality is not smooth even to the naked eye. Aluminum sheeting is slightly more expensive but lighter weight and can be polished. However preprocessing of the surface would be significantly more costly and so is not desirable. Finally, fiberglass structures are also lightweight and can take the desired parabolic shape. The surface of composite structures is highly variable, depending on the mold quality and surface preparation as well as the use of a gel-coat that acts as a filler for many surface defects and can prevent environmental degradation of the resins. Given this range of materials, surface roughness measurements were used to compare surface compatibility with mirror films.

5.2 Measurements of Mirror Film Surface Roughness on Calibrated Surfaces and Potential Backing Materials

While it is known that film application on surfaces can have a smoothing effect on underlying surfaces, that effect depends on film thickness and assumptions about the regularity and nature of the surface details [65]. Surface roughness measurements of the standard materials and surfaces mentioned, including aluminum (as rolled), mirror polished aluminum, galvanized steel (as rolled), fiberglass composite and gel-coated fiberglass composite, before and after film application were used to understand the effects of backing surfaces on the final mirror film roughness. This same commer-

Figure 5-1: Zygo optical surface profilometer for surface roughness measurements.

cially available mirror film (Reflectech) was also tested by applying it to a calibrated surface gauge, which allowed a more general analysis based on known surface finishing processes rather than sample material.This combination of experiments allows for direct comparison of candidate materials while also referring to a calibrated surface so that results may be used in other areas.

5.2.1 Experimental Setup

To measure the initial surface before film application, a surface roughness standard comparator (ANSI B46.1) as well as $7.6cm \times 7.6cm$ square samples of mounting materials were scanned using a Zygo optical surface profilometer to determine characteristics such as average surface roughness R_a and peak-valley height R_t. For final surface measurement, a mirror film sample $7.6cm \times 7.6cm$ (0.1mm nominal thickness) was applied to each of the previously scanned samples. Hand rollers of four different hardnesses were used to apply film to the potential structural materials to account for potential biasing effects of the application process. One roller type was used to apply film to the nickel standard comparator surface. The samples were rescanned with the same optical surface profilometer setup to obtain surface roughness information
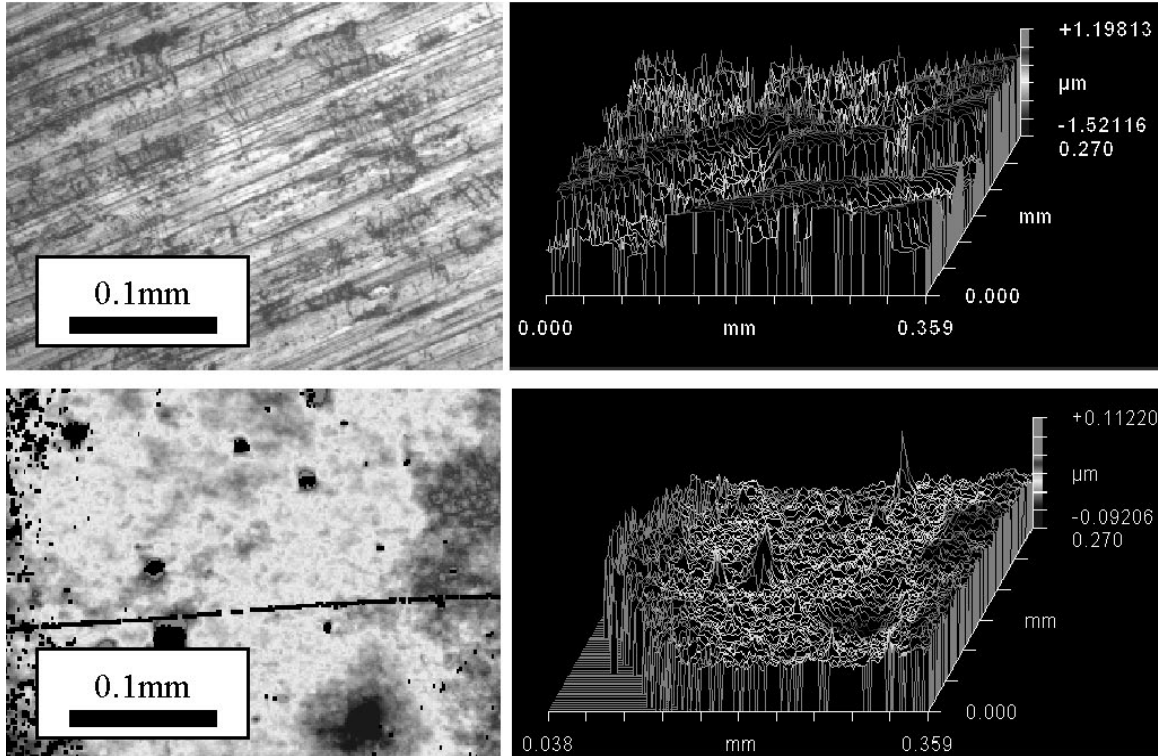
Figure 5-2: Surface scans of a rolled aluminum sample (above) and with mirror film applied (below) using Zygo optical surface profilometer.

with the film applied. Figure 5.2.1 shows the Zygo optical surface profilometer setup imaging a sample.

Gross surface defects, such as bubbles, were avoided in this particular measurement simply by visual selection of the testing area in the center of the sample plate. Measurements on backing materials were taken at three locations over the sample surfaces to prevent any local bias that could influence the measurements. There can be minor variations in roughness on the same surface finish sample, so the measurements can vary slightly depending on where it is taken. This slight position change between measurements offers a margin of error between the measurements before and after adding the film.

5.2.2 Measurements of Roughness Before and After Mirror Film Application on Backing Materials

Initial measurements of surface roughness on backing materials focused on the average roughness, R_a of the samples. Figure 5-2 shows example surface scans obtained by the experimental setup. The upper left image shows a close up of the rolled aluminum surface with typical directional ridge pattern. This surface is shown in the upper right as a 3D surface plot over an area of $0.359mm \times 0.270mm$. The lower left image then shows the rolled aluminum sample with mirror film rolled on the surface. The 3D surface plot on the lower right shows a much smoother surface profile with the average roughness approximately one tenth that of the original surface.

Average roughness values the five material samples is shown in Figure 5-3. The initial surface measurements are represented as the '0' roller hardness in the plot, with a range of average roughness from $0.024\mu m$ for the mirror polished aluminum sample to $1.068\mu m$ for the rolled steel sample. Both the fiberglass and gel-coat fiberglass, with average roughnesses of $0.230\mu m$ and $0.063\mu m$ respectively have initial surface roughnesses than the rolled metals, with rolled aluminum having an average roughness of $0.395\mu m$.

After the mirror film application, a reduction in average roughness to $0.026\mu m$ for an uncoated fiberglass sample, $0.019\mu m$ for as rolled steel, $0.016\mu m$ for a gel-coated fiberglass, $0.012\mu m$ for both mirror polished aluminum and as-rolled aluminum was shown over all roller hardnesses (Figure 5-3). Over all materials and samples a range of $0.009\mu m$ (mirror polished aluminum) to $0.047\mu m$ (fiberglass) was measured when the mirror film was applied. Hardness of the roller used during film application showed no trend in the effect of final average roughness over the materials, with all hand rollers showing significant smoothing of the surface. In particular, it should be noted that the rolled steel and aluminum samples showed equivalent final average roughness values as the final polished aluminum sample.

Final results of the average surface roughness measurements for the mirror film samples on five potential backing materials support the use of alternative backing

Average Roughness of Mirror Surface vs. Mirror Surface Application
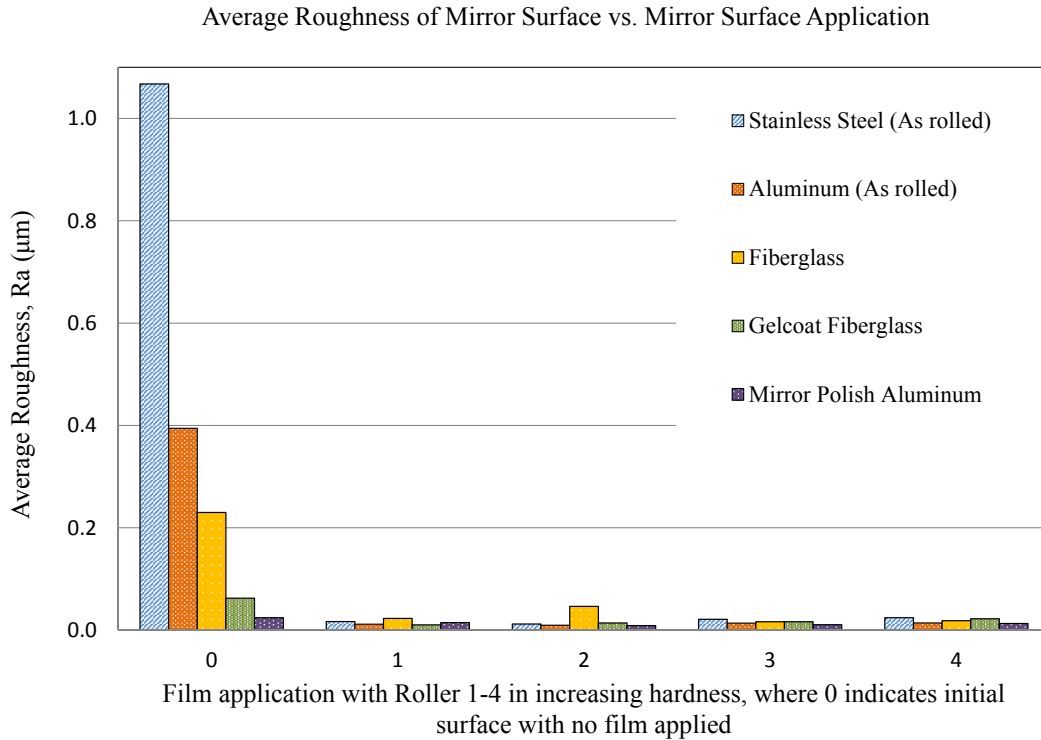
Figure 5-3: Average roughness of mirror film application on collector structure materials for differing application rollers.

materials for mirror film applications. Gel coated fiberglass, rolled aluminum and rolled steel show similar levels of surface roughness as more expensive polished aluminum backing materials, making them suitable replacements as far as roughness is concerned.

5.2.3 Measurements of Roughness Before and After Mirror Film Application on a Calibrated Surface

Calibrated surface roughness measurements of milling and grinding processes focused on the peak-valley measurements, which is the distance from the tallest peak to the lowest valley of the surface and whose values generally fall within the micrometer range ($0.1\mu m - 10\mu m$). The calibrated surface finish standard provides sample sur-

faces for horizontal milling and grinding with six average roughness values for each of the two finishing processes. Initial measurements were taken on the nickel ANSI B46.1 prepared surface and final measurements refer to the surface with the mirror film applied.

Figure 5-4 shows the peak-valley roughness values for horizontal milling and grinding before and after film application as a function of the surface's average roughness. The initial peak-valley measurements ranged from 1.507 micrometers to 7.116 micrometers for the grinding surfaces, and peak-valley measurements ranged from 1.693 micrometers to 5.548 micrometers for the horizontal milling surfaces. After the mirror film application, the final grinding peak-valley roughness measurements ranged from 0.001 micrometers to 0.166 micrometers. The final horizontal milling peak-valley roughness measurements ranged from 0.049 micrometers to 0.608 micrometers after the mirror film was added.

The surface smoothing effects of film application can be represented by the difference in peak-valley roughness as shown both in absolute terms and as a percentage reduction of the original value, as shown in Figure 5-5. Measurements of the difference before and after film application in average peak to valley height for the surface standard were 96.5% reduction ($2.90\mu m$) for a ground surface and 92.5% ($2.97\mu m$) reduction for horizontally milled surface compared to the original peak to valley height (Figure 5-5). The percent reduction in the peak-valley measurements, as shown by the (orange) line plot, ranged from 82.40% to 99.96% reduction in roughness. The high and low reduction percentages for grinding were 99.96% and 94.60% respectively. The high and low percentages for horizontal milling were 98.38% and 82.40% respectively.

Peak Valley Roughness for Standard Surface
Before and After Mirror Film Application
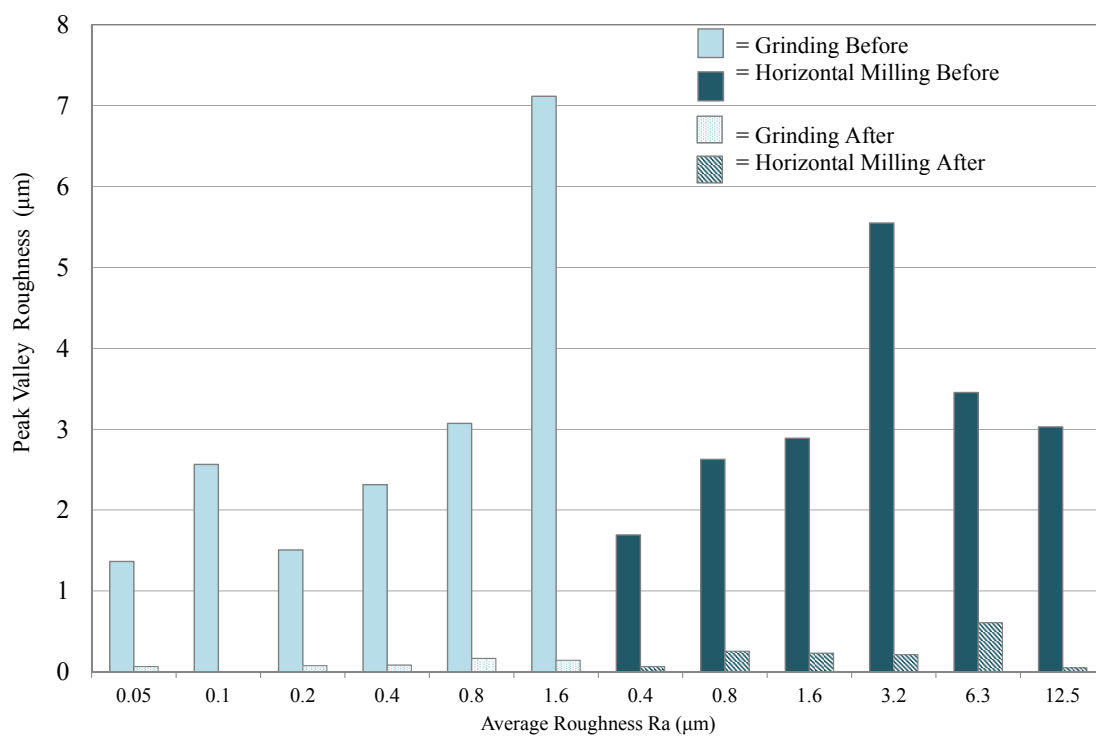
Figure 5-4: Peak to valley measurement before and after film application for standard grinding and horizontal milling surfaces.
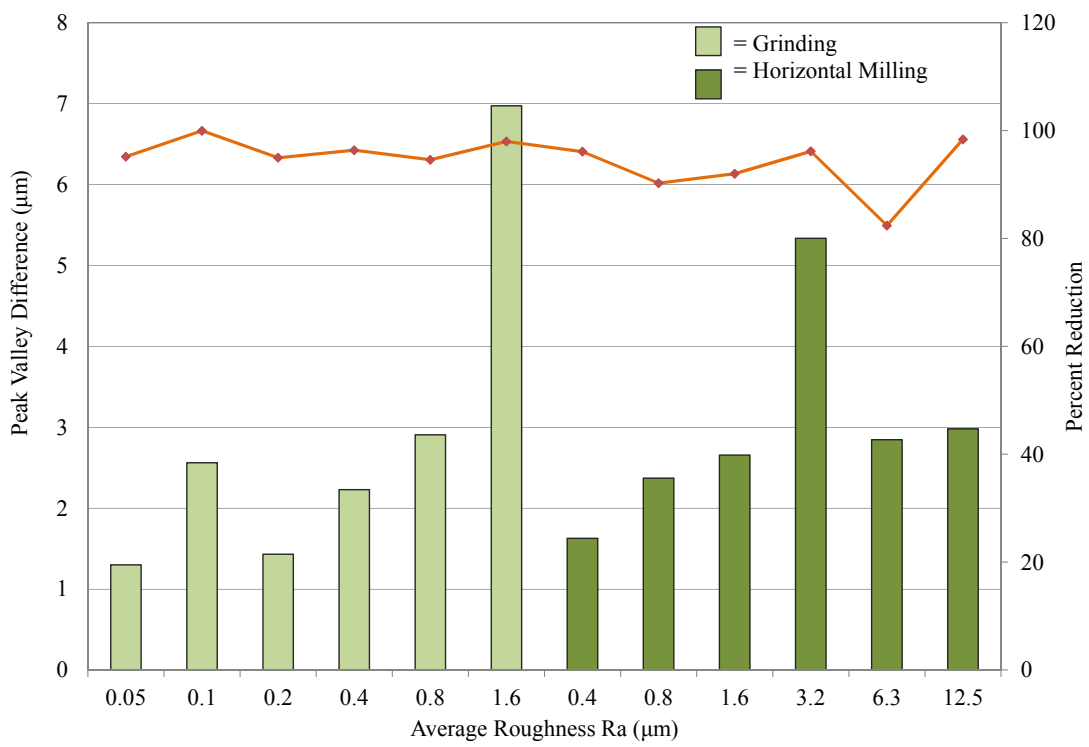
Figure 5-5: Difference in peak to valley measurement before and after film application for standard grinding and horizontal milling surfaces.
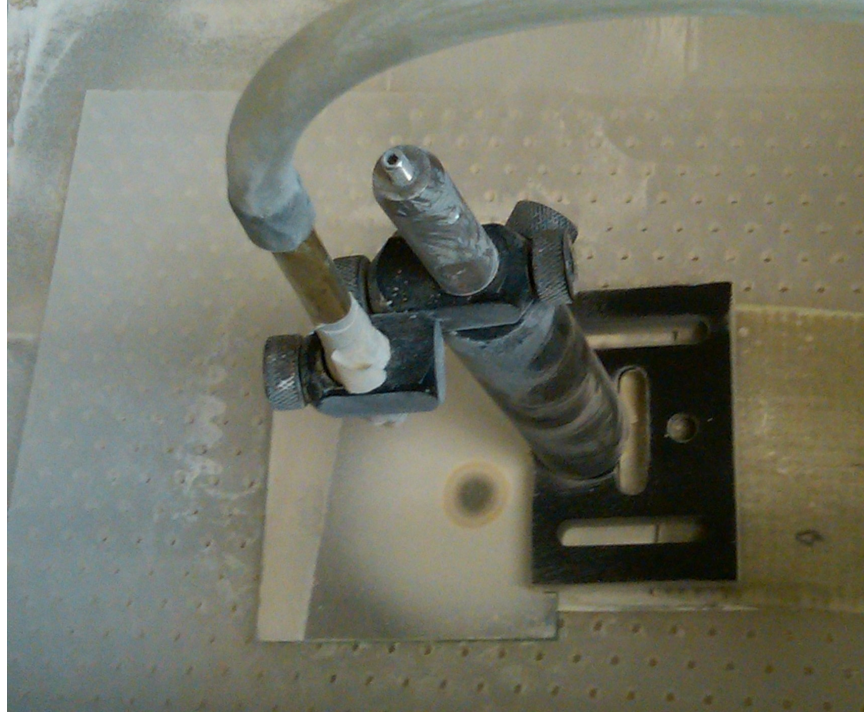
Figure 5-6: Experimental setup for surface erosion of mirror film on glass backing surface.

5.3 Mirror Surface Erosion with Quartz Particles and Resulting Performance Losses

Mirror surface performance is sensitive to the smoothness of the surface, where scratching of surface layers, and also the mirror layer when exposed, can reduce the operational efficiency of a solar trough module. When preparing mirror film surfaces for adhesion onto the backing material, the films generally have a protective layer on the surface, that is removed once the panel is in operation. However, once exposed to airborne particles over time, sudden surface bombardment such as in a sandstorm, and even scratching from the cleaning process, a mirror panel can quickly become damaged. To understand the durability of a commercial mirror film with respect to particle abrasion, measurements of efficiency as a function of distance from a central sandblasting stream were taken.

To test the surface degradation of a commercial mirror film a sample of material was adhered to the front-side surface of a borosilicate glass sample and placed in a

96

Figure 5-7: Mirror film sample after exposure to quartz directed quartz particle erosion with front-lit surface (left) and back-lit image of same sample (right).

tabletop sandblasting unit as shown in Figure 5-6. A calibrated MIL E-5007C Quartz was used as the abrasion material, which is both a comparable to coarser sands that impact mirrors in the field and compatible with the sandblasting unit without clogging (Appendix C). A 1mm diameter nozzle was positioned normal to the sample surface with the nozzle exit 85mm above the mirror film surface. A 150kPa (22psi) air supply was used to project the quartz particles for a duration of 26.1 hours until a breakthrough radius of 1.0mm was observed in the center of the film target which is shown from the front as well as when back-lit in Figure 5-7. Around the breakthrough diameter a larger transparent area of 1.95cm was also visible and can be seen in the back-lit image. After the particle abrasive removal of the surface, a spectrometer was used to measure the surface reflectance from 350nm-1100nm compared to the initial undamaged surface (Figure 6-18).

At the center of the mirror film surface where the stream of quartz particles were focused, the efficiency of the surface is 0.6% compared to the initial undamaged surface. The efficiency increases from 10% at 10mm from the center to 25% at 30mm from the center, but even at the farthest measurement 50mm from the surface, the surface is only 83% that of the initial surface reflectance. This surface erosion is a function of the layering and surface properties of the mirror film, so more information about the layering process is needed to generalize about surface abrasion rates over time. Such information would have to be made public by manufacturers [15].
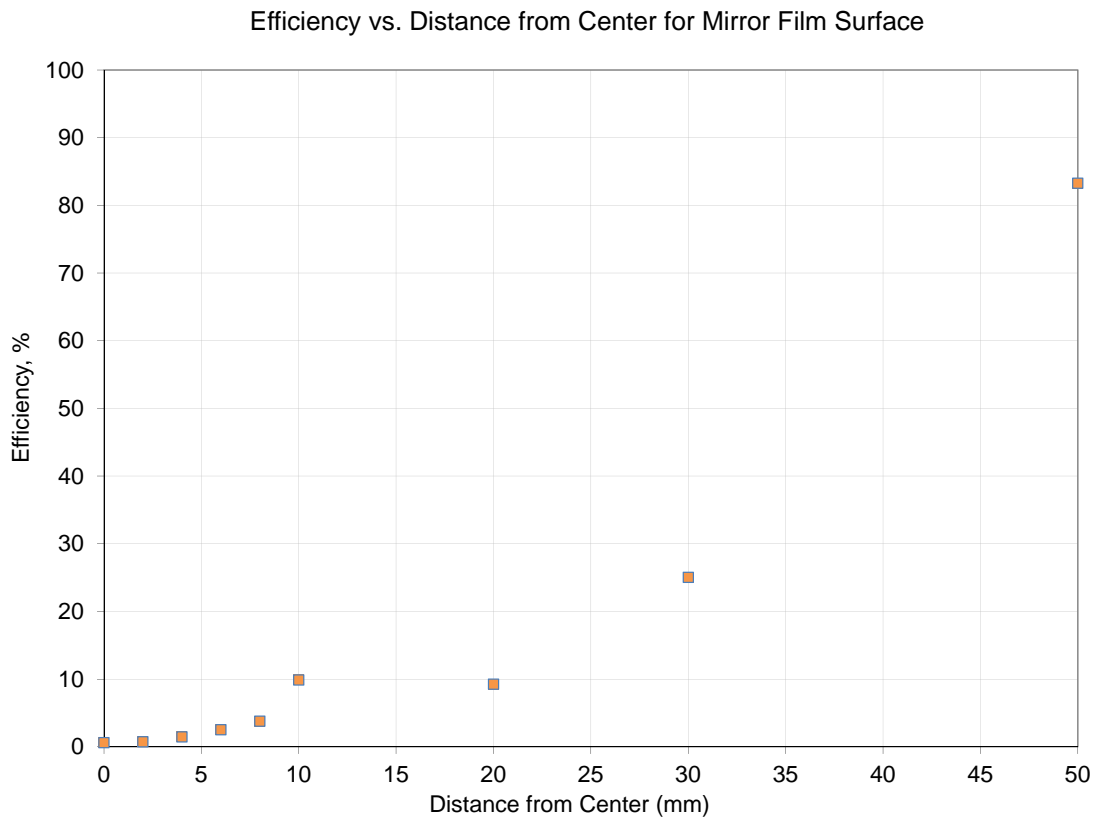
Figure 5-8: Efficiency of mirror film surface as a function of distance from center of jet impact zone.

Chapter 6

Contamination

Aerosols, a generic term to describe systems of small particles in air or another gas, and dusts in particular, which refer to solid particles produced by the breakdown of larger materials, are often deposited on solar collector surfaces during operation. Although mirror surfaces may be up to 95% efficient, the effectiveness of this surface is greatly reduced by such contamination [49, 15, 18]. By looking into the composition of dust deposited in typical solar field applications, and the means by which they cover the surfaces, more effective ways of reducing deposition and thereby increasing overall solar collector efficiencies in operation may be found.

6.1   Material Information and Size Distribution

The composition of dust particles and the range of individual particle sizes affects not only how quickly contaminants will land on the surface, but also may be used to understand dominant forces that may remove them from a mirror surface. Airborne soils, with mean particle diameters on the order of 10μm, generally fall into the range of coarse aerosols (>1μm), although a significant percentage of the particles may also be in the medium (0.1-1μm) range [66]. The distribution of aerosol particles being deposited will greatly depend on local soil composition.

For testing of deposition and cleaning on mirror film samples, Arizona Medium Grade test dust as well as MIL E-5007C Quartz was used. Because the soil particle

Figure 6-1: Arizona Medium Test Dust (left) and Mil Quartz (right).

Table 6.1: Chemical Analysis of ISO 12103-1 Arizona Test Dust

Chemical	% of -Weight
SiO_2	$68 - 76$
Al_2O_3	$10 - 15$
Fe_2O_3	$2 - 5$
Na_2O	$2 - 4$
CaO	$2.0 - 5.0$
MgO	$1.0 - 2.0$
TiO_2	$0.5 - 1.0$
K_2O	$2.0 - 5.0$

distribution and composition has been evaluated for these materials, results can be interpolated for local conditions. Figure 6-1, for example, shows the color and size difference of an ISO 12103-1 Medium Arizona Test Dust compared to a MIL E-5007C Quartz. While the size of individual particles dominate transport properties and deposition rates overall, the chemical composition may also affect the surface interactions of particles with the mirror and are worth noting. For the Arizona Test Dust used in deposition experiments, approximately 68%-76% by weight of the soil makeup is silicon dioxide SiO_2, commonly known as quartz. The dust also contains other oxides such as: aluminum oxide, or alumina at 10%-15%, iron (III) oxide at 2-5%, and smaller amounts of common oxides shown in Table 6.1.

The composition of a soil sample can generally be fit to power law distribution of particle count per diameter range, as is common for erosion processes. Figure 6-
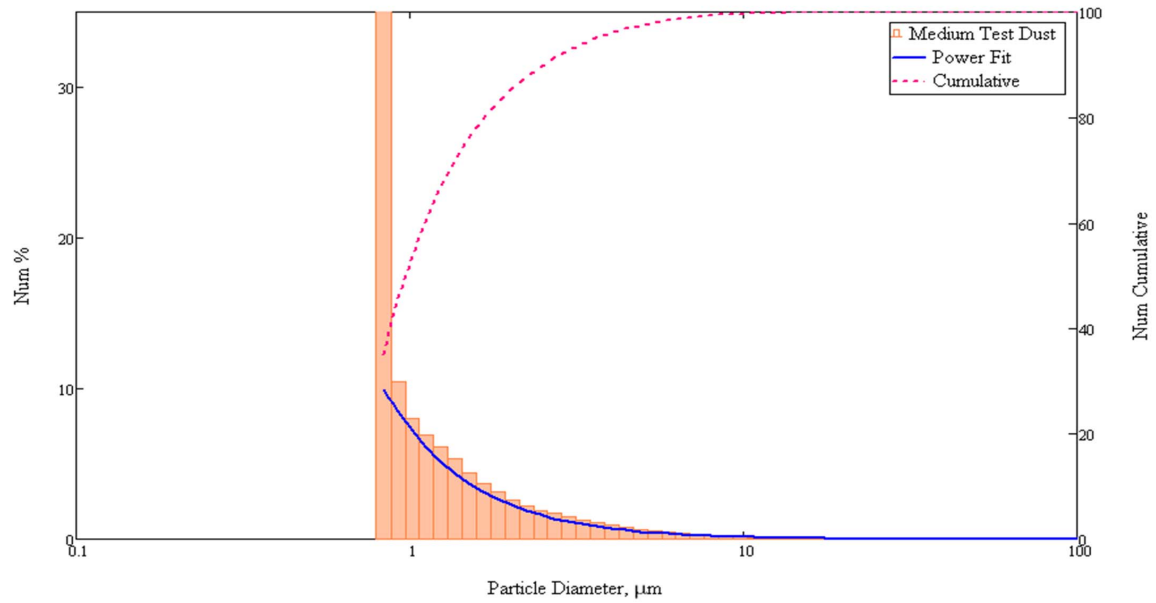
Figure 6-2: Number Distribution as a Function of Particle Size of ISO Medium Test Dust
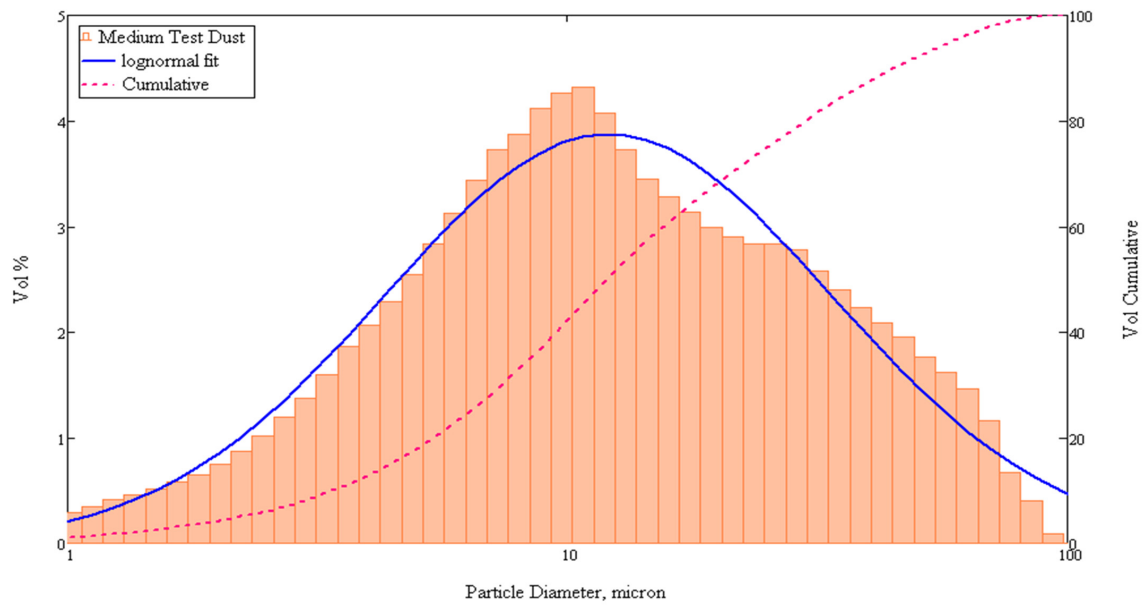
Figure 6-3: Volumetric Particle Size Distribution of ISO Medium Test Dust

2 shows the distribution of Arizona Medium Test dust, with the numerical percent distribution as a function of particle diameter, as well as the cumulative numerical percentage and the power fit of the distribution. Limits of the sample filtration were 0.711μm to 109.4μm. The power fit of the Arizona Test dust sample is given by Equation 6.1 where d_p is the particle diameter.

$$n_{ps}(d_p) = 7.335 d_p^{-1.678} \tag{6.1}$$

Given this distribution of particle count, it should be noted that even for samples where the average particle diameter is 10μm, the mode in terms of number of particles for a given diameter is less than 1μm, and in fact roughly 50% of all particles are less than 1micron. The volumetric distribution of particles shows dust composition as a function of diameter. In this representation, a log-normal fit of particle size is shown over the volumetric distribution as well as a cumulative volumetric percentage in Figure 6-3. This fit is described by Equation 6.2 [66].

$$n_v(d_p) = \frac{A}{d_p s \sqrt{2\pi}} \exp\left[-\frac{(\ln d_p - m)^2}{2s^2} \right] \tag{6.2}$$

The fit parameters in particular for the Arizona Test Dust used for experiments are given by:

$s = -1.03$

$m = 3.55$

$A = -204.75$

From this plot in Figure 6-3 one can see that the average particle diameter in terms of volumetric percentage is 12.09μm with the mode 11.28μm. Full details on the statistical distribution table can be found in Appendix C.

6.2   Deposition

As airborne contaminants travel into the quasi-laminar sublayer around mirror panels, some particles will travel across the boundary layer to where they can interacts
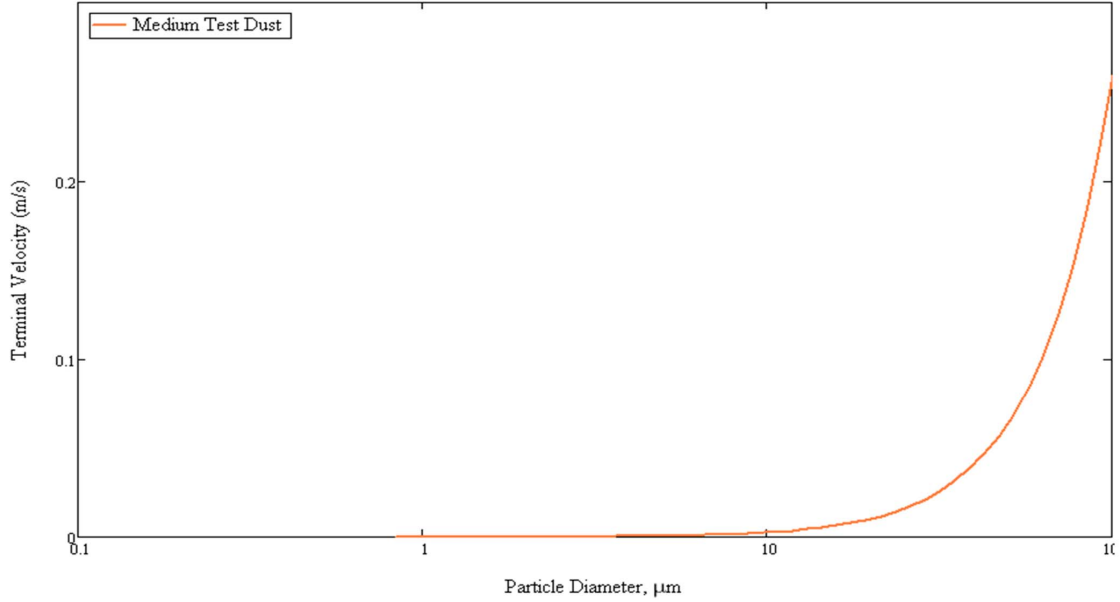
Figure 6-4: Terminal Velocity as a Function of Particle Size of ISO Medium Test Dust

physically with the mirror surface. While the rate of aerodynamic transport is generally set by conditions related to the installation site, boundary layer transport and surface interactions can depend on positioning of the mirror surface and collector structure, with the rate of deposition being determined by the slower of the two [67].

Gravitational sedimentation, where the gravitational force on particles as given by Equation 6.3 is compared to drag on the particle, describes the terminal settling velocity of the particle by Equation 6.4.

$$F_g = \rho_p \frac{4}{3} \pi \left(\frac{d_p}{2} \right)^3 g \qquad (6.3)$$

$$v_{term} = \frac{\rho_p d_p^2 g}{18 \mu} \qquad (6.4)$$

The settling velocity as a function of particle diameter for a dust particle density ρ_p of $1025 \, kg/m^3$ and dynamic viscosity of air, μ, at $1.8 \times 10^{-5} \, N \cdot s/m^2$ is shown in Figure 6-4 [68].

Given the particle size distribution of the test samples in the previous section, the rate at which a horizontal surface is covered by settling particulate matter can be

103

related to the particle size distribution if a particle count per volume of air is assumed as in equation 6.5

$$n_p(d_p) = \frac{C_t}{100} n_{ps}(d_p) \tag{6.5}$$

From the given aerosol distribution based on the test dust distribution, the total projected area of the material sedimenting from a stationary fluid can be described by Equation 6.6 [66]

$$s_{sedimentation} = \int_0^{\infty} \left(\frac{\pi d_p^2}{4}\right)\left(\frac{\rho_p d_p^2 g}{18\mu}\right) n_p(d_p)d(d_p) \tag{6.6}$$

Assuming a particle count, C_t, of $100\,particles/cm^3$ and evaluating particles between 1μm-100μm the sedimentation rate of the test samples would be:

$$s_{sedimentation\,medium} = \sum_1^{100} \left(\frac{\rho_p g \pi d_{px}^4}{72\mu}\right) n_p(d_{px})d(d_{px}) = 0.00236\,\frac{1}{s} = 2.36 \times 10^9 \frac{\mu m^2}{m^2 s} \tag{6.7}$$

The mass rate is also related by Φp from Equation 6.8 and for the particular range of Arizona test dust as given by Equation 6.9[66].

$$\phi_p = \int_0^{\infty} \left(\frac{\rho_p \pi d_p^3}{6}\right)\left(\frac{\rho_p d_p^2 g}{18\mu}\right) n_p(d_p)d(d_p) \tag{6.8}$$

$$\phi_{p\,medium} = \sum_1^{100} \left(\frac{\rho_p \pi d_p^3}{6}\right)\left(\frac{\rho_p d_p^2 g}{18\mu}\right) n_p(d_{px})d(d_{px}) = .1245\,\frac{g}{m^2 s} = .4428\,\frac{kg}{m^2 hr} \tag{6.9}$$

Additional particle deposition relationships based on moments of the particle count and diameter are also outlined by Friedlander [66].
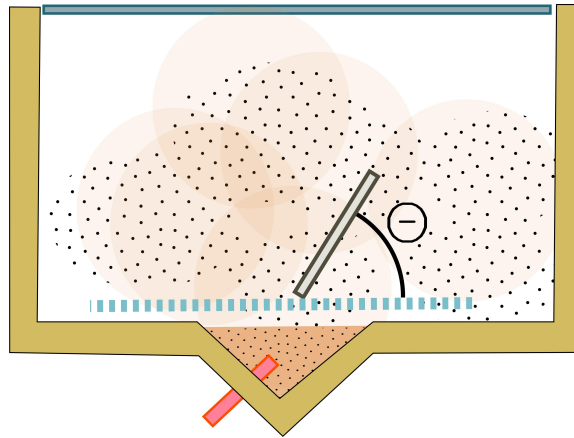
Figure 6-5: Diagram of Dust Chamber

6.2.1 Baseline Deposition Rates

In order to understand how to effectively remove deposited dust particles and prevent deposition of fouling materials, baseline studies on the effect of surface angle on accumulation and efficiency were conducted on samples of solar reflector materials. Two samples sets, one with a backing of 16 gauge galvanized steel and front surface of reflective mirror film and the other with a borosilicate glass backing and front side mirror film surface were tested in a dust chamber. Each square sample, being $58 \, cm^2$ in frontal area, was placed individually in the center of the dust chamber at angles of 0 to 180 degrees in 15 degree increments by means of a backside angle plate (Figure 6-5).

Controlled deposition of ISO 12103-1 Medium Arizona Test Dust for a period of 20 minutes was achieved by flowing air at 172kPa (25PSI) from a 1mm diameter nozzle placed in the lower section of the dust chamber to approximately 5cm below a reservoir of dust. A protective film covering the mirror film surface to prevent scratching and contamination was removed immediately before testing and sample the mass was measured immediately before before and after being placed in the dust chamber using a Mettler Toledo AG204 Balance, which has a resolution of 0.1mg for up to 81g samples. The resolution of the balance set the limit on maximum size of the samples as well as the minimum accumulation time such that a significant mass change could be measured. To understand the variation in deposition rate

Figure 6-6: Mass measurement with Mettler Toledo Balance

with time, a longer 120 minute deposition at 45 degree pitch angle was conducted
for a film sample with the mass being sampled every 10 minutes. Measurements of
humidity and temperature were recorded during experiments to control for the effects
of moisture.

Results of the initial deposition measurements as shown in Figure 6-7 showed that
an average deposition rate of 1.66mg/minute over the 120 minute sampling time,
resulting in a total deposition of 184.2mg over the 120 minute test interval. A larger
initial variation in the change in mass was observed for the first five samples, but
did not significantly affect the overall deposition rate. Measured values per unit area
correspond to a deposition rate of $0.285g/m^2min$.

When evaluating deposition as a function of angle, as expected, larger amounts of
dust appear on surfaces with smaller pitch angles. Samples angled less than 45 degrees
showed a mass accumulation of 30mg-80mg per sample with maximum deposition of
$1.34mg/cm^2$ at 30 degrees for galvanized steel. For samples with pitch angles larger
than 90 degrees, dust accumulation on the surface of 1.2mg-7.5mg was observed for
steel samples, and a range of 0.1mg-14.5mg was observed for glass samples, with
a relatively constant rate of deposition regardless of angle between 90-180 degrees
(Figure 6-8). This result validates that a limit on the effect of gravitational cleaning
exists, where simply turning a mirror surface will remove only some particles.
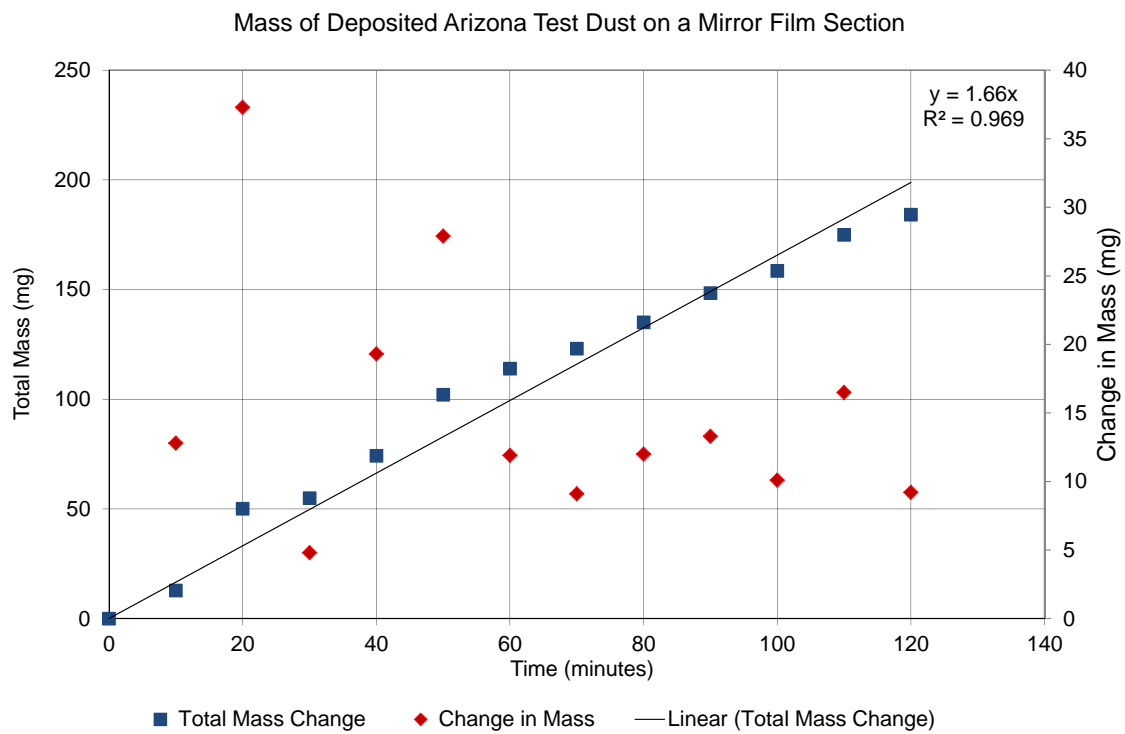
Figure 6-7: Mass of Deposited ISO Medium Test Dust on a 45 Degree Mirror Film Sample Over 120 Minutes
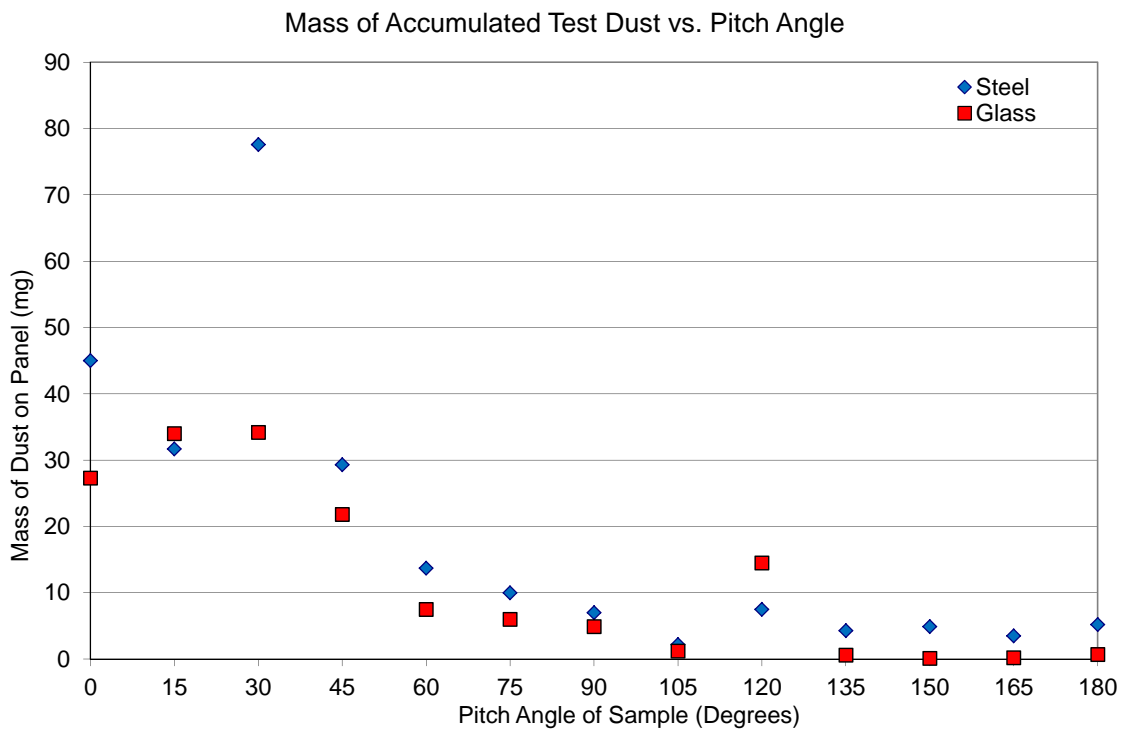
Figure 6-8: Mass of deposited dust as a function of surface inclination angle (20 minute exposure).

6.3 Surface Interactions

Once a particle settles on the surface of a solar panel, surface interactions, in particular electrostatic forces and van der Waals forces between the particles and the mirror film, can make removal difficult. The electrostatic charge relationship between a particle and a surface can be described by Equation 6.10, where q is the charge and z_0 is the charge separation distance and d_p the particle diameter and ϵ_0 the permittivity of free space [69].

$$F_e = \frac{1}{4\pi\epsilon_0}\frac{q^2}{z_0^2} \tag{6.10}$$

If the charge is assumed to be proportional to the square root of the particle diameter as shown in Equation 6.11, then the electrostatic force on a particle is given by Equation 6.12 [67].

$$q = n \cdot e \approx 2.37\sqrt{d_p} \tag{6.11}$$

$$F_e = \frac{1}{4\pi\epsilon_0}\frac{5.62d_p}{z_0^2} \tag{6.12}$$

Similarly, if the charge is assumed to be proportional to the square of particle diameter, such as suggested may be the case with triboelectrification effects (Equation 6.13) , and one gives the separation distance as related to the particle diameter (Equation 6.14) then the force from electrostatic charge attraction is given by Equation 6.15, where σ is the surface charge density [69].

$$q \approx 4\pi(\frac{d_p}{2})^2\sigma \tag{6.13}$$

$$z_0 \approx d_p \tag{6.14}$$

$$F_e = \frac{1}{4\pi\epsilon_0}\frac{(4\pi(\frac{d_p}{2})^2\sigma)^2}{d_p^2} = \frac{1}{4\pi\epsilon_0}(\pi\sigma)^2d_p^2 \tag{6.15}$$

This quadratic relationship holds only for small separation distances, and in general the assumptions of Hinds are used for the rest of this text.

In the case of quartz particles for which the Hamaker constant, A, for quartz silicon dioxide is 66×10^{-21} J, van der Waals forces are linear with respect to particle diameter where the separation distance is small, and follow from Equation 6.16 [67, 70, 71].

$$F_v = \frac{A d_p}{12 z_0^2} \tag{6.16}$$

From a plot of particle diameter as a function of force from equations 6.10,6.12,6.15, and 6.16, one may observe that surface interactions, such as electrostatic force and van der Waals forces, dominate the particle motion more than gravity for small separation distances. The 0.4nm separation distance of Figure 6-9, is generally the minimum distance of a particle surface interaction [70]. (Figure 6-9). Regardless of the electrostatic charge proportionality assumed, surface effects of van der Waals and electrostatic forces dominate for particles in the 0-200micron range of interest. This is why, from a design perspective, concepts involving simply turning a mirror surface or even vibrating a panel will have minimal effect on removing particles nearest to the mirror surface.

For a larger separation distance, such as with any subsequent layering of particles and microscopic offset, surface interaction forces rapidly decrease proportionally with $1/z_0^2$. Figure 6-10 shows gravitational, van der Waals and electrostatic forces on particles as a function of diameter for a particle with a larger, but still microscopic offset of 0.1µm. For small particles, this attractive force can be much larger than the force of gravity, which is why small particles are deposited on the surface of a mirror sample even when angled more than 90 degrees relative to horizontal. The cross-over particle diameter, where the dominant force changes, such as where gravitational force dominate over surface interactions, is sensitive to the assumptions of Hamaker constant for the material, and separation distance at the surface [70, 67, 66].
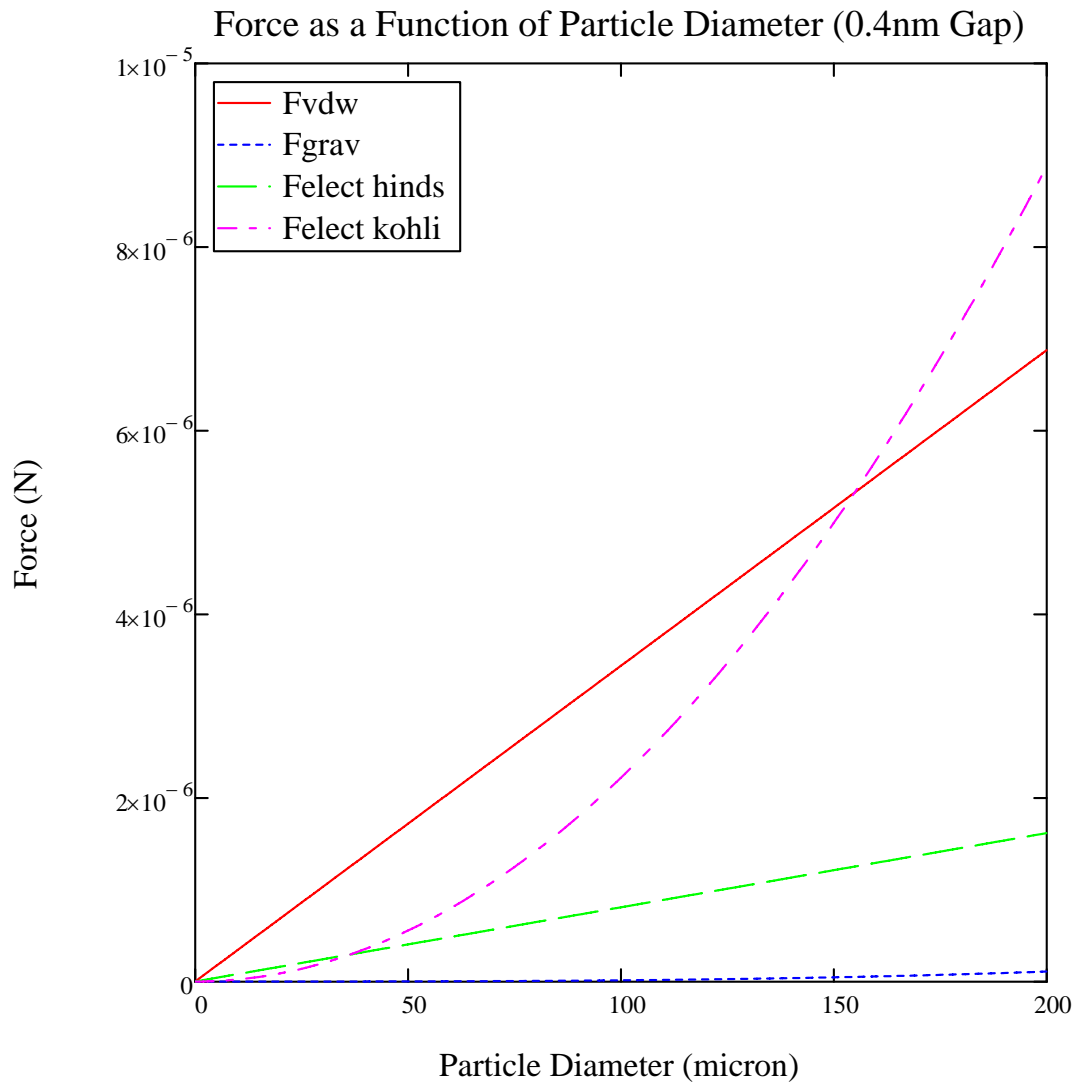
Figure 6-9: Force as a function of particle diameter for gravitational, van der Waals and electrostatic interactions for a 0.4nm gap between mirror and particle surface.
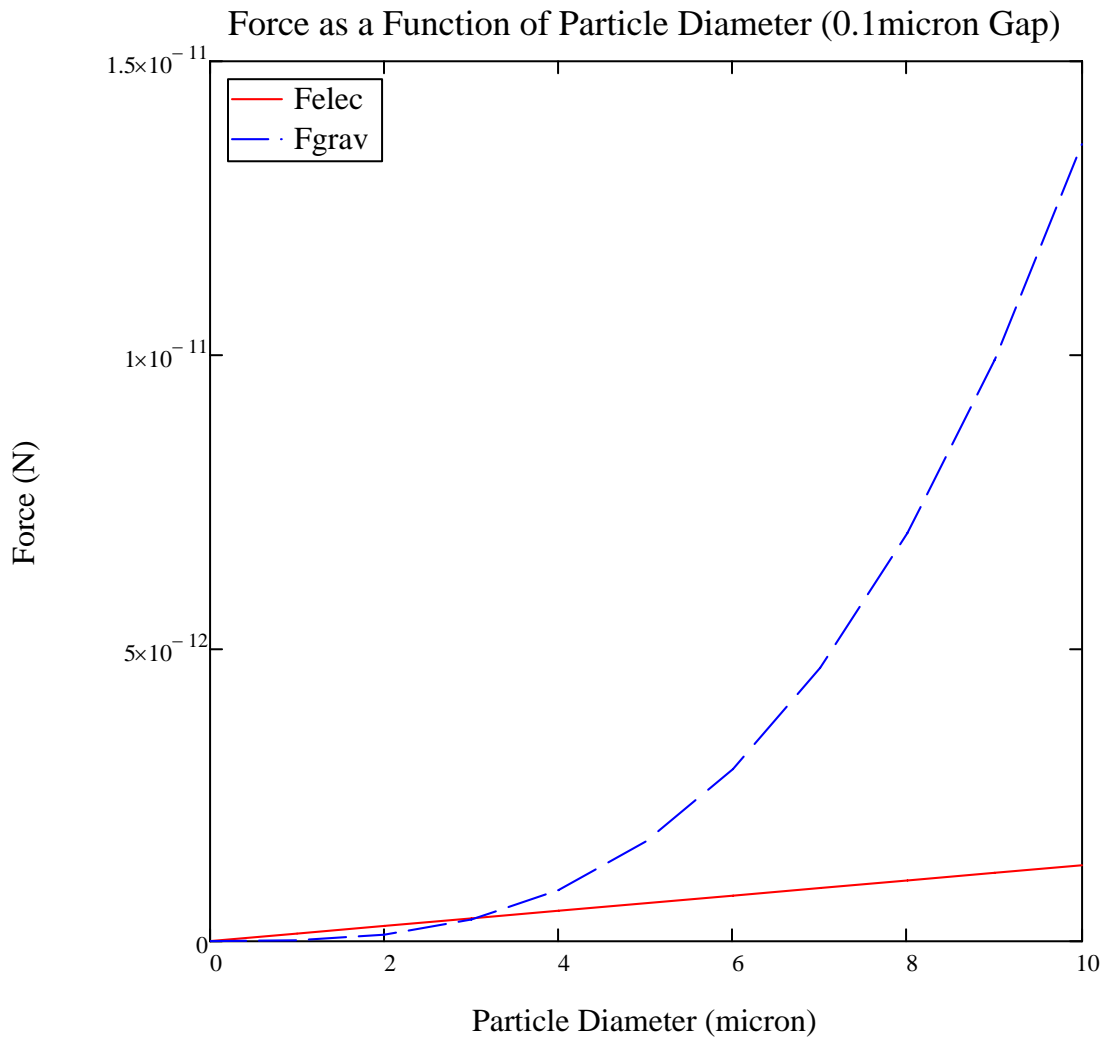
Figure 6-10: Force as a Function of Particle Diameter for a separation distance of 0.1micron

Figure 6-11: Inside dust chamber with mirror film sample

6.3.1 Surface Charge Measurements of Clean and Contaminated Mirror Film Samples

To understand more about the surface effects on contaminant deposition, the surface charge of mirror film samples adhered to galvanized steel and glass backing was measured using a static charge meter before and after the 20 minute contaminant deposition previously described in section 6.2.1 (Figure 6-11). Measurements were taken using a handheld surface DC voltmeter with 0-20kV range and 1V resolution offset 8mm from the sample surface in three locations over all samples (Figure 6-12). Measurements were repeated for inclination angles of 0-180 degrees in 15 degree increments and with humidity and temperature monitored. In addition, a 120 minute test of surface charge for a galvanized steel sample was conducted to determine whether test duration affected overall charge buildup.

Figure 6-12: Example samples before andafter testing.

Average surface charge for thirteen samples averaged over three locations for mirror film on galvanized steel and borosilicate backings is shown in Figures 6-13 and 6-14. From the data collected, the average surface charge over three locations of the mirror film samples on a galvanized steel backing showed an increase of approximately 150V from an average of -150V to 1.4V (Figure 6-13). Surface charges on the galvanized steel tend to a more neutrally charged surface after contamination. It is possible that triboelectrification over the sample neutralizes whatever charge the sample had before or that the measurement is simply measuring a neutral charge from the particles. Results for the glass-backed mirror film show a slightly different effect. The overall initial surface charge on the glass was much higher than that of the galvanized steel backed samples. Mirror film on the glass backed samples averaged over three locations vertically showed an initial average voltage over all samples of -40.3V before deposition and 34.5V after (Figure 6-14). Like the steel-backed samples, the initial surface charges on glass backing were all negative. Unlike the steel, however, after the dust deposition all but one sample of glass-backed film registered as positively charged. Unlike the steel however, the glass does not seem to neutralize post-contamination. There is a larger variation in final charge for the glass backed film samples, with the glass-backed samples positively charged after dusting.

It is possible to look at the same data set in more detail, looking at the variation in charge in the three locations separately and as a function of sample inclination angle. Figure 6-15 shows the surface charge before and after dust deposition on the

steel backed samples by location based on the inclination angle and Figure 6-16 plots the surface charge before and after dust collection by location of the glass samples for a given angle. For the galvanized steel samples, the largest difference in voltage between two adjacent locations was of 378 volts and a low of 5 volts, whereas the glass-backed samples had a high of 66 volts and the smallest difference was 2 volts. For galvanized steel backed film samples, the variation in charge over location decreases after contamination, and for glass-backed samples there is also a decrease in location variation, however not as pronounced.

When plotting test results as a function of sample pitch angle, Figure 6-15 shows no influence on surface charge with increase angle for the mirror film samples on galvanized steel. For the surface charge of the mirror film samples on glass in Figure 6-16, an increase in charge difference before and after contamination was seen for sample angles of 0-90 degrees, but this pattern breaks down for angles 90-180 degrees. This could be an effect of flow conditions in the chamber, with air flow velocity over the sample being relatively low and non-directional in nature.

To understand if there is a longer term charge buildup over time, the surface charge of a mirror film sample on galvanized steel was recorded over a period of 120 minutes. Results in Figure 6-17 shows an average charge of 30V and a range of 4V-70V, but no clear buildup or marked decrease over the duration tested. To determine the influence of environmental factors, before and after surface charges were plotted versus humidity and temperature. Relative humidity over all test sampling ranged from 44%-54% with an average 47.6% relative humidity. Ambient temperature ranged from 19.7 ° C to 21.2 ° C with an average temperature of 20.7 ° C. There was no noticeable correlation between either relative humidity or temperature and the change in surface charge. Therefore it can be concluded that the reported temperature and humidity fluctuations in the test environment had no measurable effect on the results.

While there were observed differences in surface charge before and after contamination for mirror film on galvanized steel, the varability of measurements over the surface, and the liklihood that van der Waals and other surface effects dominate particles at the surface, suggests that electrostatic control method on the panel surface

Figure 6-13: Average surface charge of a mirror film sample on galvanized steel before and after 20 minute contamination.

Figure 6-14: Average surface charge of a mirror film sample on glass before and after 20 minute contamination.
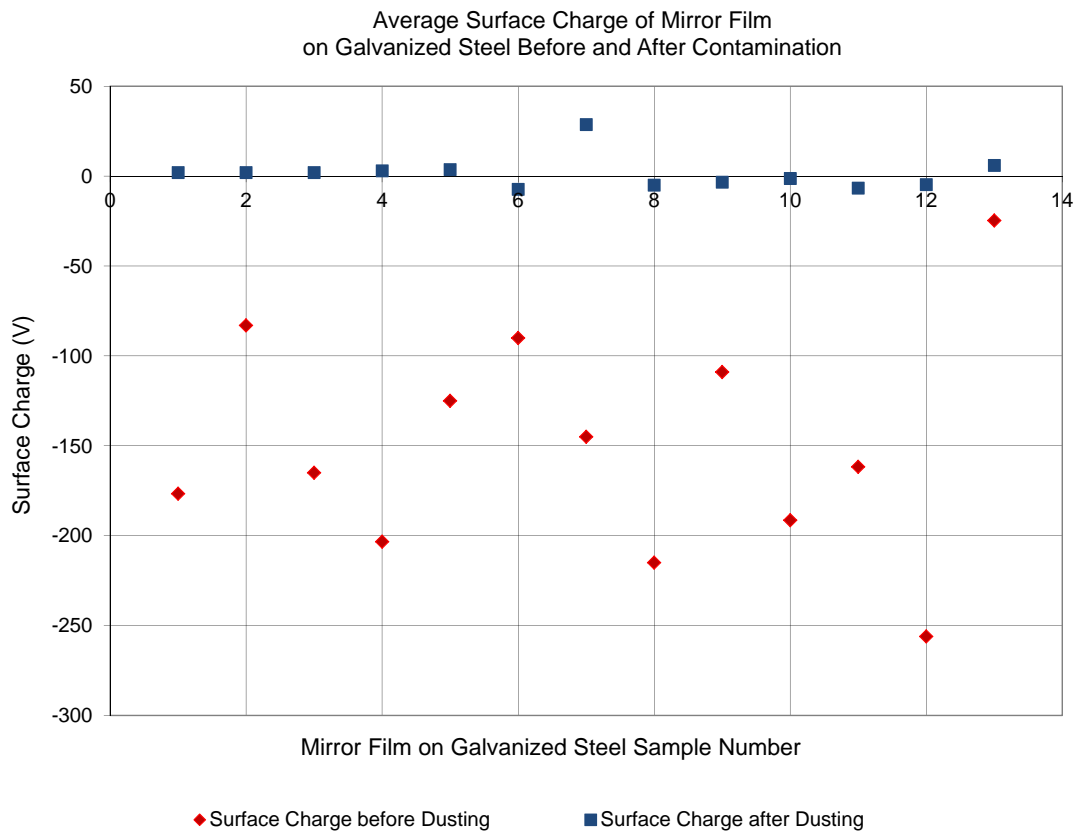
Figure 6-15: Surface charge of three locations on a mirror film sample on galvanized steel before and after 20 minute contamination.
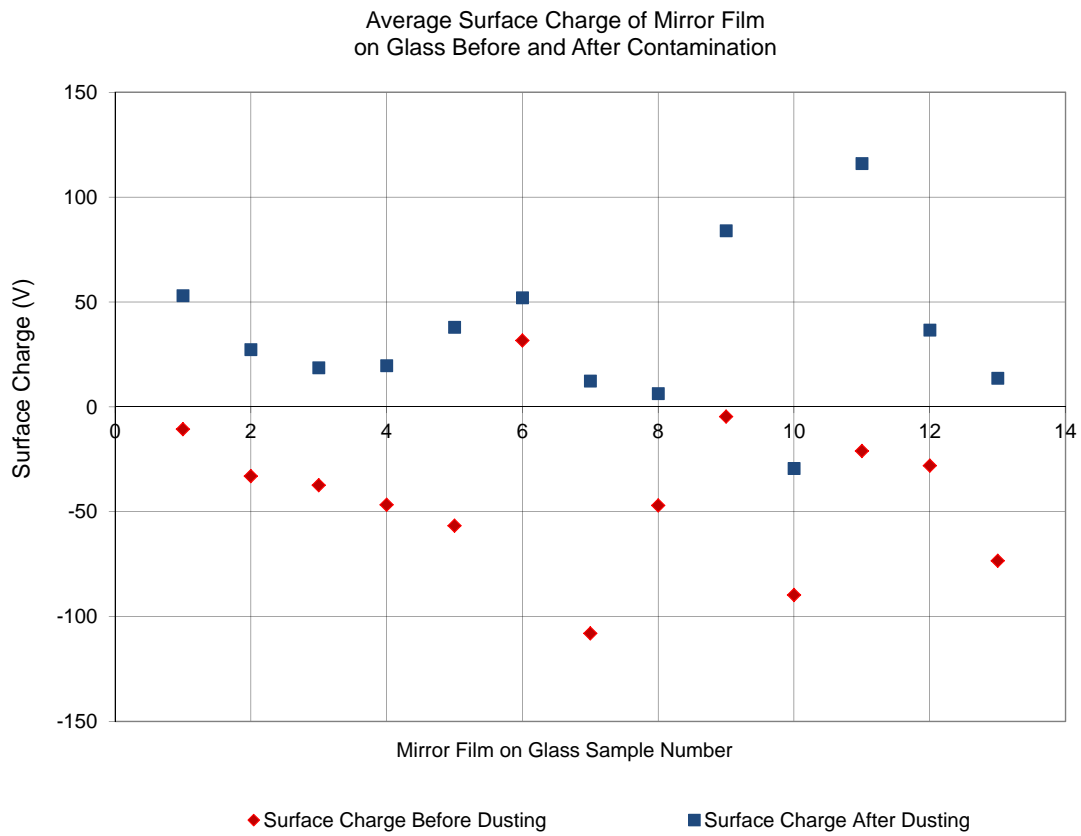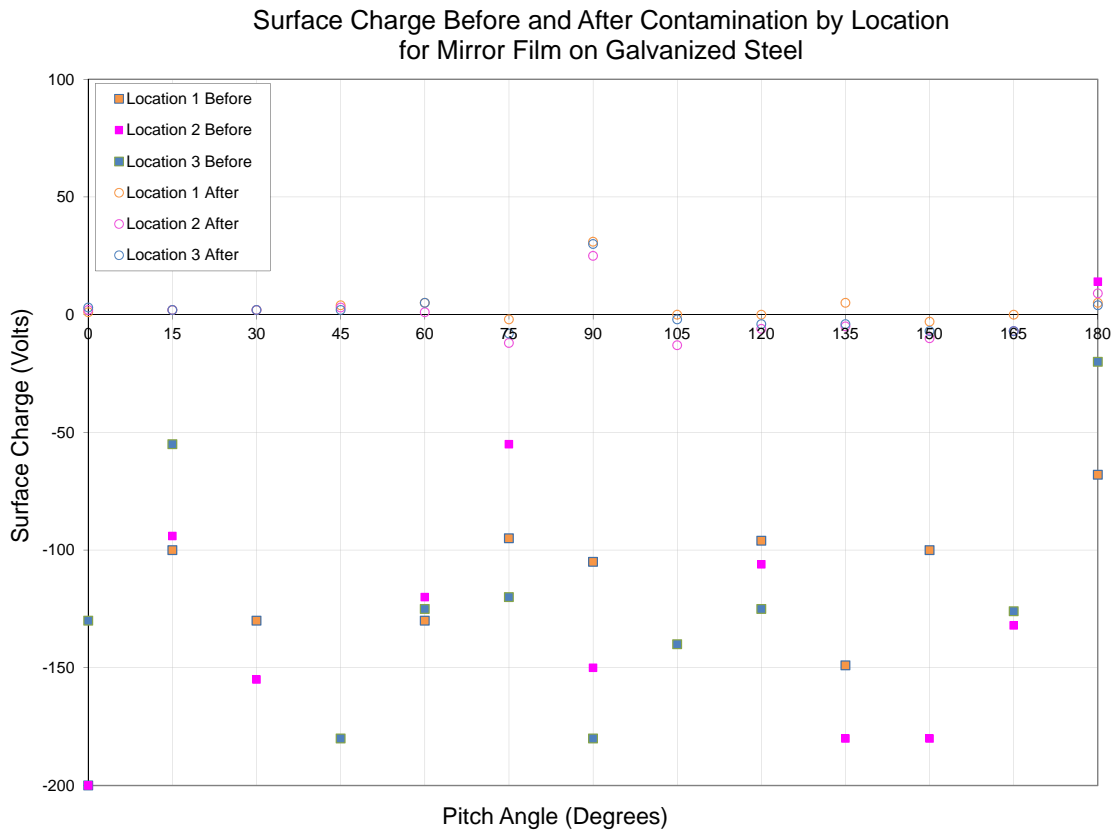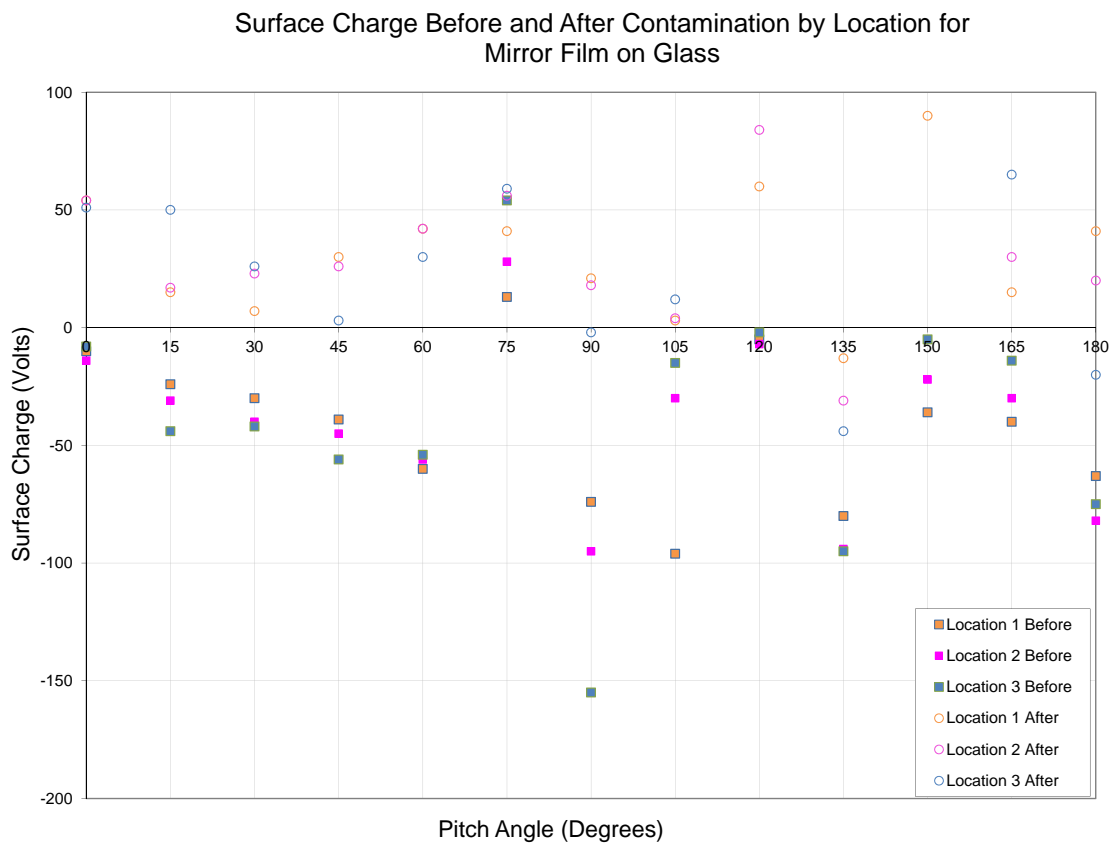
Figure 6-16: Surface charge of three locations on a mirror film sample on glass before and after 20 minute contamination.
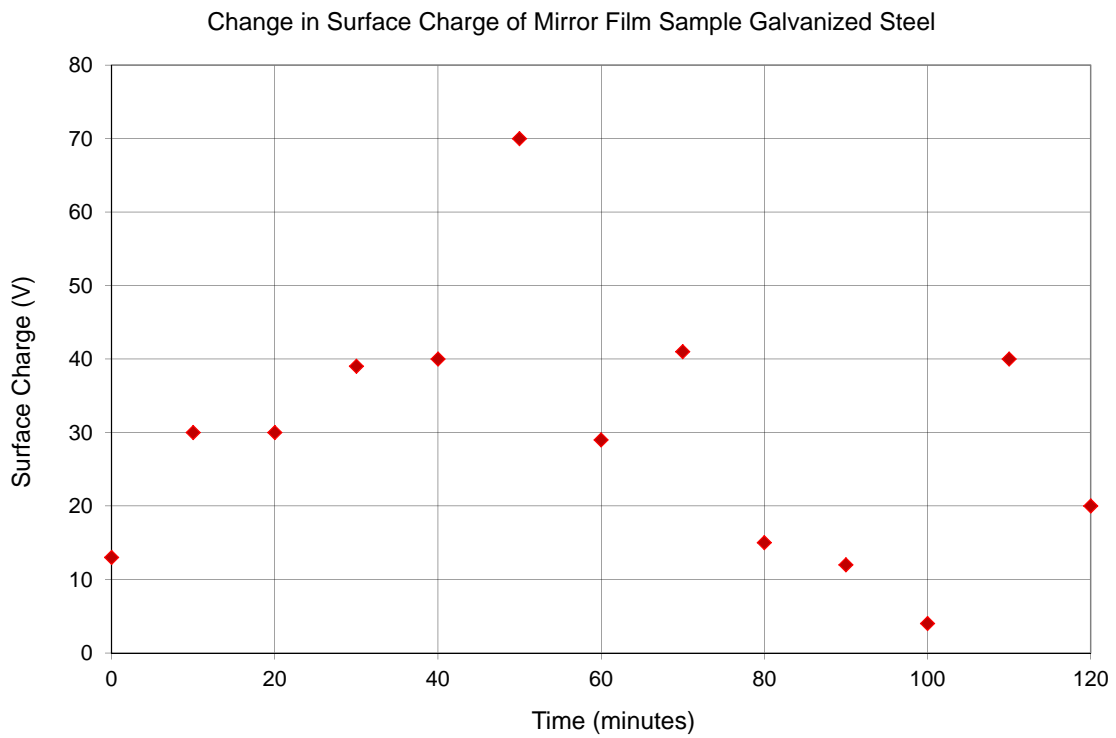
Figure 6-17: Surface charge of a mirror film sample on galvanized steel over 120 minute duration.

would not be effective. In addition, the since the surface of the film is mainly insulative, any electrostatic control method would probably have to use active ionizing particle delivery methods, which require high voltages and would result in another parasitic loss in the solar trough field. Perhaps developments in coatings for electrostatic control which do not interfere with film reflectivity could be used on mirror film panels, but such research is beyond the scope of this thesis.

6.4   Reflectivity Loss

To understand surface contamination effects on optical performance more directly, measurements of reflectance were conducted on the mirror film surface before and after contamination. In this experiment the front surface of mirror film samples on galvanized steel and glass backing materials were measured in three locations before and after contamination of 20 minutes in a dust chamber, as previously described. Thirteen samples of glass were layered on the front surface with a mirror film reflectance then placed in a dust chamber and inclined 0-180 degrees with 15 degree increments. Reflectance of the samples was measured using a Stellarnet Blue-Wave Spectrometer with 350-1100nm wavelength detector range and a complementing SL1-Filter tungsten halogen light source [72]. An in-line probe, consisting of seven exterior optical fibers and one receiver fiber (R600-8-VISNR) was used to allow for measurements normal to the front surface of the mirror film sample. A diagram of this setup is show in Figure 6-18. From this apparatus, a plot of the spectra, such as shown in Figure 6-19. Raw data measurements of spectral reflectance are reported in counts, where the reference spectrum for comparison of contamination is the initial spectrum labeled 'before.' To maintain a uniform initial intensity, the distance between the test surface and the light source and probe was fixed.

6.4.1   Average Reflectance

Average reflectance of the samples was calculated by integrating the count value of spectral reflectance from wavelengths 350nm-1100nm and averaging over each of three

Figure 6-18: Reflectance measurement arrangement of sample fiber optic light source and sensor with enclosure.

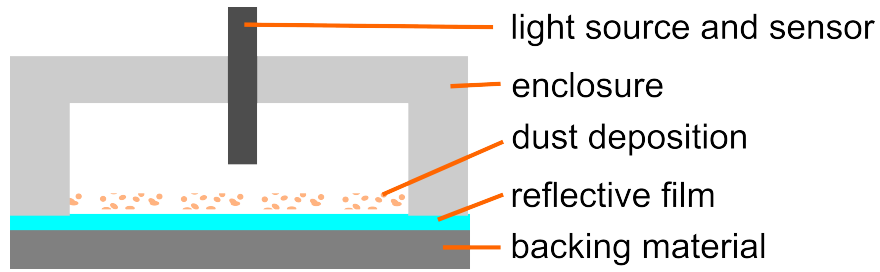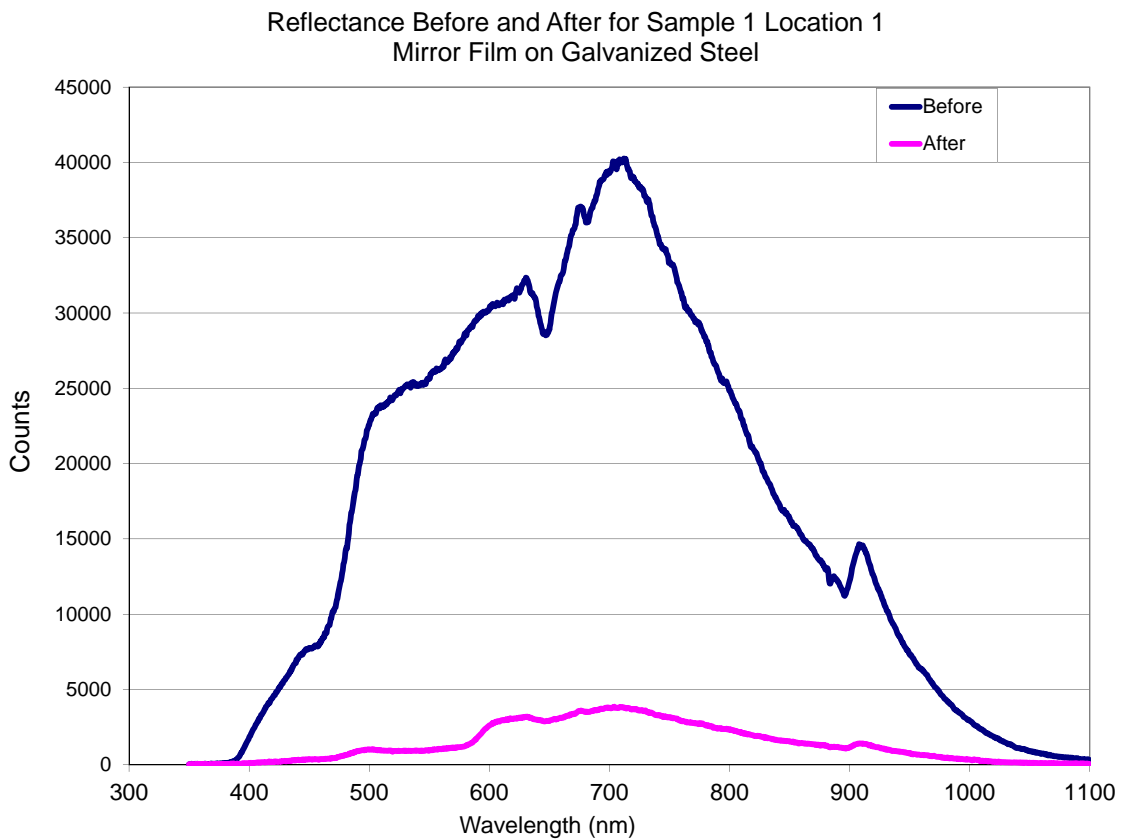Figure 6-19: Typical spectrum reflected from mirror film surface using Stellarnet SL1Filter light source.

locations per sample. Using raw count data rather than calibrated data allowed for more consistent zeroing of the spectral reflectance. In some datasets an observable offset was observed in the data, which could be removed by subtracting out the count values at minimum or maximum spectral range from the the data set. This zeroing was critical because integration of an inconsistent offset led to large errors in non-zeroed average reflectance data.

The average initial reflectance count of the glass samples was 2.0×10^7 as shown in Figure 6-20 and is consistent over all initial pitch angle measurements, as would be expected before testing if the samples were clean. After 20 minutes of dust contamination, the average total reflectance was significantly reduced for the pitch angles less than 90 degrees. The 0 degree pitch sample showed a post-contamination reflectance of 1.67×10^7 counts, with the reflectance increasing to 2.20×10^7 counts for 90 degree samples and then remaining withing the 2.0×10^7 to 2.20×10^7 range for samples between 90 and 180 degrees. The fact that the total average reflectance values of the 90-180 degree samples is larger than the initial sample measurements is largely due to small remaining offset differences in the spectral reflectance raw data, which over the 1500 discrete frequencies recorded can become significant when integrated. This general trend of low reflectance at small angles that levels out for angles larger than 90 degrees is consistent with the particle deposition measurements in Section 6.2.1.

The average reflectance before contamination of the galvanized steel backed samples (Figure 6-21) was also consistently around 2.5×10^7 in total. This level value for the clean samples is consistently higher than for the glass samples, which is most likely due to the slightly different count offset observed in the data. The measurements of reflectance after 20 minute deposition exhibited the same pattern as described by the glass samples, but with the 0 degree measurements at 4.3×10^6 count increasing to 2.0×10^7 counts at 90 degreees and then settling around 2.25×10^7 counts for measurements from 90-180 degrees. This data is consistent with larger amounts of dust on a sample for small angles, which results is a lower efficiency surface.
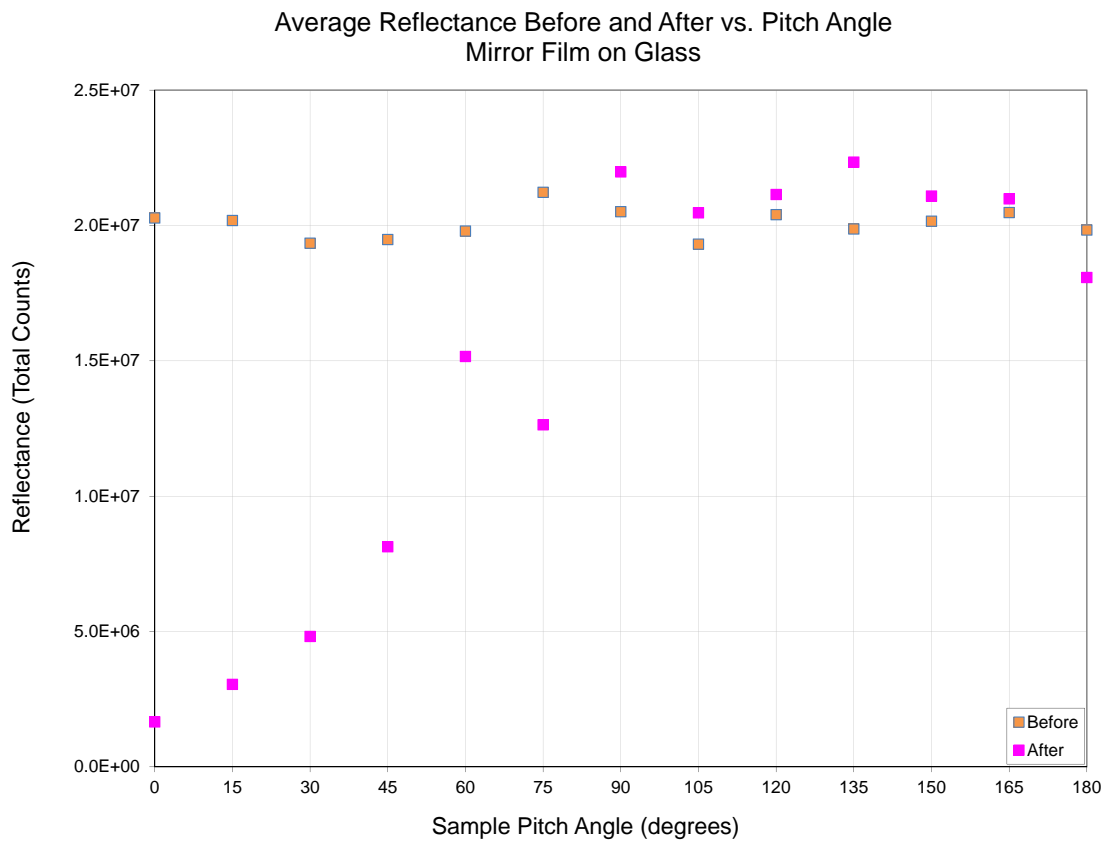
Figure 6-20: Average total reflectance on a mirror film sample on glass before and after contamination.
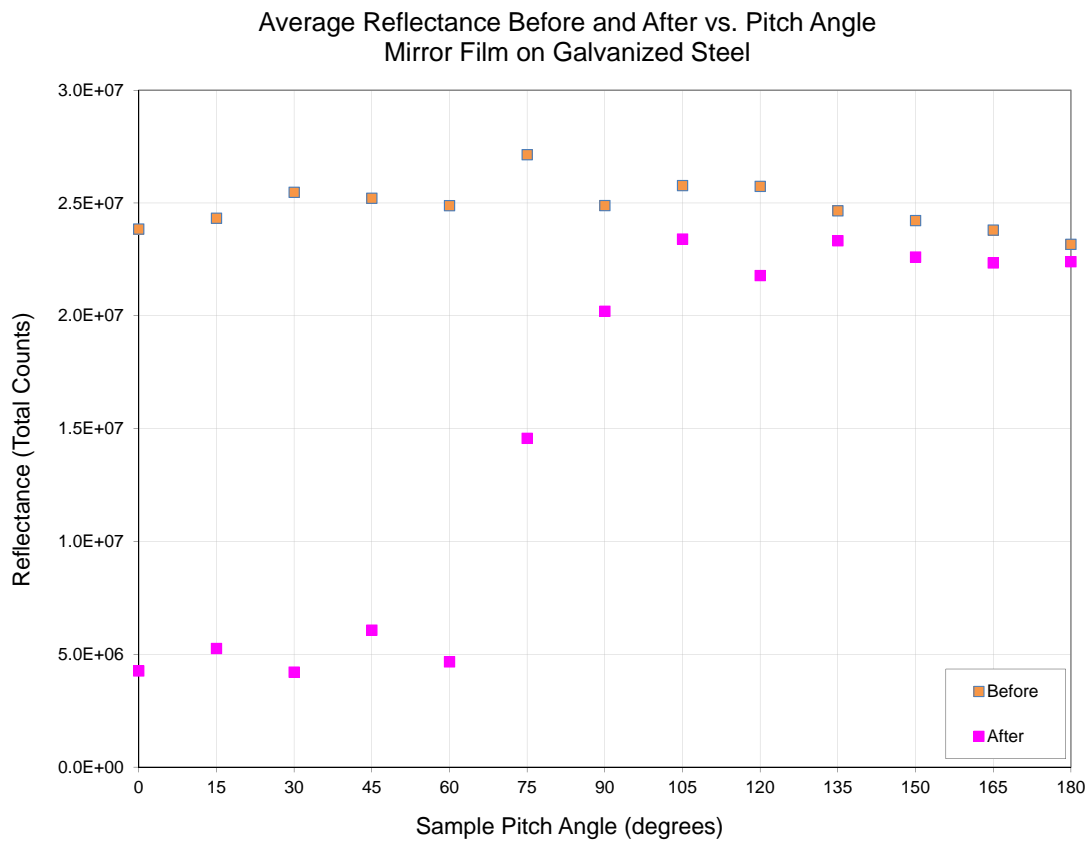
Figure 6-21: Average Reflectance on a mirror film sample on galvanized steel before and after contamination.

6.4.2 Surface Location Variation in Reflectance

To determine if there is any location bias on the surface, and to understand the variation in deposition for samples, the reflectance of the glass by location before and after dust deposition is plotted in Figure 6-22. The three test locations on the samples were located along the vertical center-line of the sample, with Location 2 at the midpoint vertically, Location 1 measured approximately 2cm below Location 2 and Location 3 positioned 2cm above Location 2. Before dust contamination of the surface, the reflectance measurements over the three locations show no bias, where one location is more reflective than the others, suggesting a uniformly clean surface. Differences in location variation range from a minimum of 2×10^5 counts for the 0 degree sample to 28×10^5 counts for the 105 degree clean sample. After the samples were placed in the dust chamber, the difference between maximum and minimum location measurements was smallest for the 0 degree sample, measuring 6.4×10^5 counts, and largest at 180 degrees where it measured 47×10^5 counts. The location measurement differences show a slightly larger variation in the contaminated surfaces, which would be expected because the surface is not perfectly evenly covered with particles.

Repeating the comparison of location variation for galvanized steel-backed samples, variations of the initial contaminated surface show comparable variations as seen for the film on glass backing and are reported in Figure 6-23. For initial uncontaminated samples a minimum of 4.8×10^5 counts at 180 degrees and a maximum of 63×10^5 counts 60 degrees was measured. Post deposition samples show a slightly larger variation, with the minimum location difference of 12×10^5 counts at 15 degrees and maximum variation of 246×10^5 counts at 30 degrees. This results provides support that the backing material does not significantly affect variation over location.

6.4.3 Reflectance Mass Comparison and Efficiency

From the raw count reflectance data, it is possible to calculate the surface efficiency as a function of inclination angle and dust collection mass using the initial clean surface as the reference. For both glass and galvanized steel backed samples, the efficiency
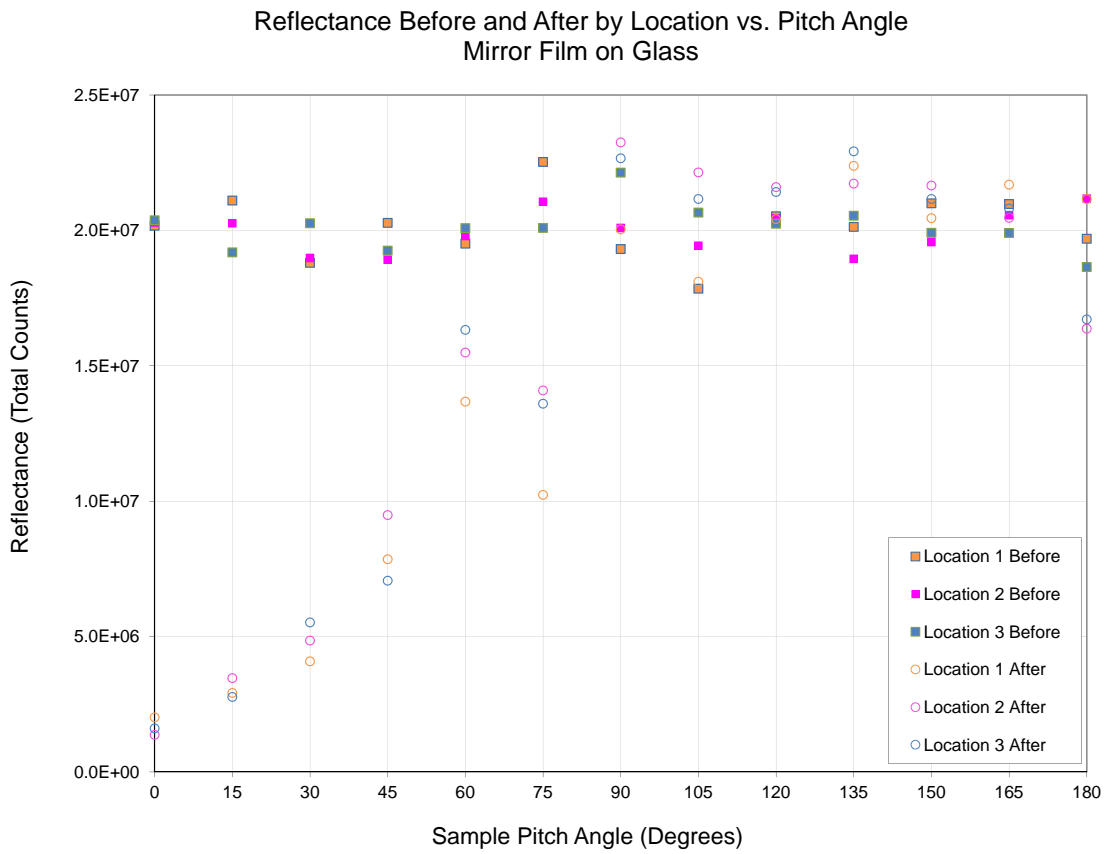
Figure 6-22: Reflectance of three locations on a mirror film sample on glass before and after contamination as a function of pitch angle.
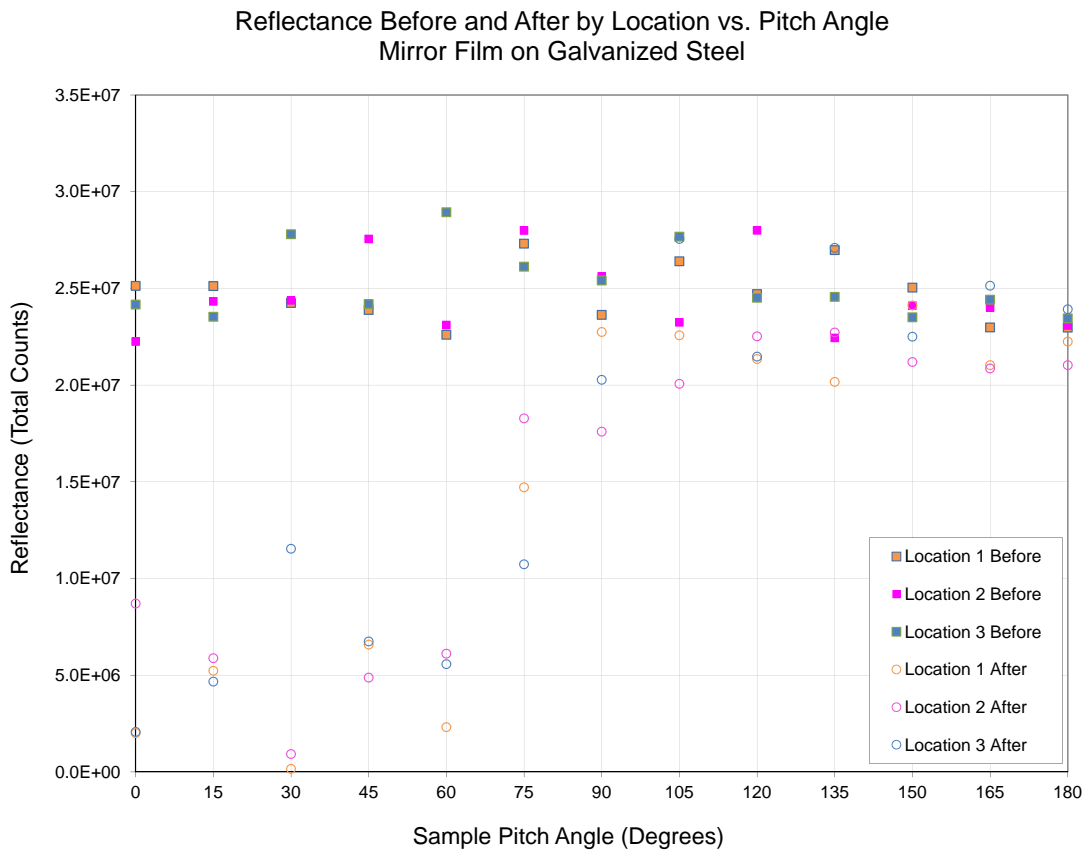
Figure 6-23: Reflectance of three locations on a mirror film sample on galvanized steel before and after contamination as a function of pitch angle.

of the contaminated surfaces is shown in Figure 6-24 as a function of the sample pitch angle during deposition. In this plot, the reference clean surface of galvanized steel was used for both samples to give a uniform reference and also because the offset error for the initial galvanized steel samples was significantly lower than that of initial glass samples. For both backing material sample tests, the efficiency at lower angles is significantly reduced compared to the clean surface, with glass backing samples at 0 degreees having an efficiency of 6.9% and galvanized steel backed samples at 0degrees with efficiency at 17.8%. The efficiency of contaminated surfaces improves with pitch angle up to 90 degrees with glass samples having efficiency of 88.3% and galvanized steel samples having efficiency of 81.2%. Pitch angles of between 90 and 180 degrees have level values of ranging from 80-91% for galvanized steel and 81-96.7% for glass. These values give an understanding of efficiency over a curved panel, to what extend angular position can affect deposition, and the efficiency loss that can be expected even with panels turned to greater than 90degrees.

A more direct correlation to be made with contamination of mirror surfaces in dusty outdoor environments is the amount of dust deposited and the resulting efficiency loss. For the particular Arizona Test Dust used, pitch angle of the samples is related to the more direct mass measurement to show efficiency as a function of mass of deposited dust in Figure 6-25. Efficiency for mass area deposition of less than $1g/m^2$ can already reduce the effectiveness of clean mirror surfaces to 80%-90%. The efficiency as a function of. mass area density fits an exponential function, where a mass density of $6g/m^2$ results in efficiencies of 15% compared to the uncontaminated surface. This particular efficiency to mass density relationship is dependent on preview explanations of particle size distributions, but provides a quantitative assessment of the significance that contamination plays in parabolic trough module effectiveness. Such results point to cleaning concepts as of major importance in successful solar plant operations. While each installation location may have unique particle distributions, particle counts, and resulting costs to clean, data on efficiency allows operations to determine ideal cleaning schedules and investment paybacks for cleaning systems.

Efficiency of Contaminated Sample with Respect Clean Mirror Surface vs. Pitch Angle
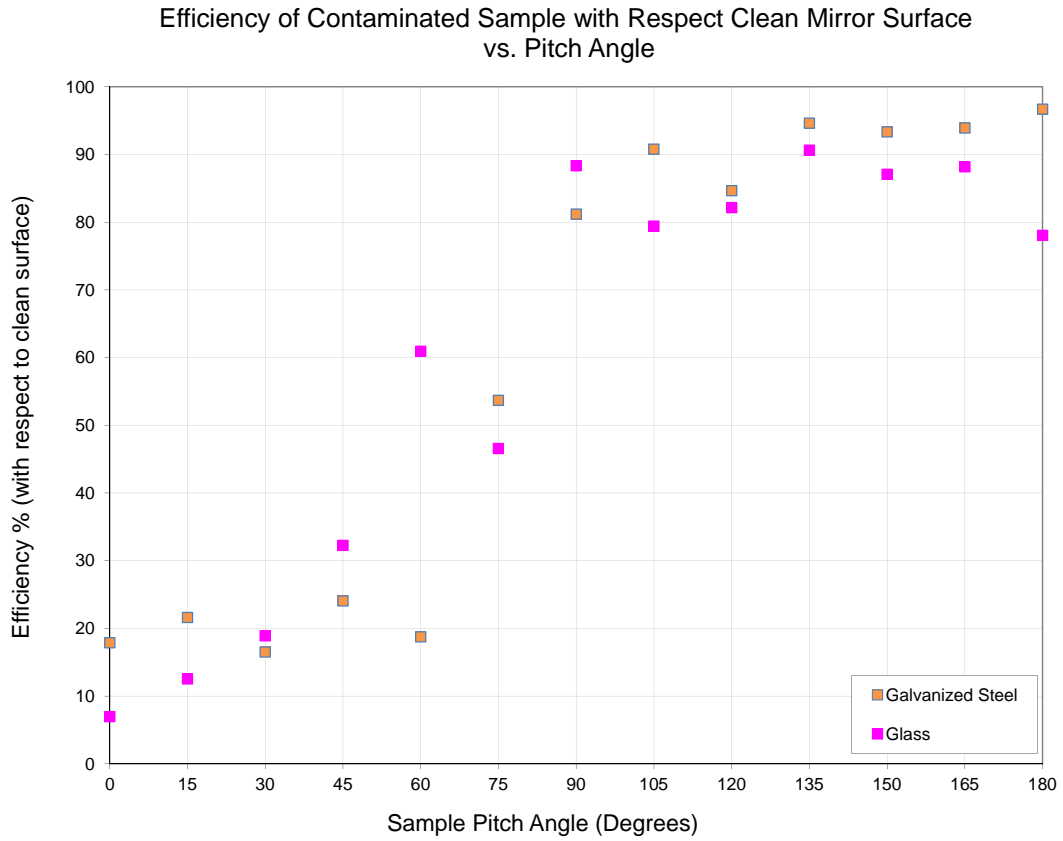
Figure 6-24: Comparing percent average reflectivity from the ratio of post-contamination output to the pre-contamination surface for a mirror film sample on galvanized steel.

Efficiency of Contaminated Sample with Respect Clean Mirror Surface
vs. Mass Area Density

Legend:
- Galvanized Steel
- Glass
- Exponential (All Sample Types)

$y = 79.639e^{-0.198x}$
$R^2 = 0.6101$

X-axis: Mass of Dust on Sample (g/m^2)
Y-axis: Efficiency % (with respect to clean surface)

Figure 6-25: Efficiency of contaminated surface as a function of mass of deposited dust

Chapter 7

Cleaning Concepts

Given the scarcity of water in dusty environments where solar thermal power is installed, cleaning of reflective mirror surfaces is aan important issue. As shown in the previous chapter, particle concentrations of only $6g/m^2$ of mirror can cause up to 85% loss in reflectivity, which directly affects overall efficiency of the solar collector module. This chapter presents initial testing of the effectiveness of several cleaning concepts.

Traditional methods for cleaning parabolic trough collectors consist of manual washing using water. Systems of large brushes and water tanks as well as pressure washers on truck-beds are used by a cleaning crews who periodically drive in between rows of collectors to remove dust that has been deposited on the mirror surface, which requires $22L/m^2 \cdot year$ at sites in the southwest United States [18]. The costs of the water, which generally is not recovered, makes mirror cleaning an expensive task, and may be impractical in regions where clean water infrastructure does not exist. However, the loss in panel efficiency if the panel is not cleaned is an even larger cost in terms of overall energy costs. As an example of the order of magnitude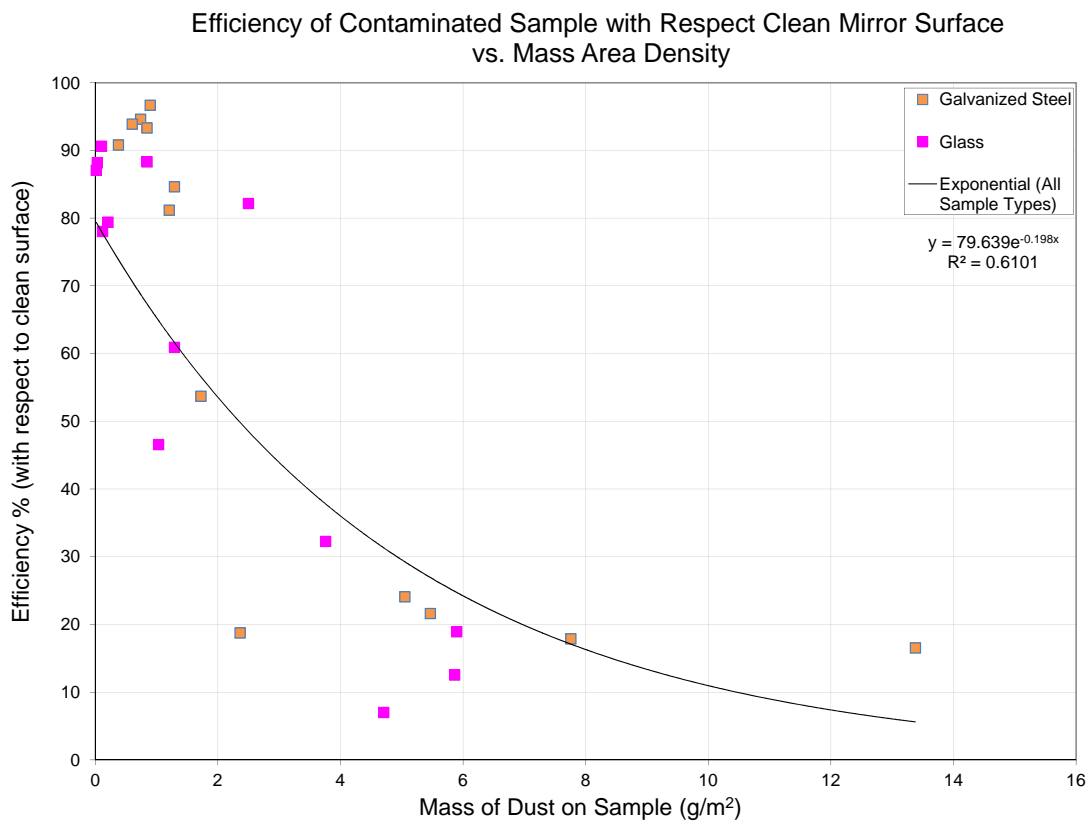 of cleaning costs, equation 7.1 gives a cleaning water cost of $0.011/m^2year$ if one assumes water is generated using desalination at a cost of $0.50/m^3$ of water ([73]).

$$\left[\frac{22L}{m^2year}\right]\left[\frac{0.001m^3}{1L}\right]\left[\frac{\$0.50}{m^3}\right] = \frac{\$0.011}{m^2year} \tag{7.1}$$

In addition to the cost of water labor for a plant on the order of $100,000m^2$ of panels, assuming a cleaning crew of 3 working throughout the year at \$30,000/year per person, and not including the cleaning equipment would result in a total plant cleaning cost of \$91100/year or \$0.91/m^2year (Equation 7.2) [18].

$$\left[\frac{\$0.011}{m^2year}\right]\left[\frac{100,000m^2}{plant}\right] + \left[\frac{3personnel}{plant}\right]\left[\frac{\$30,000}{personnel \cdot year}\right] = \frac{\$91,000}{year} \quad (7.2)$$

Comparing this cost to the cost of electricty generated per square meter, with an assumed cost of \$0.20/kWe, equation 7.3 gives a generated panel value of \$87/m^2year. Overall the cost of manual cleaning with desalinated water is 1% of the the generated electric value. Because dirt deposited on a panel can quickly result in 85% difference in the reflective efficiency, meaning approximately \$74/m^2year difference in the generated electricity, the costs associated with cleaning is necessary, however, other methods for cleaning could be more effective overall. While the estimates here simplify the costs and efficiencies associated with such a system, they provide a first order comparison of cleaning costs and difference in performance for the panel if cleaned effectively.

$$\left[\frac{6kWh}{m^2day}\right]\left[\frac{365day}{year}\right]\left[\frac{0.20efficiencykWh_e}{kWh_{solar}}\right]\left[\frac{\$0.20}{kWh_e}\right] = \frac{\$87}{m^2year} \quad (7.3)$$

In addition to water use limitations, manual cleaning with brushes can load the edges of glass mirror panels causing breakage, resulting loss of efficiency, and expensive repairs. Finally, using brushes and water, which contains sand particles, can often scratch the mirror surface, which is especially risky for mirror film applications and front side reflectors. As shown in Section 5.3, surface erosion can lead to losses in reflectivity in the same manner as a sand storm would.

Alternative cleaning methods could take advantage of mechanical, electrostatic, fluid and vibrational means of removing particles. A summary of potential methods, which is by no means exhaustive, is shown in Table 7.1. These methods are divided into active implementations, which require additional energy to interact with contam-

inants, and passive methods, which require no additional energy. For example, and active mechanical method might use a series of rollers to push particles off of the mirror surface, whereas a passive mechanical method would use the existing turning of the trough over the day, which is required anyway for operation, to dump particles by purely gravitational effect. Risks of mechanical methods are that the forces involved in moving the particles may be high enough to scratch the mirror surface or even break the mirror panel. Given the variety of strategies for cleaning mentioned, and the inherent efficiency loss of an active methods that may add additional parasitic loads to the solar field, passive methods were pursued as the overall cleaning focus.

Electrostatic methods would use ionizing particles or control of surface static charge to reduce the surface attraction of particles. An active method, such as an ionizing air knife, requires both forced air flow and a power source for the ionizing air. Ionizing air knifes are often used in clean room applications where passive methods are not possible. A passive electrostatic method would use grounding of the surface to reduce surface charge, much in the way that electrostatic discharge in controlled in clean room environments. Antistatic materials and coating on the surface of the mirror, would also be a passive method, however such a coating would have to be optically clear. In general, better materials for conductors or electrostatic dissipators are opaque, making their effectiveness as a mirror coating unlikely.

Vibration of the panel structure, either actively, with shaker motors or piezo actuators, or passively by tuning the structure to vibrate with wind loading effects could remove larger particles. As this method depends on inertial forces, the effectiveness would largely depend on the particle size distribution and energy transfer to the particles and is often limited to outer contamination layers and particle larger than 100micron [67].

Fluid methods, which is where the standard water cleaning process would be categorized, use fluid flow to lift particles from the surface. Active methods, would use air, other gases, or viscous gels that are forced over the surface. CO_2 snow cleaning, where fluid flow is coupled with nucleation of small dry ice particles to remove contamination by momentum transfer, are also possible, as is used for telescope op-

Table 7.1: Initial strategies for cleaning based on mechanical, electrostatic, fluid and vibrational methods with active and passive implementations.

Method	Active	Passive
Mechanical	Brushes Rollers	Dumping during trough positioning
Electrostatic	Ionizing air knife	Ionizing bar (antistatic methods) Grounding methods Antistatic materials
Fluid	Air nozzle Viscous/collectible gels	Vortex generators /Turbulators
Vibration	Piezo-timed cleaning Shaker motors	Tuned panel structure

tics [74, 75]. Finally, a passive fluid flow method, where the wind that flows over the panel is used with turbulator tapes or vortex generators to create vortices could be integrated into the current structure. Re-entrainment of particles for glass beads with varying bulk air velocities has been studied [76, 67]. Use of vortex generators for surface cleaning has not been found in the literature and could provide a novel means of minimizing contamination. In related areas such as photovoltaic panels, the need for surface cleaning measures has been suggested in solar power applications for autonomous vehicles in space [77, 78]. Given the initial background science of the given passive methods, the passive fluid method using vortex generator was chosen to be evaluated in detail.

7.1   Vortex Generator Concept

One passive cleaning concept that was investigated is the use of vortex generators to increase turbulent flow over the mirror surface. Typically used to control flow over airplane wings, vortex generators placed on the edges of mirror panels have the potential to increase wind-induced vortices preventing dust from settling on the surface and or by re-entrainment of dust already deposited on the mirror surfaces. Using features such as vortex generators, small holes in the panel edges, or other raised features, minor changes to the panel could reduce the need for water-based

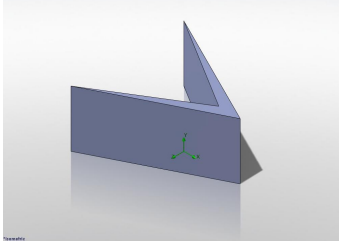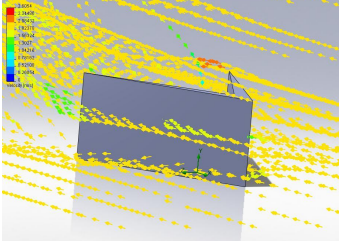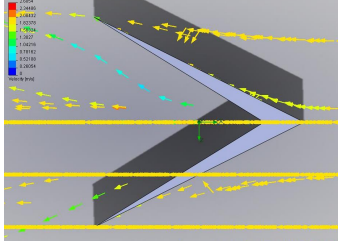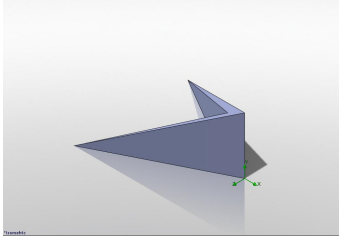cleaning technologies and would require little or no maintenance. [1]
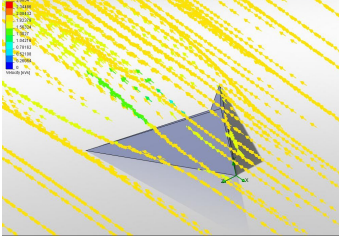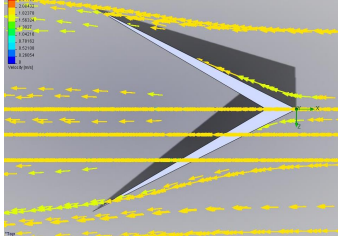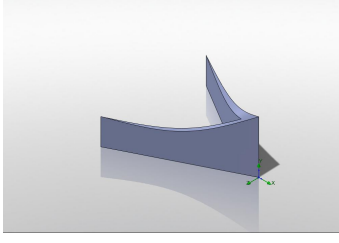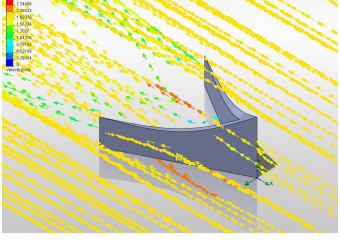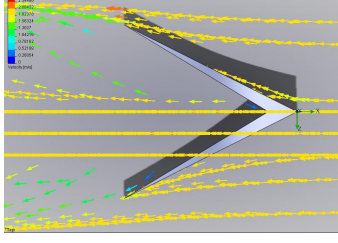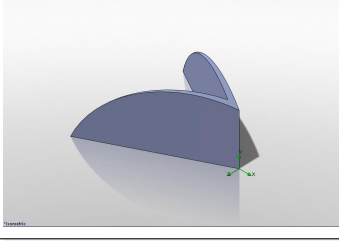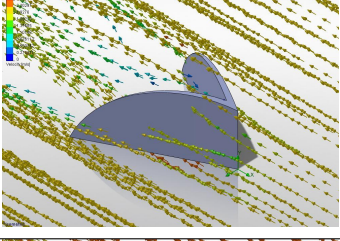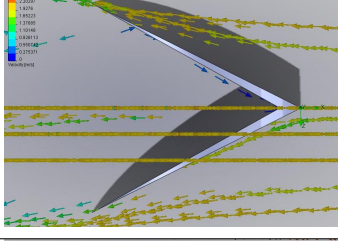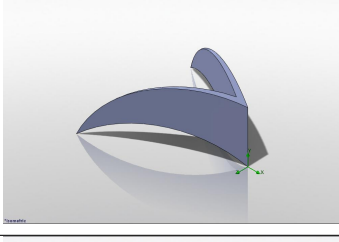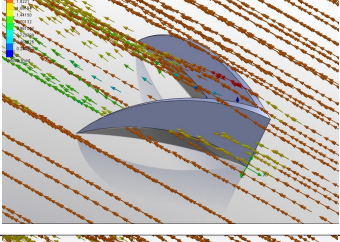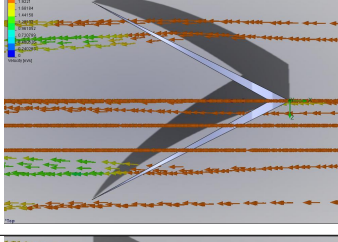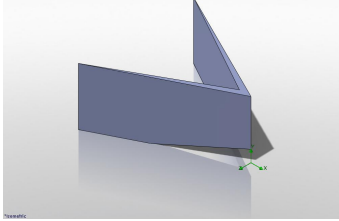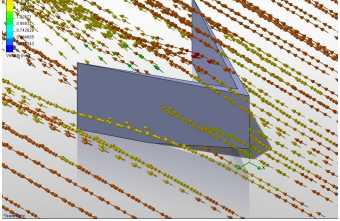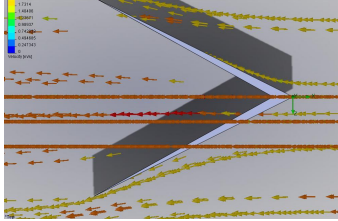
7.1.1 Simulation

Initial studies of the vortex generator concept simulated flow around vortex generator shapes to understand the effects of feature changes. All vortex generators tested had the same major dimensions of height, part length and width shown in Figure 7-1. Six different vortex generator shapes were tested and are referred to in the text according to their shape designation number as shown in Table 7.2. The first design, VG1 is the most simple of the vortex generator shapes with a straight extrusion of a V-shaped two-dimensional sketch. The second version of the vortex generator part VG2 is an extrusion of the V-shape having the same frontal height as VG1 but with the upper surface tapering linearly toward the rear points of the part. VG3 is version of VG1 but with the upper surface being curved concave down as show in the third row of the table. VG4 is a modification of VG1 with a taper to the rear points, as with VG2, but in this case the taper begins normal to the front edge of the part forms a rounded upper edge. The design of VG5 further modifies VG4 by introducing curved gaps between the surface plane and the legs of the V-shaped part on either side. Finally, VG6 is an iteration of VG1 but with an opening at the front of the vortex generator between the surface plane and the frontal edge of the part. Isometric views of flow are shown in the second and third columns of Table 7.2 and larger images of flow around the shapes are shown in Appendix D.

Flow simulations for air at speeds of 5m/s were conducted for a volume 80mm from the bottom of the vortex generator shape, 200mm in depth starting 60mm ahead of the front edge and extending 140mm back, and 160mm in width for the part. Larger simulation volumes greatly increased the simulation processing times. Flow was simulated approaching parallel to the bottom plane of the vortex generator with flow approaching the front edge of the V-shaped extrusion before flowing around the

---

[1]Vortex generator cleaning concept testing is a collaboration with Professor Bahaa Ibraheem Kazem at the University of Baghdad. Results presented here were conducted by the author at MIT. Additional simulations and iterations may be available from his research group.

Table 7.2: Vortex generator shape test matrix showing shape designation, shape, isometric flow and top view of flow.

Vortex Generator	Vortex Generator	Isometric View Flow	Top View Flow
VG1			
VG2			
VG3			
VG4			
VG5			
VG6			
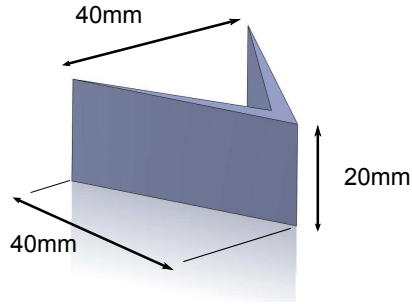
Figure 7-1: Scale of vortex generator shapes

Table 7.3: Vortex generator performance measures and results for six design iterations at 5m/s in air.

Vortex Generator	Maximum Velocity (m/s)	Flow Height (mm)	Flow Width (mm)
VG1	6.15	38	37
VG2	5.90	22	18
VG3	5.78	21	25
VG4	6.08	30	30
VG5	5.95	20	20
VG6	6.13	34	31

legs of the shape. An isometric view of a flow simulation iteration for VG1 is shown in Figure 7-2. This image shows vectors representing flow direction and speed passing around the structure, with upward flow directionality behind the shape. For other versions of the vortex generator, isometric views tended to make relative comparisons difficult to visualize. To visually compare the performance of the six designs, front and side view comparisons of a vector field originating 1mm from the bottom of the surface plate were compared in terms of horizontal spread and height change in a plane located 140mm front edge whose normal is parallel to the original flow direction. Figure 7-3 and Figure 7-4 show front and side views of VG1 with airflow at 5m/s with a 10mm grid spacing overlaid. Figure 7-5 and Figure 7-6 show front and side views of flow around one of the weaker designs in terms of lift height. In addition to the height and spread of the flow around the part, a maximum velocity in the fluid field was identified for each design. Table 7.3 gives a summary of flow height and width in the 140mm offset plane as well as the maximum velocity.

Results from the flow simulation study show maximum velocities greatest for
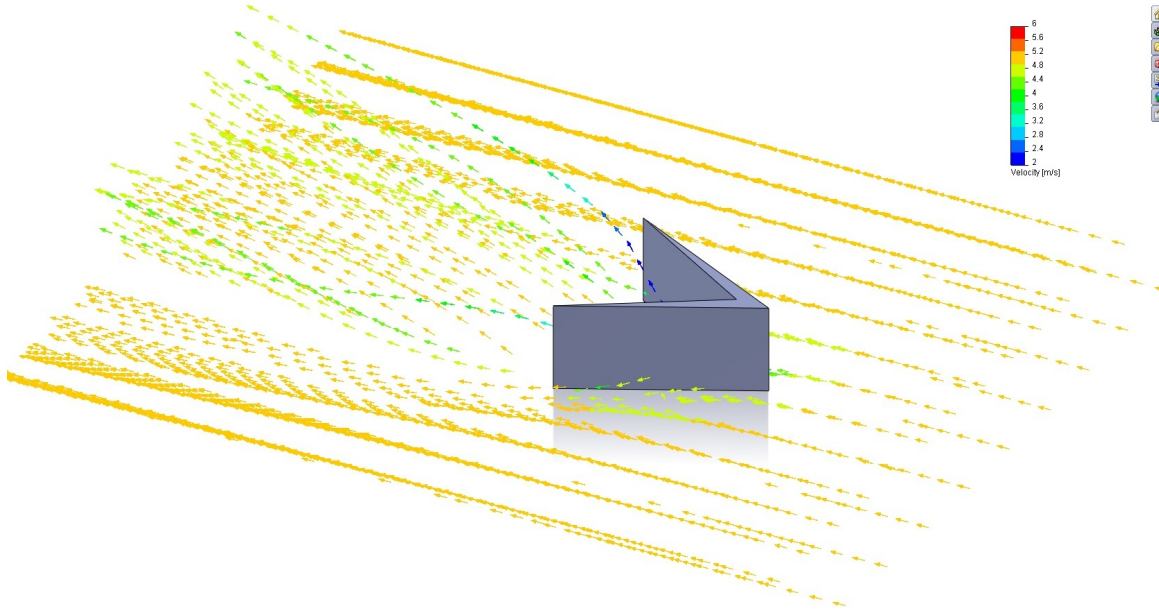
Figure 7-2: Flow pattern of simple extruded vortex generator in air at 5m/s
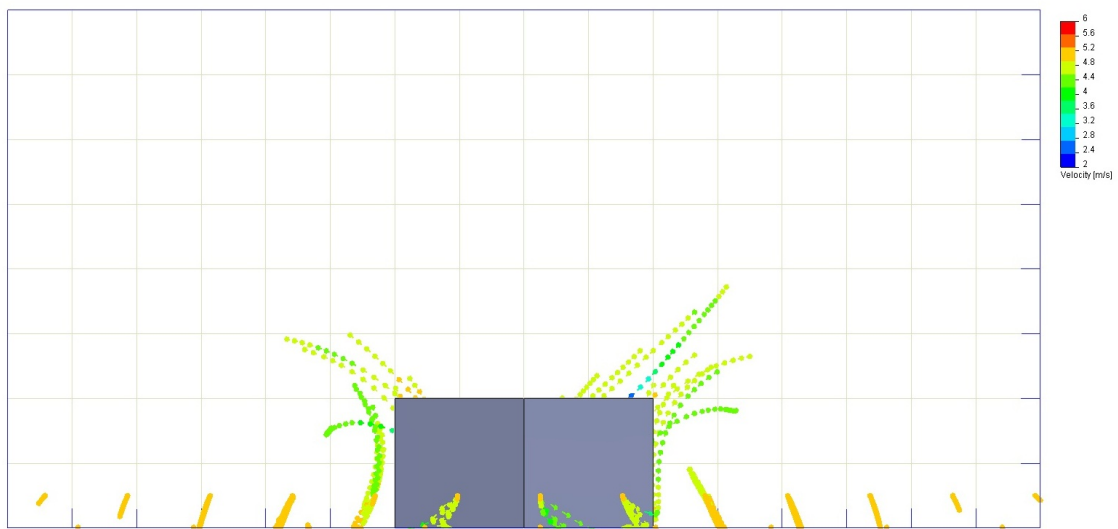
Figure 7-3: Flow pattern of simple extruded vortex generator in air at 5m/s
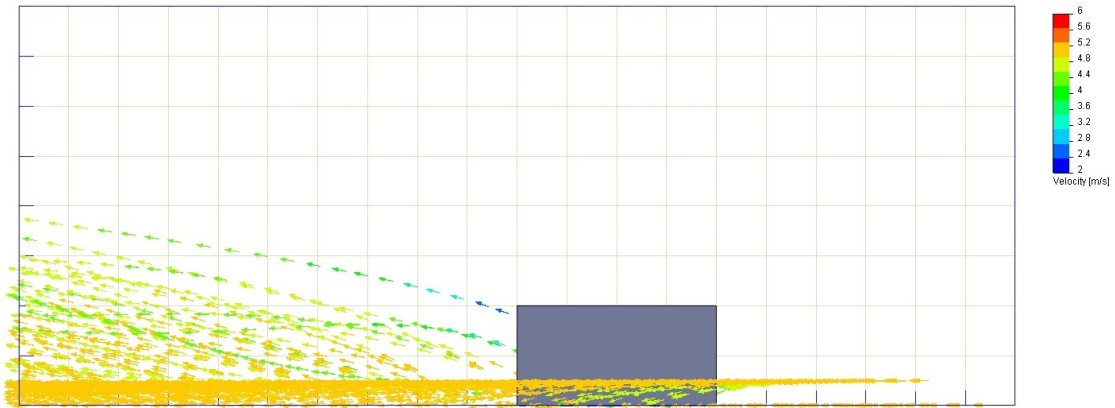
Figure 7-4: Flow pattern of simple extruded vortex generator in air at 5m/s
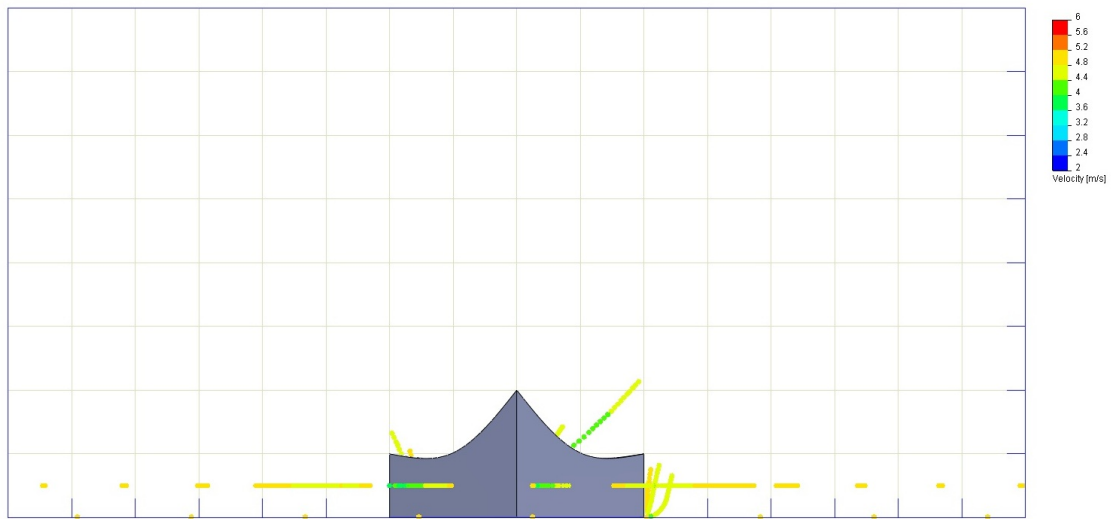
Figure 7-5: Flow pattern of simple extruded vortex generator in air at 5m/s
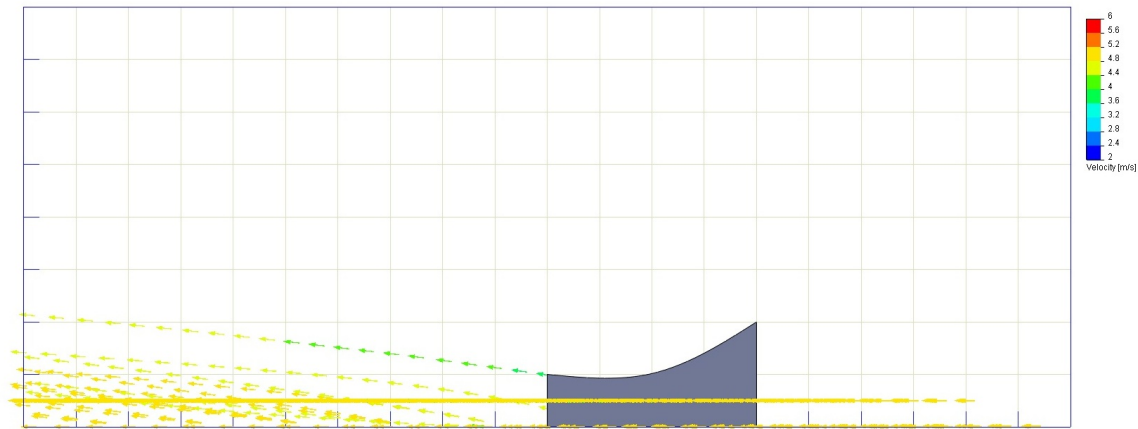
Figure 7-6: Flow pattern of simple extruded vortex generator in air at 5m/s

the VG1 design at 6.15m/s followed by VG6 with 6.13m/s. The design with the smallest maximum velocity measurement was VG3 at 5.78m/s. For the height change comparison of flows initiating 1mm from the surface and measured 140mm behind the vortex generator, VG1 had the maximum lift at 38mm followed by VG6 with 34mm. The heights for VG2, VG3 and VG5 were significantly lower, at 22mm, 21mm and 20mm respectively. As measured from the center-plane horizontally in one direction, the flow width for VG1 was 37mm followed by VG6 with 31mm. The lowest observed width for the flow spread was VG2 with 18mm. The same simulations, when assuming an airflow of 2m/s showed the same relative performance for the shapes, but with smaller magnitudes.

From the initial evaluation of the vortex generator shapes described, the simplest vortex generator shape, VG1 performed better than the other five designs in all three evaluation categories. This design was chosen for further comparison and visualization for vortex generator and cleaning capability. Further studies of performance would attempt to evaluate larger simulation volumes, particularly in the direction of flow, to understand the effective distance of the vortex generator features.

In order to scale features of the simulation for further studies of vortex generator performance, Reynold's number scaling was used to estimate the relative performance for flow in water as well as on for the full size trough. Table 7.4 shows the Reynold's

142

numbers of a vortex generator when scaled for air at the actual scale of the full-sized parabolic trough for three windspeeds, as well as the Reynold's numbers for the simulated windspeeds and dimensions of the modeled part, and finally, that of the vortex generator when tested in a water tunnel for particle imaging velocimetry studies. In some cases, both the windspeed and characteristic length of the vortex generator could be set. Limitations of the pump speed of the water tunnel to 0.1m/s as well as the test section allowed only the variation in vortex generator scale to be set. Details of the water tunnel test setup and results are given in the next section (Section 7.1.2).

The Reynold's numbers given for the design scenarios in the case of the air at actual scale can be varied by assuming a different scaling of the vortex generator depending on the windspeed that is specificed as the target operational speed. However, the target windspeed will depend on assumed parabolic trough installation location as well as the desired performance of the vortex generator. The lower limit of operational windspeed would be set based on the minimum operational windspeeds that occur in a given region with sufficient frequency to maintain a cleaning schedule. The upper limit target cleaning speed would be set based on some percentage of the maximum operational windspeed set for the troughs. In addition to the target windspeed, the dimensions of the vortex generator may be adjusted to scale with simulations. Results of the water tunnel and simulation studies can be scaled to full size according to the Reynold's number ratio mentioned to achieve the same baseline results. In both scaling cases, the dimensions of the resulting vortex generator would still be on the order of centimeters, which is within an acceptable range of dimensions to mount to the trough structure. The final desired Reynold's number and scaling would have to be determined on a larger scale panel to optimized the size and spacing, however the previous test provide an outline for such optimization.

7.1.2   Water Tunnel Testing of Vortex Generators

To visualize the vortex shedding off of the vortex generator concept VG1, described in the previous section, particle imaging velocimetry was used to capture flow patterns

Table 7.4: Reynold's number of vortex generator features in air for low, medium, and high windspeeds, as well as for fluid flow simulation parameters and water tunnel parameters.

	units	air actual scale (low)	air actual scale (med)	air actual scale (high)	air simulation	air simulation	water tunnel
density (rho)	kg/m^3	1.18	1.18	1.18	1.18	1.18	997
velocity	m/s	3	6	10	2	5	0.1
characteristic dimension (fin length)	m	0.067	0.04	0.02	0.04	0.04	0.04
mu	Pa*s	1.80E-05	1.80E-05	1.80E-05	1.80E-05	1.80E-05	8.94E-04
mu/rho		1.5254E-05	1.5254E-05	1.5254E-05	1.5254E-05	1.525E-05	8.97E-07
Reynolds Number		1.32E+04	1.57E+04	1.31E+04	5.24E+03	1.31E+04	4.46E+03
Reynolds number ratio wrt air at 10m/s		1.01	1.20	1.00	0.40	1.00	0.34

behind an extrusion with 30 degree, 45 degree, and 60 degree V-shapes. To capture the dynamic effects of a vortex generator in a fluid field, a water tunnel with 200mm x 200mm cross-sectional area, 10cm/sec nominal flow rate and seeded with 50micron glass beads was used to image the flow. A green laser was used to image a horizontal flow plane, creating a two dimensional image of particle motion, which was captured using a rear mounted camera with 40fps frame rate. An image of the water tunnel with PIV testing in progress is shown in Figure 7-7.[2]

Models of the vortex generator shapes were produced using stereolithographed parts of DSM Somos 18420 resin with a glass bean finish to achieve a smooth planar part, while maintaining a sharp front edge [79]. Parts were extruded to 200mm length to ensure that the imaging plane would be far from edge effects. The three resulting extruded vortex generator parts are shown in Figure 7-8.

Results of the flow visualization were captured as image sequences of particle position in the laser imaging plane. Figure 7-9 shows a raw image of particle flow for each of the three angled vortex generators. Particle image velocimetry software PIVView was used to process sets of sequential images. By comparing particle position in the images along with frame rate and vortex generator dimensions in the plane, vector fields were created for each part configuration. Images used for flow analysis have the vortex generator positioned largely out of the image frame in the upper right corner

---

[2]Design and implementation of the water tunnel PIV test setup by John W. Roberts of the MIT Robot Locomotion Group. Many thanks for access to this test setup.
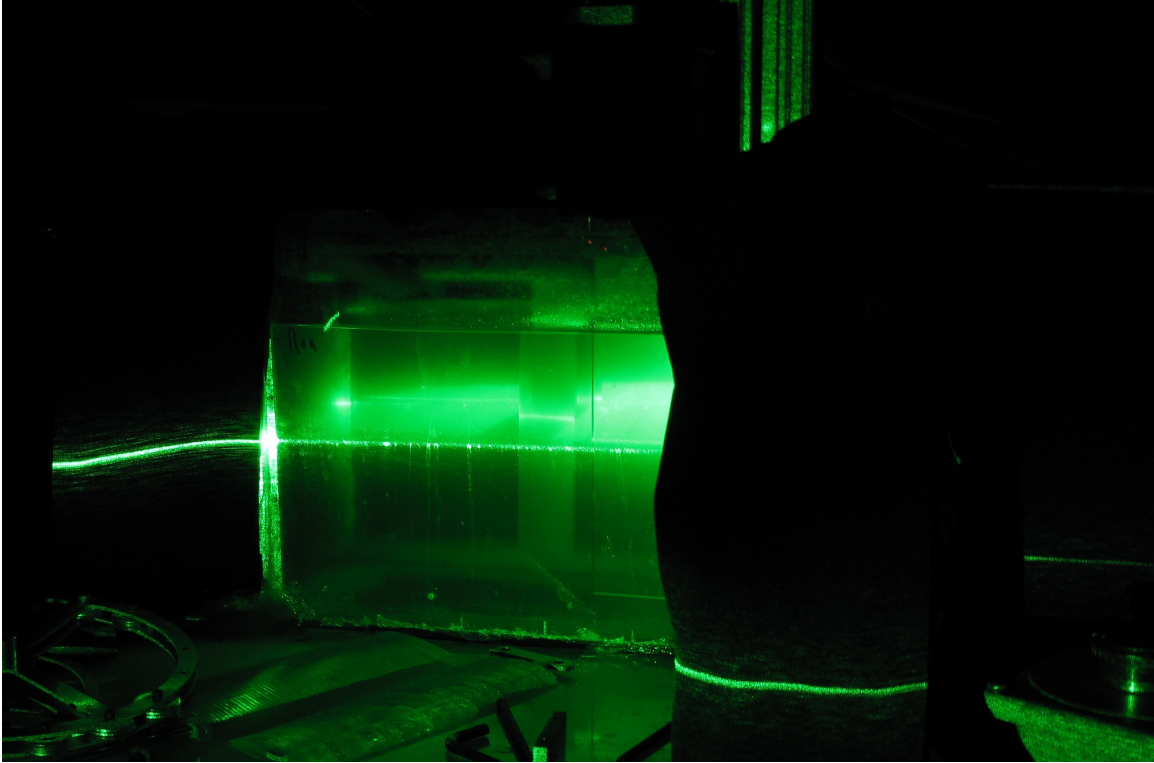
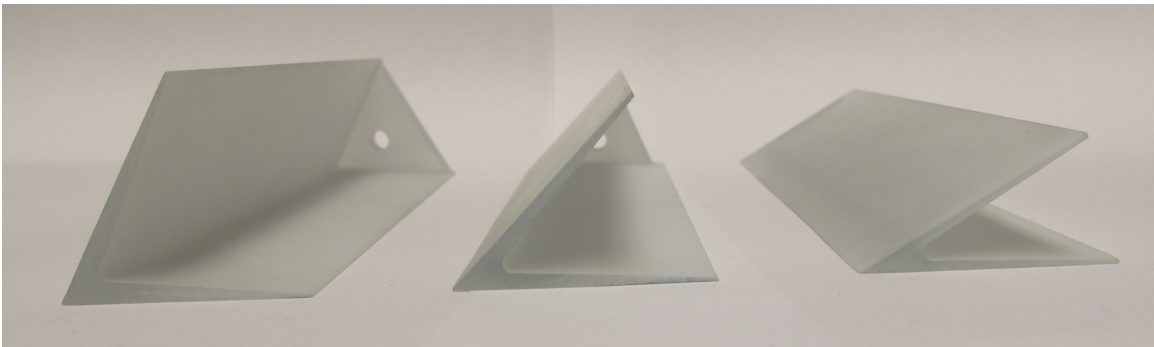Figure 7-7: PIV testing of vortex extruded vortex generator shapes in a water tunnel.

Figure 7-8: Extruded vortex generator shapes for evaluating angular effects.
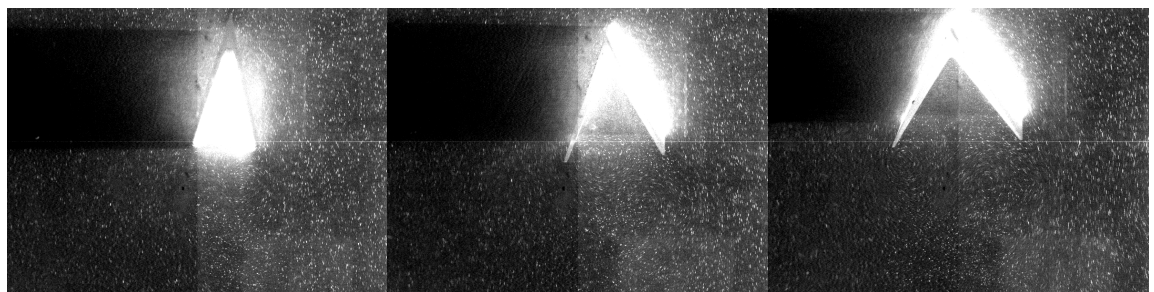
Figure 7-9: Vortex generator cross-sections with 50micron particles in water tunnel.

to allow for maximum trailing flow length in the image. Shadowing of the part in the images is responsible for discrepancies in vector calculations in the upper left section of the images. All images were post processed to remove a single horizontal pixel line defect in the image, which interfered with vector flow analysis.

Results of the 30 degree vortex generator are shown in Figure 7-10, with the tail region of the vortex generator marked in the upper right. The color velocity map, with flow starting at the upper edge of the plot and flowing down, shows the affected region behind the vortex generator approximately 80mm, twice the tail width and more than twice the vortex generator length at 90mm. Velocity of the unaffected flow on the left hand side of the plot show approximate 10cm/s flow rate, whereas behinds the vortex generator, flow rates range from 0m/s to 0.11m/s. Figure 7-11 shows a color vector plot of the same 30 degree data, but which allows for clearer viewing of the vector directionality. In this plot, the increased turbulence of the flow behind the vortex generator is visible when compared to vector fields in the free flow region on the left. The same shadowing error vectors in the upper left (20mm x 60mm) should be ignored, as they are a result of image processing and were not visible in actual particle flow.

PIV analysis was conducted with the same testing parameters for a 45 degree vortex generator shape. Figure 7-12 shows the resulting vector field and velocity map for the 45 degree shape, with the tail region labeled in magenta in the upper right corner of the plot. In the case of the 45 degree vortex generator, the affected zone for the same nominal 0.1m/s flow rate shows a much larger affected area extending approximately 90mm in width at the extent of the 90mm travel length. Velocity behind the vortex generator ranges from 0m/s to 0.11m/s or greater. In the 45 degree case, Figure 7-13 shows a larger zone of turbulent flow that for the 30 degree shape, more eddies are visible and a wider overall affected zone is visible compared to that of the 30 degree shape in Figure 7-11.

The 60 degree vortex generator shape, with velocity field and vector plot shown in Figure 7-14 shows a similarly sized flow field as for the 45 degree vortex generator. In this case fewer but larger vortices appear in the image, and the overage velocity in

146
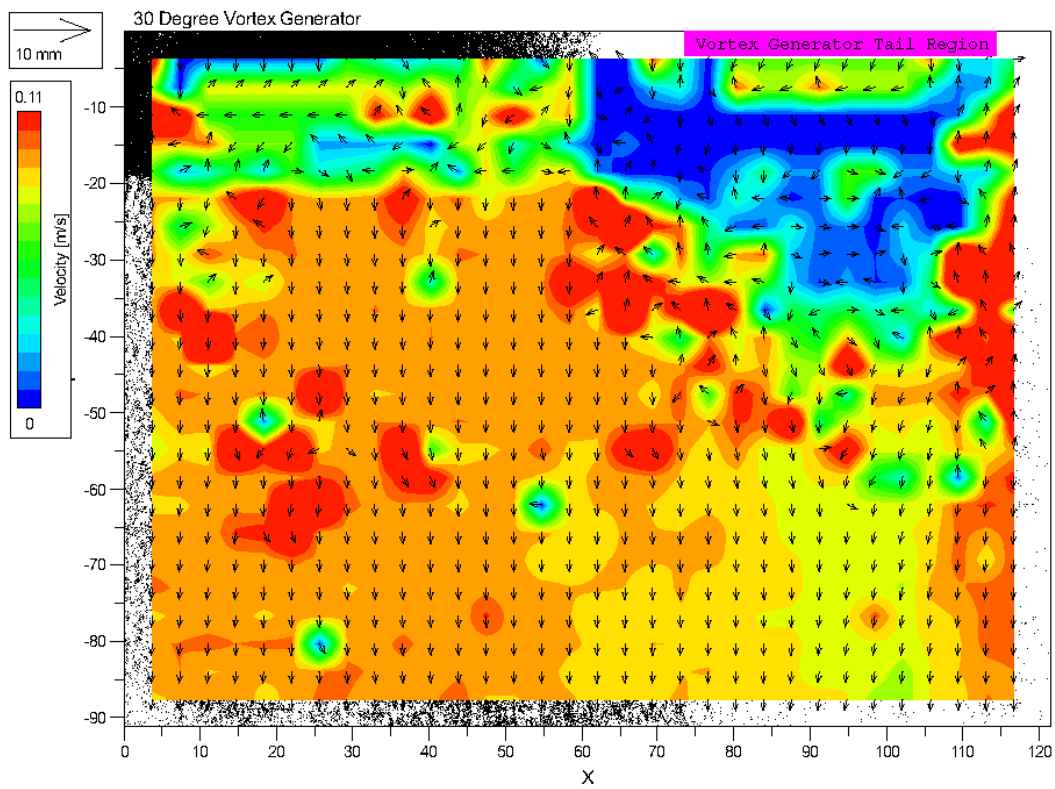
Figure 7-10: Vector field and velocity map of 30 degree vortex generator.
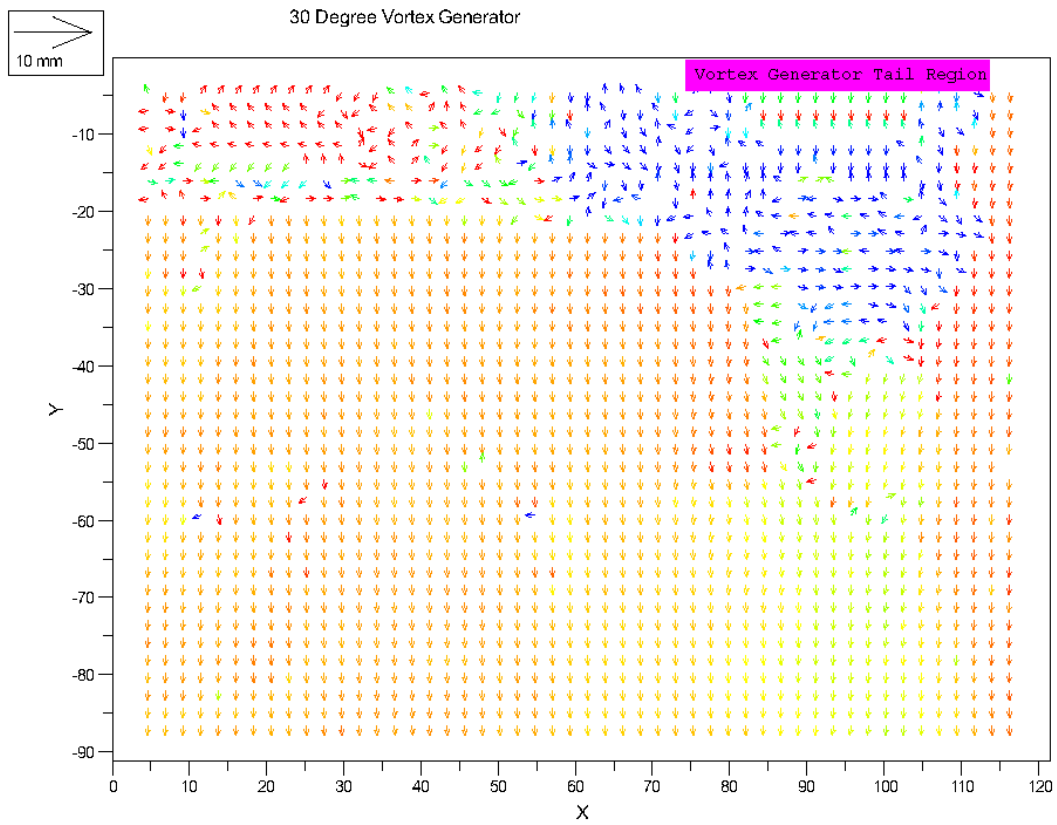
Figure 7-11: Vector field of 30 degree vortex generator cross-sections with 50micron particles in water tunnel.
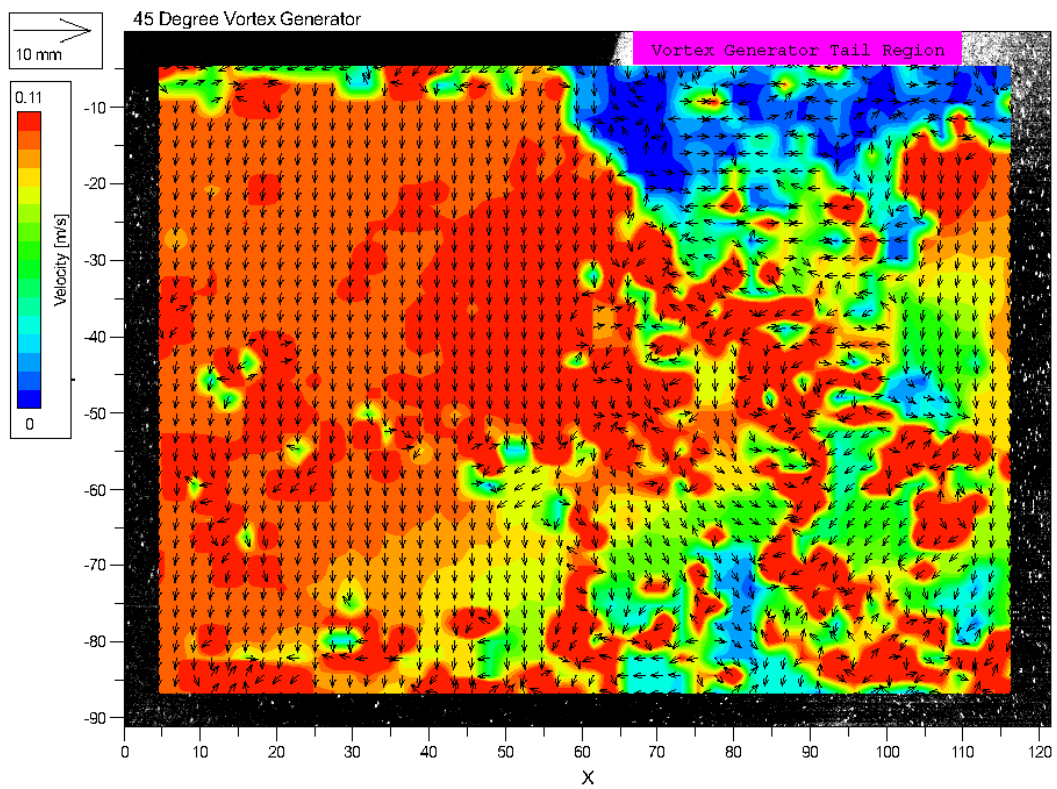
Figure 7-12: Vector field and velocity map for 45 degree vortex generator.
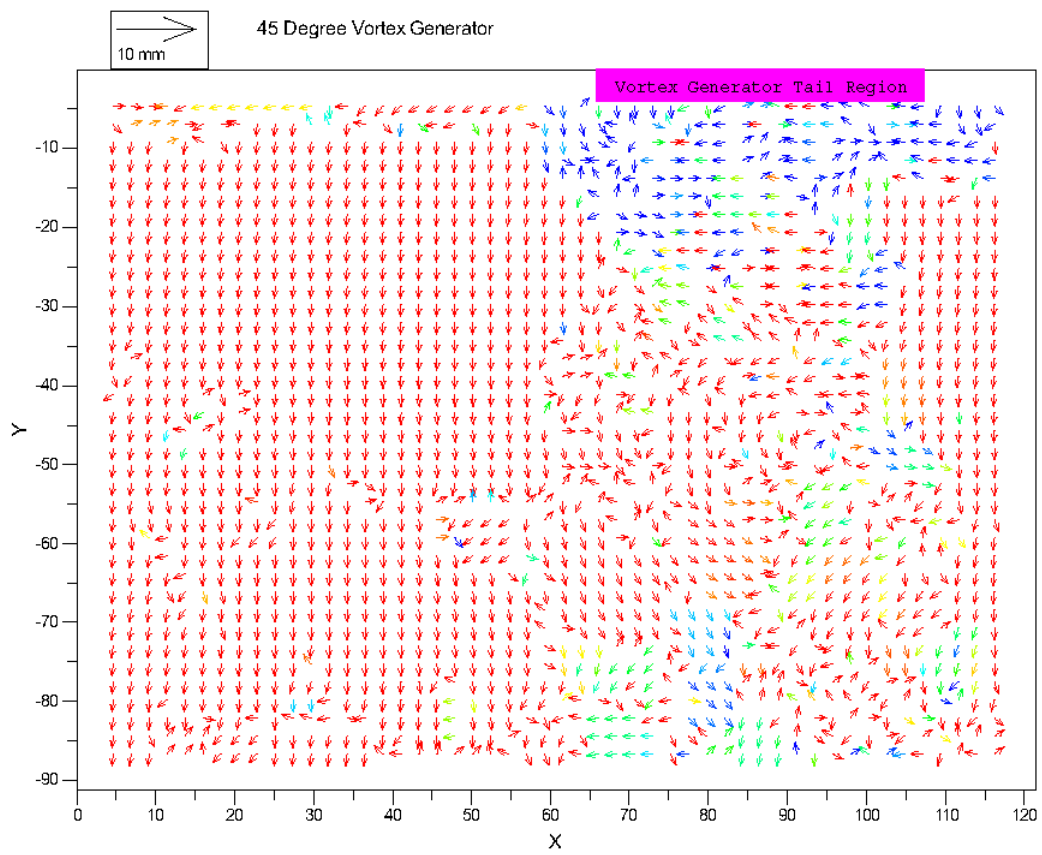
Figure 7-13: Colored vector field plot for 45 degree vortex generator.
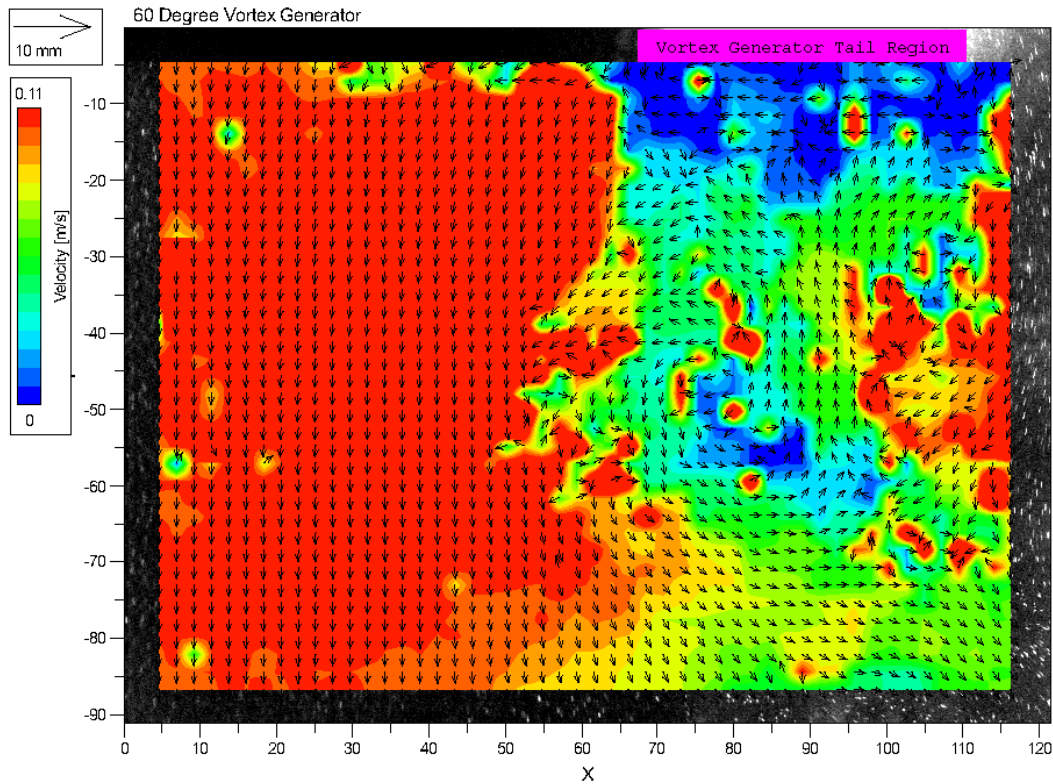
Figure 7-14: Vector field and velocity map for 60 degree vortex generator.

the turbulent region appears more uniform in the 0.5m/s range. Figure 7-15 showing the colored vector field for the 60 degree part shows a similarly 70mm-80mm wide turbulent region behind the vortex generator.

Results from the vortex generator angle variation and PIV imaging show larger turbulent regions for 45 degree and 60 degree vortex generator shapes than for a 30 degree shape. Between the 45 degree and 60 degree versions of the part, the 45 degree part shows a higher average velocity behind the tail of the vortex generator. To make definite decision regarding performance between these two shapes, a larger test length would be important. Imaging in the vertical plane of the vortex generator to visualize lift would also informative. Scaling of the vortex generator for differing average flow velocities for the installation site could also refine the design.

151
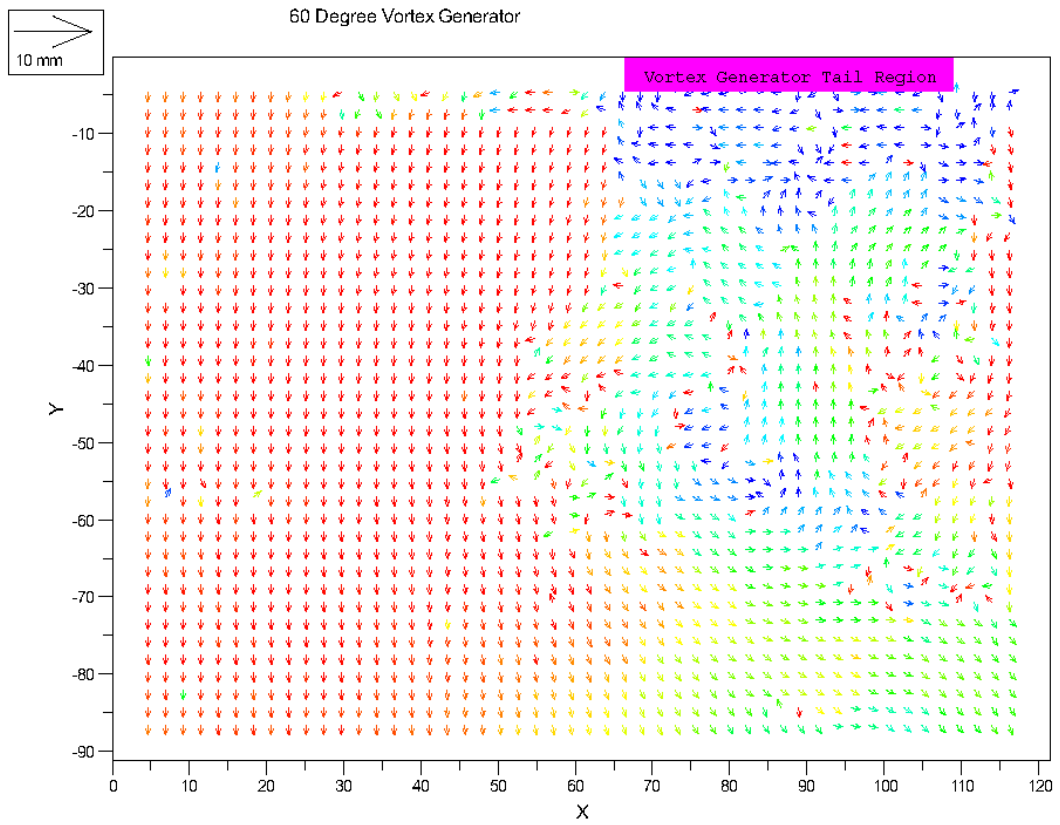
Figure 7-15: Colored vector field plot for 60 degree vortex generator.

7.1.3 Reflectance Measurement of Vortex Generator Cleaning on a Mirror Film Surface

Ultimately the vortex generator cleaning concept could increase the efficiency of a parabolic trough collector panel more effectively than existing flow alone. To test the concept effectiveness, a bench-top test of reflectance was performed on a 150mm x 180mm galvanized steel sheet with mirror film applied to the front-side surface. A 40mm x 40mm x 20mm vortex generator VG1 shape, as detailed in Figure 7-1 was stereolithographed and attached to the center-line of the sample panel as shown in Figure 7-16 with reflectance testing locations shown circled in red. Twelve sample locations were tested round the vortex generator shape, with Location and Location 2 in left and right front corners of the test part, where it was assumed that little effect would be seen. A test row 20mm behind the vortex generator in five locations centered about the flow axis and space approximately 30mm apart were used for Location 3 through Location 7 from left to right. Another 30mm behind the first test row, Locations 8-12 were labeled from left to right on the sample. Initial measurements of the clean surface reflectance were taken with a Stellarnet Blue Wave Spectrometer for wavelengths of 350-1100nm (Section 6.4). To produce a uniform layer of contamination over the surface, the mirror panel with attached vortex generator was placed in a dust chamber for 23minutes with Arizona Medium Test Dust, as previously described in Section 6.2.1. Measurement of reflectance over the contaminated surface were taken in several locations. Figure 7-17 shows the mirror panel with uniform deposition across the surface.

To create a uniform sheet of air flowing over the panel an Exair air knife was placed 30mm in front of the vortex generator edge with the flow plane offset approximately 5mm from the surface. A constant pressure air supply of 290kPa (28psi) was used to flow air at a measured speed of 5.9m/s at the exit of the device. Measurements of reflectance after airflow a were taken over the Locations 1-12. Figure 7-18 shows the resulting mirror surface after a 60second cleaning, after which little visible change was observed.
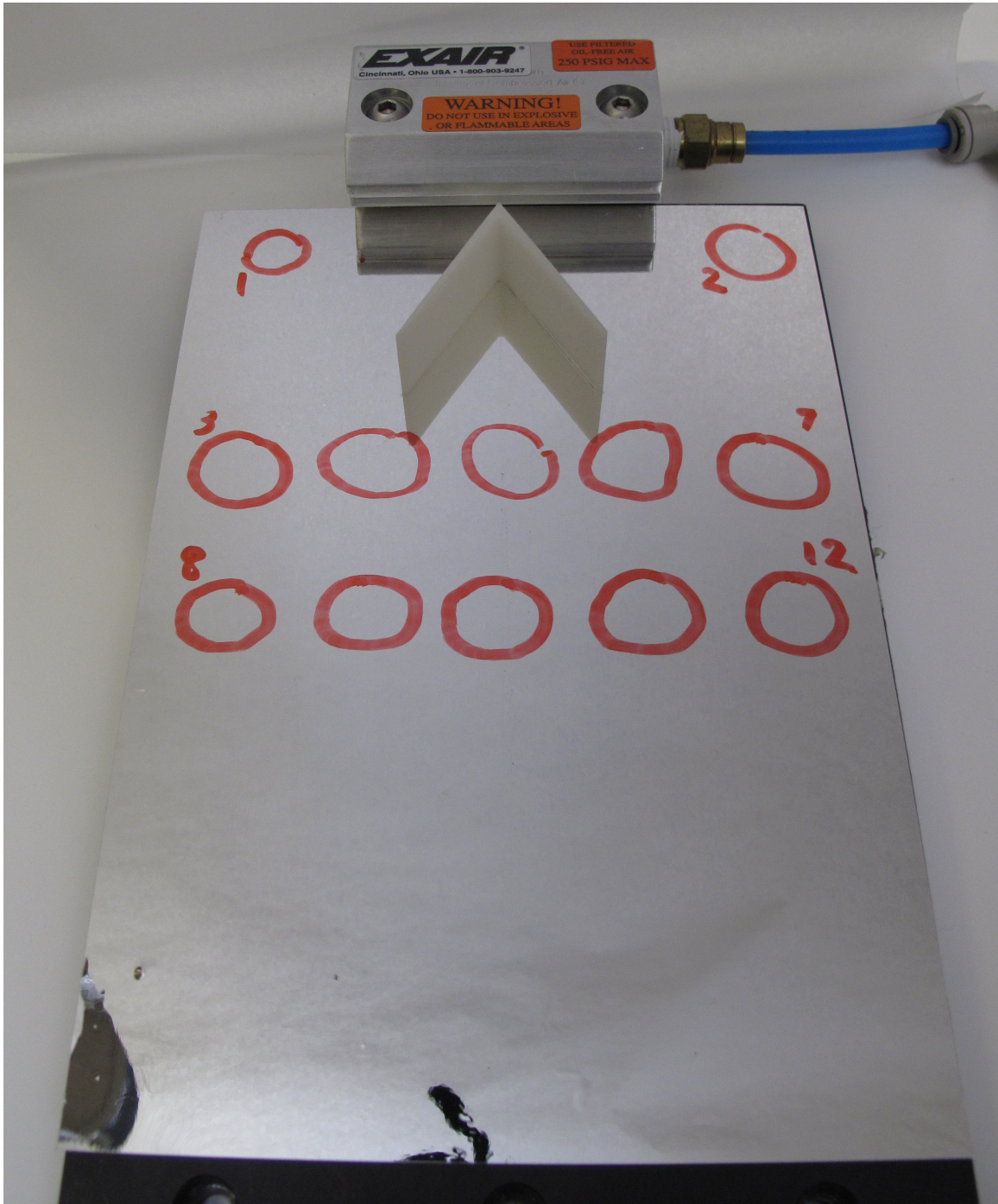
Figure 7-16: Vortex generator on mirror film surface with testing locations circled

Figure 7-17: Vortex generator on mirror film surface after 23 minute contamination in dust chamber.

Figure 7-18: Vortex generator on mirror film surface after 5.9m/s airflow over panel.

Following the vortex generator tests the same surface was deposited with dust for a second 23 minutes and the vortex generator was removed from the surface. Figure 7-19 shows the deposited surface prior to cleaning. The surface cleaning with the same flow rate and flow offset was repeated on the untreated surface. The resulting cleaned surface without a vortex generator is shown in Figure 7-20.

Results of the reflectance measurements over the sample surface are shown in Figure 7-21. In this plot, the total reflectance of the clean surface over all locations averages 2.5×10^7counts when looking at the raw intensity data. The contaminated surface, both before vortex generator cleaning and for simple airflow over the surface were approximately 0.5×10^6counts. For the surface after cleaning using a simple airstream over the surface, total reflectance averages 3.9×10^6counts and for the surface cleaned air flow around the vortex generator shape total reflectance averages 7.4×10^6counts. In this plot additional reflectance measurements shown as Location 13, which was at the very end center of the panel. This additional measurement was taken for the contaminated surfaces when it was found that placement of the reflectance probe in Location 3 to Location 12 could potentially disturb the deposited dust layer of adjacent test locations.

Figure 7-22 shows the efficiency of the cleaned surfaces according to location as compared to the total reflectance of the initial uncontaminated surface. In this plot, optical efficiency of the panel after airflow over the surface with no vortex generator present varied from 1.8% to 23% with an average efficiency of 14.4%. For the panel performance after cleaning with the vortex generator located on the surface, the efficiency ranged from 15.0% to 41.1% with an average of 29.3% efficiency. Where measurements were made for the contaminated surfaces, optical efficiency was measured at 1.8%-2.5%.

This difference in cleaning performance suggests that vortex generators improve surface cleanliness of mirror film panels, however the ability to measure this effect over large areas far from the vortex generator feature and for longer durations would have to be tested on a full-scale trough module.

Figure 7-19: Mirror film surface after 23 minute contamination in dust chamber with previous vortex generator location shown.

Figure 7-20: Mirror film surface after 5.9m/s airflow over panel with vortex generator absent.
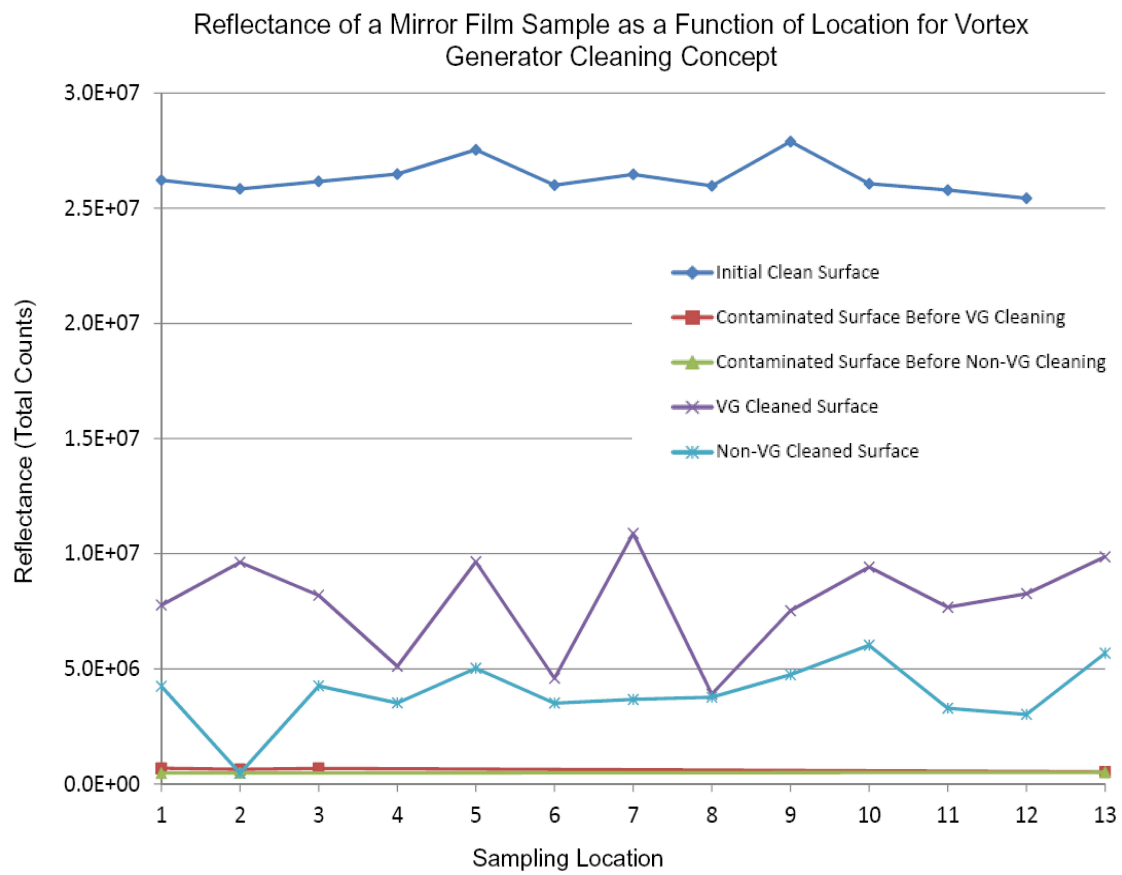
Figure 7-21: Reflectance of mirror film for the initial surface, contaminated surface, vortex generator cleaned surface, and non-VG cleaned surface.

Figure 7-22: Efficiency of mirror film surface for vortex generator cleaning compared to non-VG cleaned surface.

7.2 Summary

Given the simulation, visualization and small scale panel test of vortex generator cleaning performance, this passive cleaning method could result in cleaning savings over the lifetime of a solar plant. To test vortex generator cleaning further, a much larger test length would be required and ideally imaging in the vertical plane of the part to capture lift and re-entrainment of particles would also be implemented. Most likely, testing of this size would have to integrate PIV imaging in a larger wind tunnel, which would be difficult given the health risks of releasing small particles in the confined space. Ideally, direct measurements of mirror panel cleanliness at an existing solar installation wuold be pursued. This could give more specific information on cleaning performance and ease of installation for existing parabolic trough designs. In addition, studies of vortex generator positioning in the curved trough surface and for crosswinds would be informative for design optimization.

Additional methods mentioned at the beginning of this section should not be ruled out as possible cleaning methods should active concepts be considered as a cost effective option. The uncertain cost feasibility for methods such as CO_2 snow cleaning for instance make this method difficult to compare as an active cleaning concept, despite its potential for increase cleaning effectiveness.

Chapter 8

Conclusion & Recommendations

Parabolic solar troughs are a very mature technology, but in the area of alternative energy research, every percent that can be gained in efficiency or cost of ownership is critical. Given the scope of the fundamental issues and components involved in industrial sized solar power plants this thesis was able to demonstrate improvements in the design of a parabolic trough modules by studying a monolithic molded trough design, evaluating efficiency of mirror film surface backing matierials and film abrasion effects, quantifying the resulting effects of contamination on film reflector surface efficiency, and finally design and evaluation of vortex generators as a passive cleaning concept.

The details of this investigation involved evaluating the overall structural concept of the collector to reduce complexity while maintaining structural stability under wind loading conditions. In the process of evaluating the feasibility of one such concept, a monolithic reflector panel with a mirror film front surface, details related to the mirror surface efficiency were investigated. At the panel-structure to mirror interface, surface roughness of the underlying structural backing was looked at to understand performance effects on the mirror film surface that would make one backing material potentially more suitable than another. In this case it was found that three materials tested: gel-coated fiberglass, rolled aluminum, and rolled steel were all similarly effective when compared to a more expensive mirrored aluminum backing material. When looking at the integration of the larger structural changes with the factors that

affect surface reflectivity of parabolic mirrors, it became apparent that contamination of the surfaces and cleaning were major factors in reduced module effectiveness. Given that the conceptual development of the structure was ongoing, research into contamination factors and potential cleaning solutions were considered in such a way that panel cleaning solutions could be integrated into the trough module design from the start. A vortex generator cleaning concept, which uses V-shaped extruded shapes to create vortices over a panel in the presence of wind, was modeled and then tested as a passive cleaning solution.

Aspects of this research have the potential for use in other areas of energy research. In particular, vortex generator cleaning methods could just as easily be implemented on existing solar troughs systems as well as photovoltaic panels for solar installations. Evaluation of mirror film durability and application to panel surfaces could allow mirror film panels to replace broken glass sections of existing structures. Understanding the surface roughness requirements of mirror film backing could enable film replacement on scratched or damaged panels by simple removing the old film and replacing it with a new layer, or possibly just laying a new sheet of film on top of the damaged layer. Monolithic panel mirrors for solar tower concepts, where torsional stiffness requirements on the panels are not as strict, may help to reduce field costs. It is the hope of the author that this research helps to take a small step toward higher efficiency solar power plant installations, making solar a more viable source of energy in the future.

Next steps for evaluation of the vortex generator cleaning concept would be to implement the design on a full scale module at an existing solar installation. With a full-scale module in operation, the cleaning efficiency on the full curved collector, manufacturing and installation costs, and vortex generator spacing could be evaluated with typical wind conditions. Given these inputs and a cost-benefit analysis similar to that given in the flowchart of Figure 8-1, a plant operator could decide whether the benefit of installing vortex generators on all panels is worthwhile.

Figure 8-1: Flowchart of vortex generator cleaning concept cost-benefit analysis.
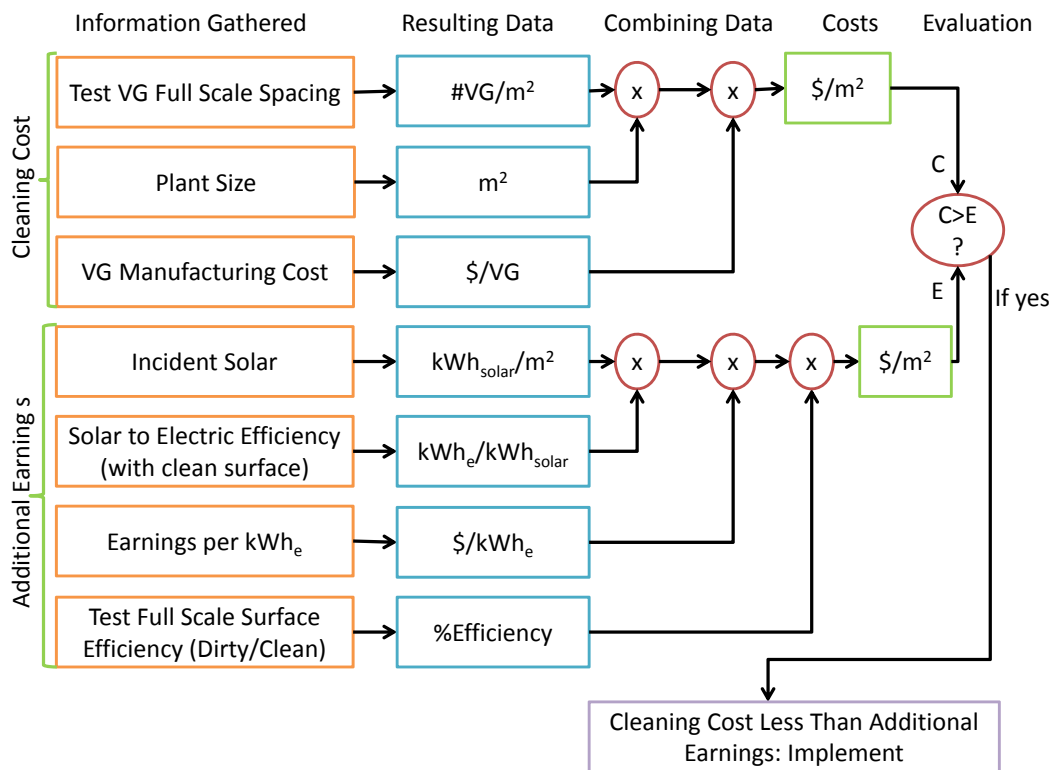
Appendix A

Fiberglass Trough Fabrication

A.1   Trough Detail Drawing

Figure A-1 shows the drawing of the composite 1/10-scale solar trough panel used for wind loading measurements and which was used as a reference for construction of the mold.

A.2   Mold Construction

To produce a vacuum formed composite parabolic trough, a mold was produced to provide adequate stiffness and surface accuracy. Detailed construction of the mold and welding the frame was performed by Keith Durand and Josh Dittrich to comply with the composite part specifications in Figure A-1. Figure A-2 shows the steel structure that was welded both as a structural support for the mold, but with end details that would serve as guides for application of final surface filler material. Figure A-3 shows the sheet metal being welded onto the frame to ensure that it maintains appropriate dimensional tolerancing. Figure A-4 shows the front surface of the mold being polished and prepared for the filler application. After the surface is smoothed and prepped, Figure A-5 shows a mold filer beign sread over the front surface using the ends of the frame as a thickness gauge. The final mold surface was wet sanded to a gloss finish and treated with mold release before being prepped for the layup

The engineering drawing contains the following text:

1. Parabolic Shape, inner surface most critical.
   Equation for profile of this inner surface
   $y=h(x^2/a^2)$
   where origin is lowest point of the parabola and
   $h= 0.156 \pm 0.005$
   $a=0.250 \pm 0.003$

2. Focal line of inner parabolic surface

3. Aluminized mylar will be adhered to
   the inner surface

(0.65)

0.05 ±0.01

0.250 ±0.003
see note 1

0.004 0 +0.002

(0.100)

75°

0.156
see note 1

R0.025

0.54

1 ±0.02

0.17

A

0.003 A

			UNLESS OTHERWISE SPECIFIED:		NAME	DATE	
			DIMENSIONS ARE IN METERS	DRAWN	SF	01/14/09	
			TOLERANCES: FRACTIONAL:	CHECKED			TITLE:
			ANGULAR: ±5 degrees				Extruded Parabola Shaped
			TWO PLACE DECIMAL ±0.01m THREE PLACE DECIMAL ±0.005m	ENG APPR.			Composite Collector
				MFG APPR.			1/10 scale model
			INTERPRET GEOMETRIC TOLERANCING PER:	Q.A.			
PROPRIETARY AND CONFIDENTIAL				COMMENTS:			
THE INFORMATION CONTAINED IN THIS DRAWING IS THE SOLE PROPERTY OF MIT. ANY REPRODUCTION IN PART OR AS A WHOLE WITHOUT THE WRITTEN PERMISSION OF MIT IS PROHIBITED.			MATERIAL Fiberglass Composite TBD	Stacy Figueredo stacyfig@mit.edu Office # 617.253.2052 MIT Precision Engineering Research Group			SIZE **A** DWG. NO. 1 REV **A**
	NEXT ASSY	USED ON	FINISH very smooth, gel coat				
	APPLICATION		DO NOT SCALE DRAWING				SCALE: 1:10 WEIGHT: SHEET 1 OF 1

Figure A-1: Drawing of 1/10th scale parabolic trough for fiberglass prototype construction

Figure A-2: Framing of Parabolic Trough Mold

process (Figure A-6).

A.3   Vacuum Layup Process

This section shows additional images of the vacuum layup process for creating the monolithic composite trough used in the wind tunnel experiments.

Figure A-3: Welding skin onto steel frame

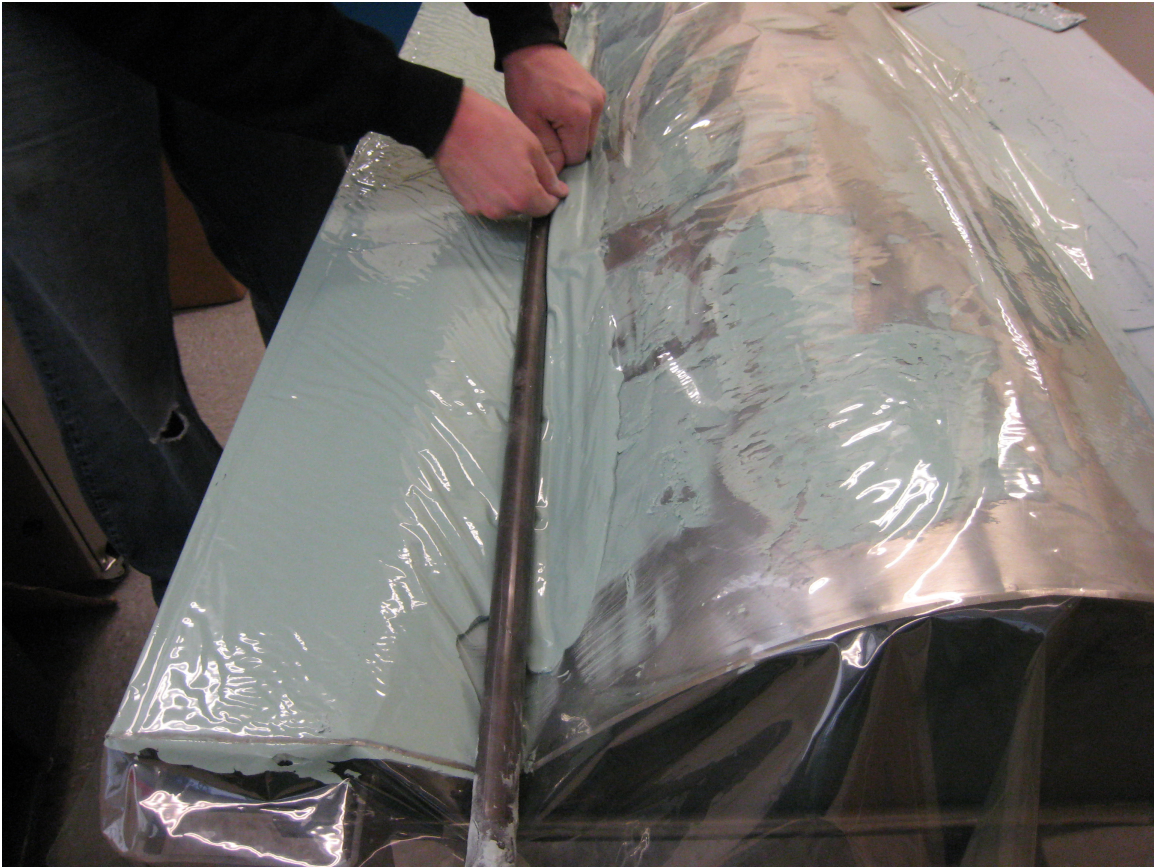Figure A-4: Polishing mold surface before filler application

Figure A-5: Mold filler applied to create final surface using ends of frame as a thickness gauge.

Figure A-6: Final mold surface after filler smoothing.

Figure A-7: Layup of materials on the parabolic mold

Figure A-8: Vacuum layup process with resin flowing into materials
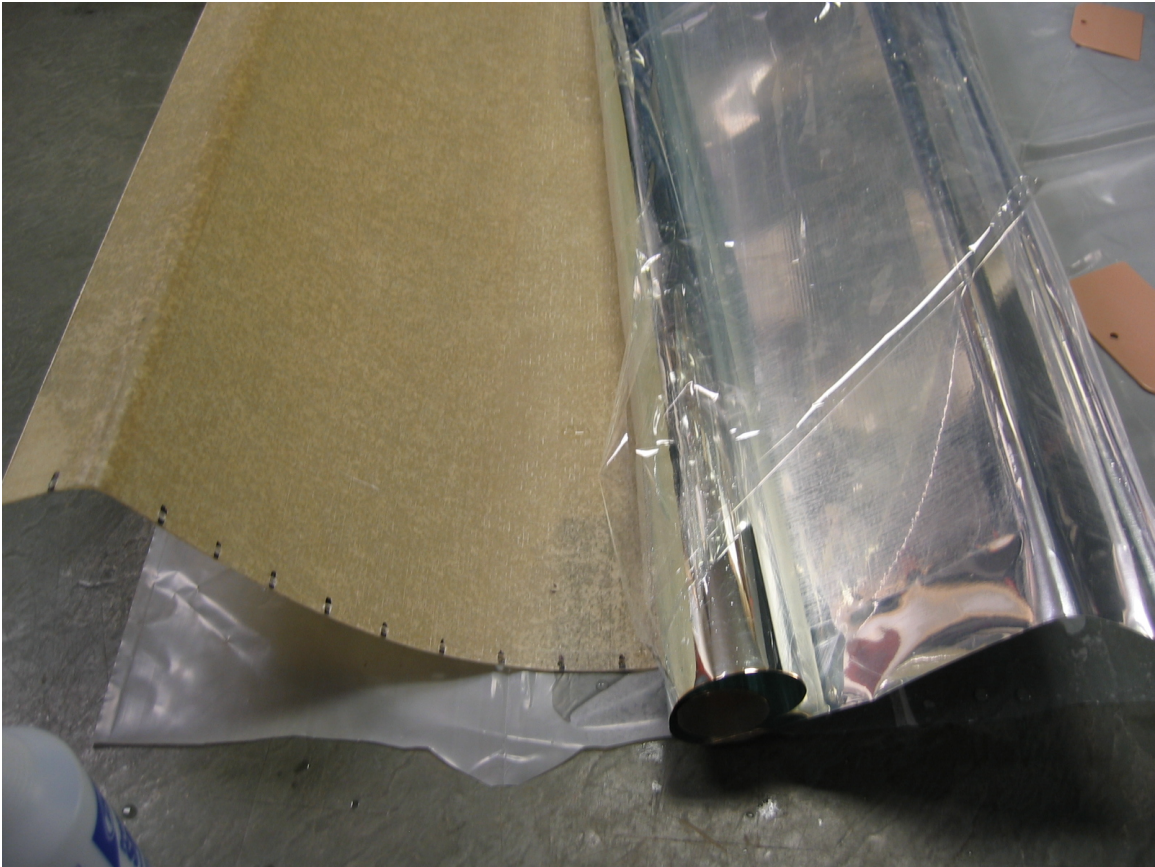
Figure A-9: Final composite part with mirror film being applied

Appendix B

Mirror Film Application Details

Listed in this section are details on the process used to apply an adhesive-backed mirror film with a removable front surface protective layer. In the experiments mentioned in the thesis, a 0.1mm thickness film from Reflectech was used to maintain consistency in reflectivity and efficiency measurements.

B.1   Application Procedure

Using the a fiberglass monolithic trough structure with a gelcoated inner surface, where mounting holes have already been drilled into the part, deionized water was used to thoroughly remove any residual particles from both sides of the part, and in particular the curved inner mounting surface (Figure B.1). To initiate the film application, the clean fiberglass inner surface was spray with a fine water mist (Figure B.1). The protective layer on the adhesive side of the mirror film was peeled back by a few centimeters and also sprayed with deionized water. The film was aligned with the long edge of the parapolic trough and a plastic spreader tool was used to apply pressure to the film where the adhesive was exposed on the fiberglass part (Figure B.1). This effectively pushes the water out from between the surfaces, allowing the adhesive on the back of the film to contact the fiberglass, while limited the amount of air that is trapped between the surfaces. The plastic spreader should beto push on frontside of film in one direction toward the roll of film and outward toward the edge of the part,
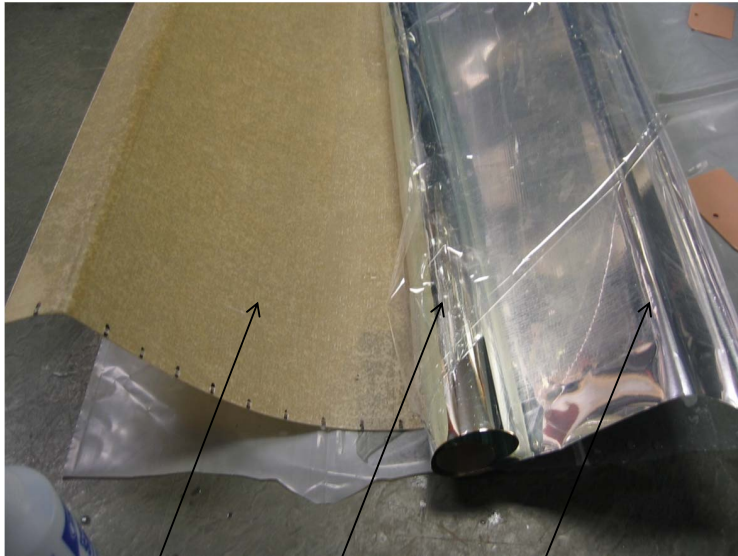
Clean Fiberglass part   Protective layer on sticky side of film (backside)   Mirror film with protective layer on front side (do not remove)

Figure B-1: Clean fiberglass part with mirror film for mounting shown.

always pushing bubbles toward the edge of the film and away from the sections that are already adhered to the fiberglass part. Once a full length section of the film is applied, the same spray followed by pushing out water over the film surface should continue for the remaining surface, each time only exposing a 5-10cm of adhesive (Figure B.1). Figure B.1 shows the final part with end sections attached, but with the frontside protective layer still intact until further assembly is complete.
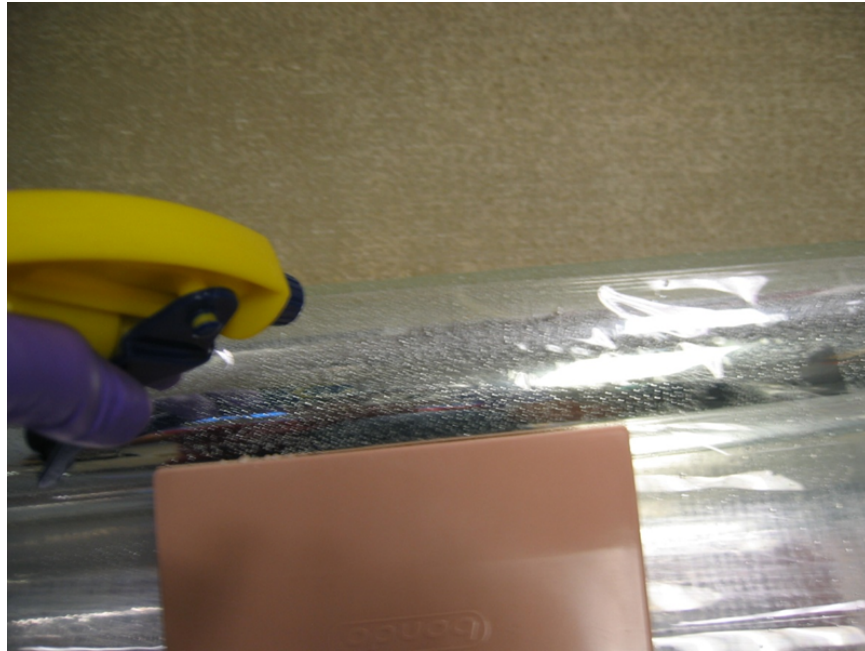
Figure B-2: Spray film and part
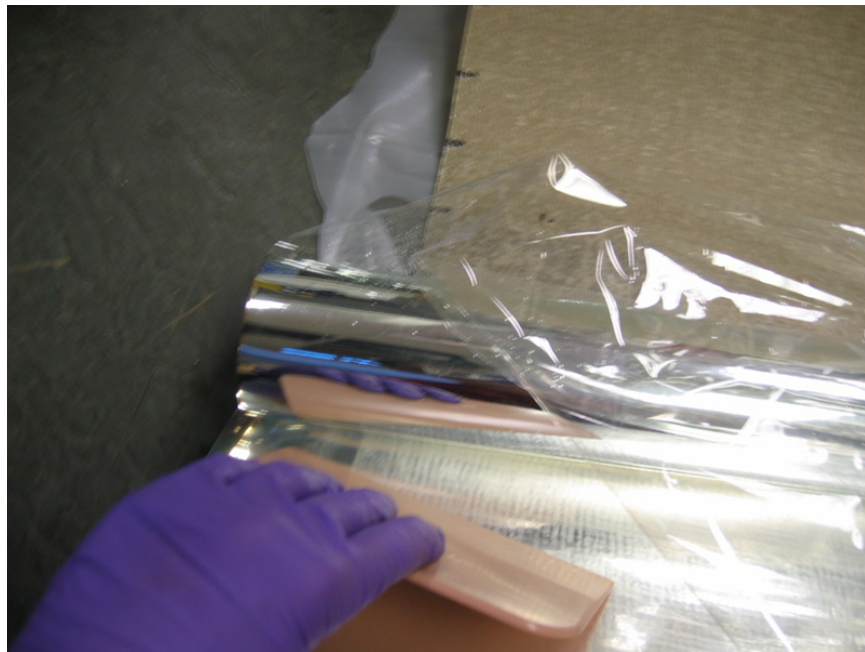
Figure B-3: Adhere with spreader

Figure B-4: Mirror film application with half of the film applied to the fiberglass part.
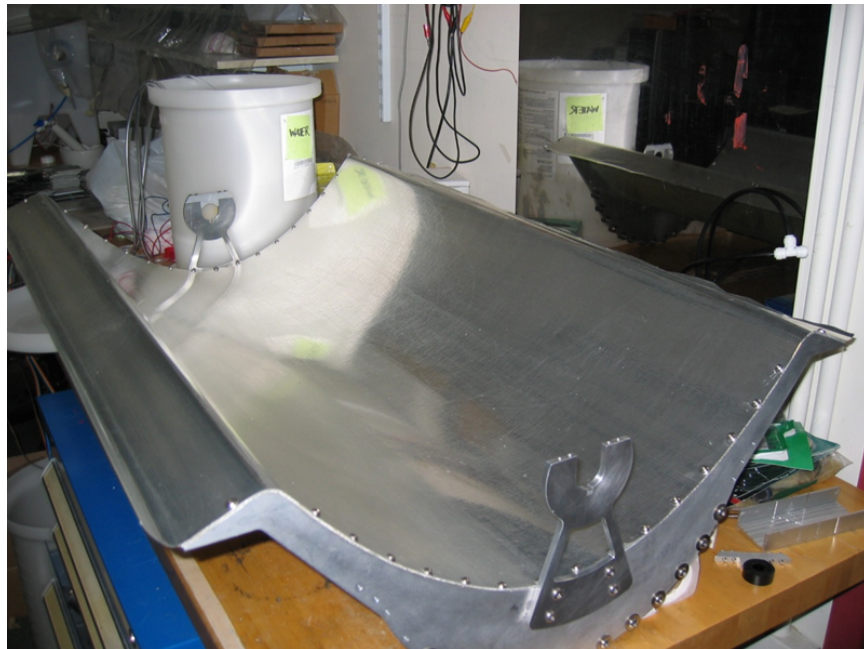
Figure B-5: Mirror film application on a monolithic fiberglass trough at 1:20 scale.

Appendix C

Test Dust and Quartz Specifications

Specification for the test dust and quartz is useful for comparing to the breakdown of contaminants in other locations.

C.1   Arizona Test Dust Specification Sheets

A detailed table of the ISO Medium Test Dust particle distrubution that was used in the contamination studies.

C.2   MIL SPEC Quartz Specification Sheets

Table C.1: ISO Medium Test Dust Particle Distribution Table

COULTER®   MULTISIZER AccuComp® 1.19

POWDER TECHNOLOGY, INC.

PTI
POWDER TECHNOLOGY INC.
14331 Ewing Avenue South   Burnsville, Minnesota 55306
Phone: 952-894-8737

Filename: 10571M.#01   Sample Number: 200
Group ID: 10571M
Sample ID: ISO 12103-1, A3 MEDIUM TEST DUST
Comment: SAE MEDIUM TEST DUST, NIST TRACEABLE
Operator: LHA
Electrolyte: ISOTON II
Dispersant: TYPE IC
Aperture Size: 280 µm   10571b.#01
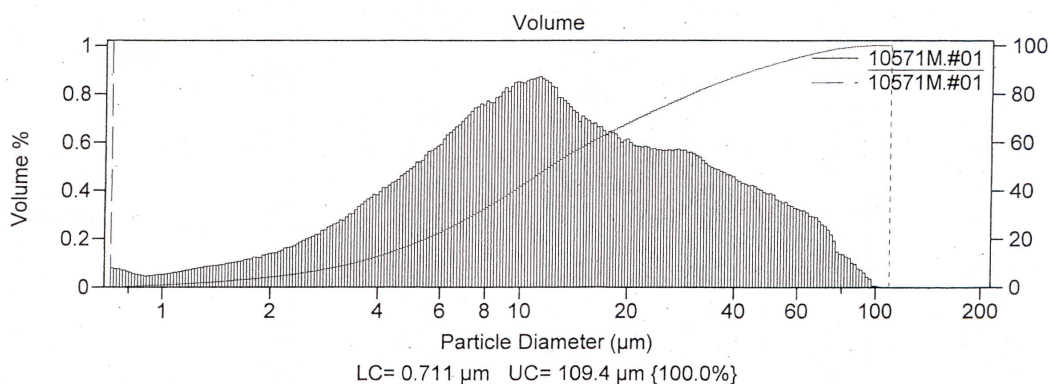   100 µm   10571b.#02
                   30 µm   10571b.#03
Acquired: 16:57 18 Mar 2010
Serial Number: 123
Edited size data

LC= 0.711 µm   UC= 109.4 µm {100.0%}

Volume Statistics (Geometric)   10571M.#01

Calculations from 0.711 µm to 109.4 µm

Volume	831.5e6 µm³		
Mean:	12.09 µm	S.D.:	20.2 µm
Median:	11.97 µm	Variance:	407 µm²
Mean/Median Ratio:	1.010		
Mode:	11.28 µm		
Spec. surf. area:	0.824 m²/ml		

% >	10	25	50	75	90
Size µm	45.02	25.17	11.97	6.406	3.409

Micron Size	Cumulative Volume % less than
1	1.0
2	4.2
3	8.2
4	12.9
5	17.9
7	28.0
10	42.2
20	68.2
40	87.4
80	99.1
120	100.0

Table C.2: ISO Medium Test Dust Particle Distribution Table (continued)

COULTER®   MULTISIZER AccuComp® 1.19

18 Mar 2010

———————— POWDER TECHNOLOGY, INC. ————————

10571M.#01

Channel Number	Particle Diameter μm	Diff Number %	Cum < Number %	Diff Volume %	Cum < Volume %
1	0.711	25.31	0	0.372	0
6	0.785	14.58	25.31	0.287	0.372
11	0.866	8.93	39.89	0.238	0.658
16	0.955	7.50	48.82	0.269	0.896
21	1.054	6.55	56.31	0.316	1.16
26	1.163	5.79	62.87	0.375	1.48
31	1.283	4.95	68.66	0.430	1.85
36	1.416	4.07	73.61	0.475	2.28
41	1.562	3.40	77.68	0.533	2.76
46	1.724	2.86	81.08	0.602	3.29
51	1.902	2.45	83.94	0.691	3.89
56	2.099	2.08	86.39	0.792	4.59
61	2.316	1.82	88.47	0.929	5.38
66	2.555	1.58	90.29	1.08	6.31
71	2.819	1.37	91.87	1.26	7.39
76	3.110	1.17	93.24	1.45	8.65
81	3.432	1.03	94.41	1.72	10.10
86	3.786	0.871	95.45	1.94	11.82
91	4.178	0.718	96.32	2.15	13.76
96	4.610	0.596	97.04	2.40	15.91
101	5.086	0.494	97.63	2.67	18.31
106	5.612	0.403	98.13	2.93	20.98
111	6.192	0.335	98.53	3.26	23.90
116	6.832	0.273	98.86	3.57	27.16
121	7.538	0.216	99.14	3.79	30.73
126	8.317	0.168	99.35	3.97	34.53
131	9.176	0.132	99.52	4.18	38.50
136	10.12	0.101	99.65	4.29	42.68
141	11.17	0.075	99.75	4.27	46.97
146	12.33	0.051	99.83	3.93	51.23
151	13.60	0.035	99.88	3.59	55.16
156	15.01	0.025	99.91	3.40	58.75
161	16.56	0.017	99.94	3.23	62.15
166	18.27	0.012	99.96	3.07	65.38
171	20.16	0.009	99.97	2.93	68.45
176	22.24	0.006	99.98	2.88	71.39
181	24.54	0.005	99.98	2.83	74.27
186	27.07	0.003	99.99	2.83	77.10
191	29.87	0.002	99.99	2.72	79.93
196	32.96	0.002	99.99	2.49	82.65
201	36.37	0.001	100.00	2.34	85.14
206	40.12	0.001	100.00	2.16	87.48
211	44.27	0.001	100.00	2.04	89.64
216	48.85	0.0039	100.00	1.88	91.68
221	53.90	0.0027	100.00	1.70	93.56
226	59.47	0.0018	100.00	1.56	95.26
231	65.61	0.0012	100.00	1.37	96.82
236	72.40	6.1E-5	100.00	0.932	98.19
241	79.88	2.8E-5	100.00	0.580	99.12

Table C.3: MIL E-5007C Quartz specifications for etching tests

Specified Size (µm)	Test Sieve Designation	Specified Range (% Of Total Less Than by Weight)
1000	USA 18 mesh	100
900	Electroformed	$98.0 - 99.0$
600	USA 30 mesh	$93.0 - 97.0$
400	ATM 48 mesh	$82.0 - 86.0$
200	ATM 88 mesh	$46.0 - 50.0$
125	USA 120 mesh	$18.0 - 22.0$
75	USA 200 mesh	$3.0 - 7.0$

Appendix D

Additional Flow Simulation Results

In addition to the images shown in the main section of Chapter 7, images of flow for all six vortex generator shapes are shown for flow at 5m/s in air.

D.1 Flow Simulations for Six Vortex Generator Profiles

In order to evaluate the relative flow length and vertical lift resulting from vortex generator shapes, six concepts with the same maximum part height, length and width, as well as V-angle were simulated in the SolidWorks flow simulation package. Flow simulation parameters are for air at 5m/s. Overall part height is 20mm, part width is 40mm and length is 40mm. See the main section of Chapter 7 for additional simulation details. In the front and side views, a grid with 20mm spacing allows for comparison with the other designs for flow height and spread. The scale of the flow velocity shown in the upper right of the images, is consistent between all views and between all shapes.

VG1: Vortex generator one is the simplest shape of the vortex generators, with a purely extruded part shape that is orthogonal to the desired cleaning surface. Fig-
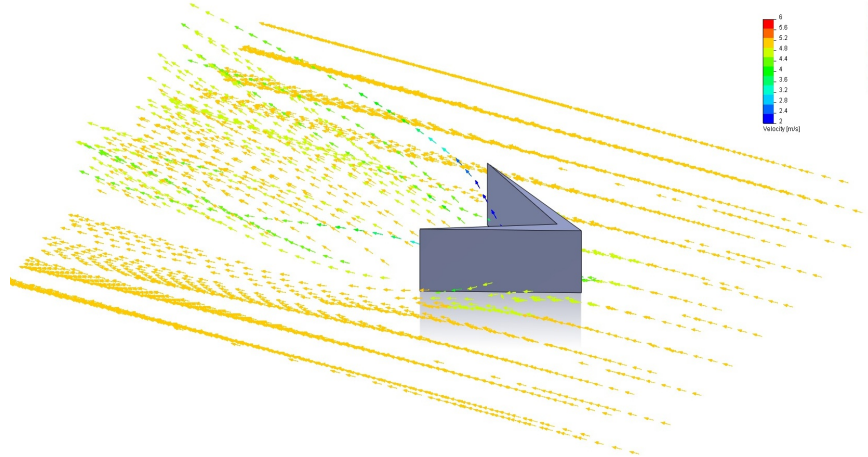
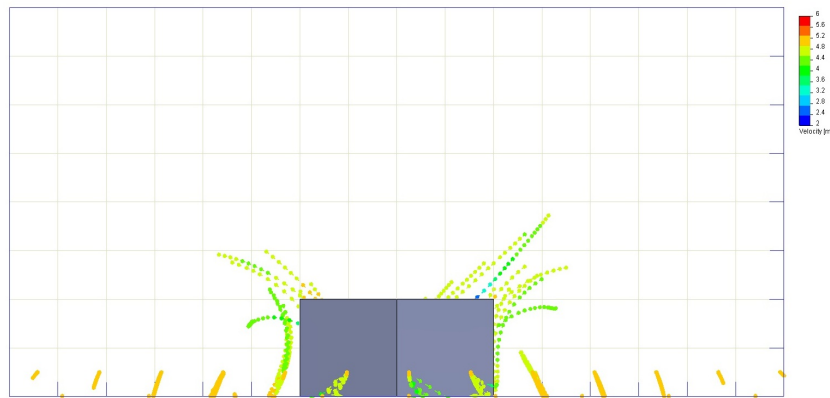Figure D-1: Vortex generator shape 1 with airflow at 5m/s. Isometric View

Figure D-2: Vortex generator shape 1 with airflow at 5m/s. Front View

ure D.1 to Figure D.1 shows the flow in isometric, front and side perspectives.

VG2: Vortex generator two is the equivalent to shape one except with a linear slope from the front edge down to the rear points of the shape. Figure D.1 to Figure D.1 shows this shape in more detail, with the flow around the form.

VG3: Vortex generator three is the equivalent to shape one except with a inner curved slope from the front edge down to the rear points of the shape. Figure D.1 to Figure D.1 shows this shape in more detail, with the flow around the form.

VG4: Vortex generator four is the equivalent to shape one except with an outer convex slope from the front edge down to the rear points of the shape. Figure D.1 to Figure D.1 shows this shape in more detail, with the flow around the form.
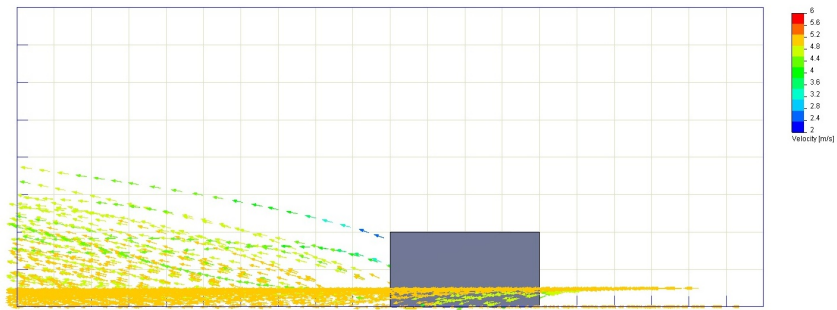
Figure D-3: Vortex generator shape 1 with airflow at 5m/s. Side View
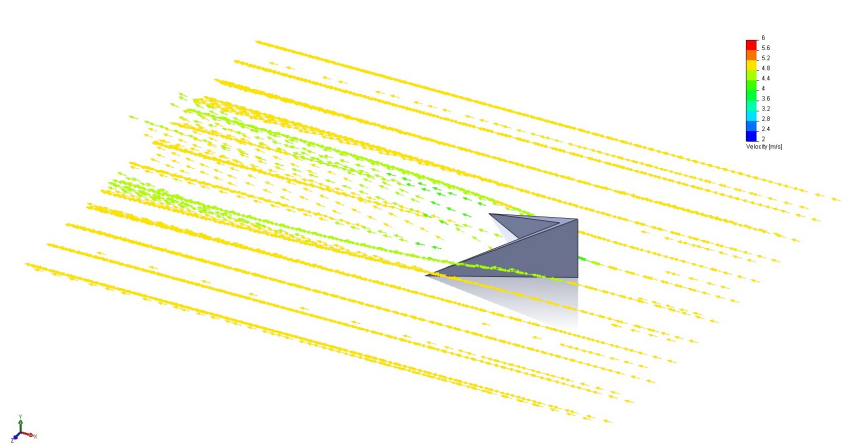

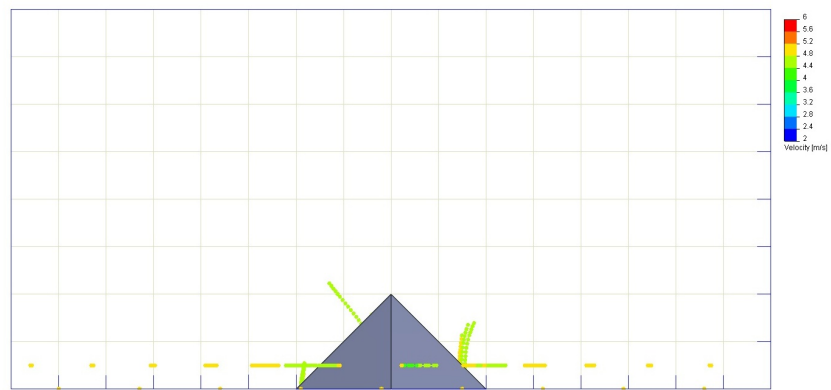Figure D-4: Vortex generator shape 2 with airflow at 5m/s. Isometric View

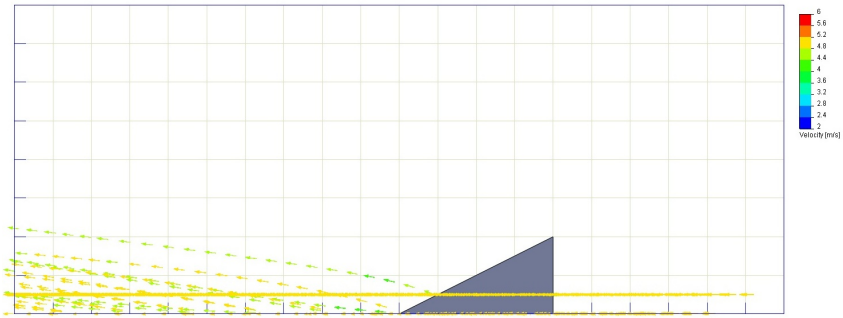Figure D-5: Vortex generator shape 2 with airflow at 5m/s. Front View

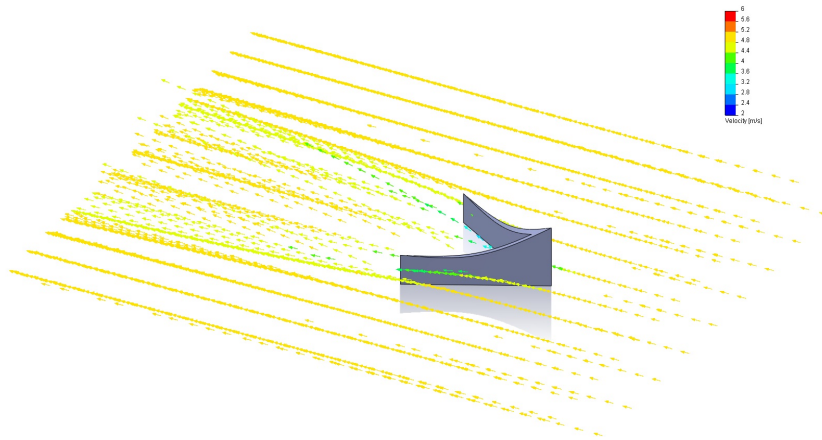Figure D-6: Vortex generator shape 2 with airflow at 5m/s. Side View

Figure D-7: Vortex generator shape 3 with airflow at 5m/s. Isometric View

Figure D-8: Vortex generator shape 3 with airflow at 5m/s. Front View

Figure D-9: Vortex generator shape 3 with airflow at 5m/s. Side View

Figure D-10: Vortex generator shape 4 with airflow at 5m/s. Isometric View
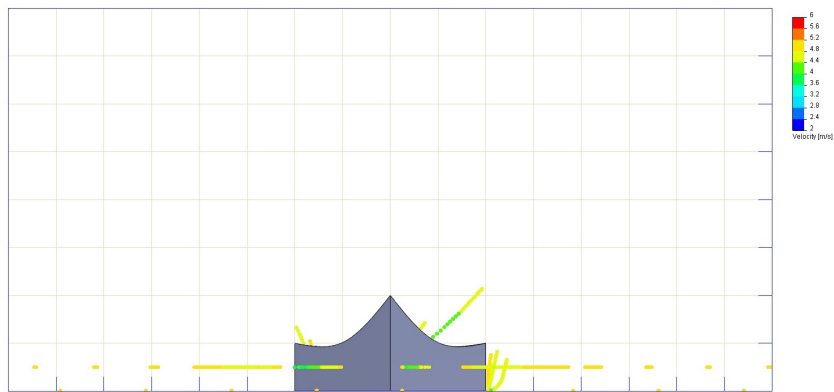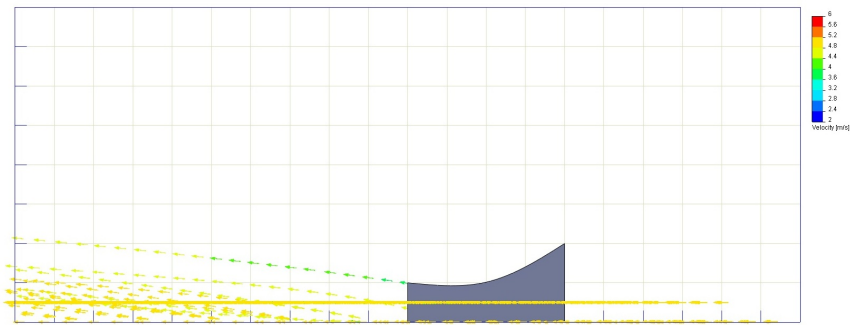

Figure D-11: Vortex generator shape 4 with airflow at 5m/s. Front View

Figure D-12: Vortex generator shape 4 with airflow at 5m/s. Side View
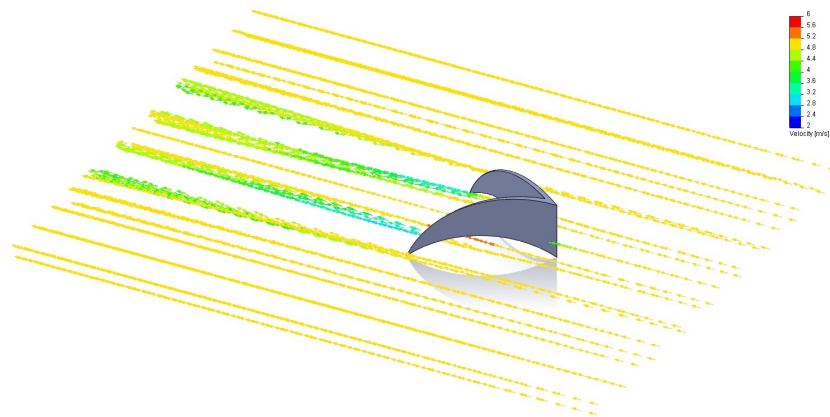
Figure D-13: Vortex generator shape 5 with airflow at 5m/s. Isometric View

VG5: Vortex generator five is the equivalent to shape four with an outer convex slope from the front edge down to the rear points of the shape, with the addition of a curved section removed from the lower fin area. Figure D.1 to Figure D.1 shows this shape in more detail, with the flow around the form.

VG6: Vortex generator six is the equivalent to shape one with extruded bulk form, except that a straight section removed from the front of thelower fin area. Figure D.1 to Figure D.1 shows this shape in more detail, with the flow around the form.

Figure D-14: Vortex generator shape 5 with airflow at 5m/s. Front View

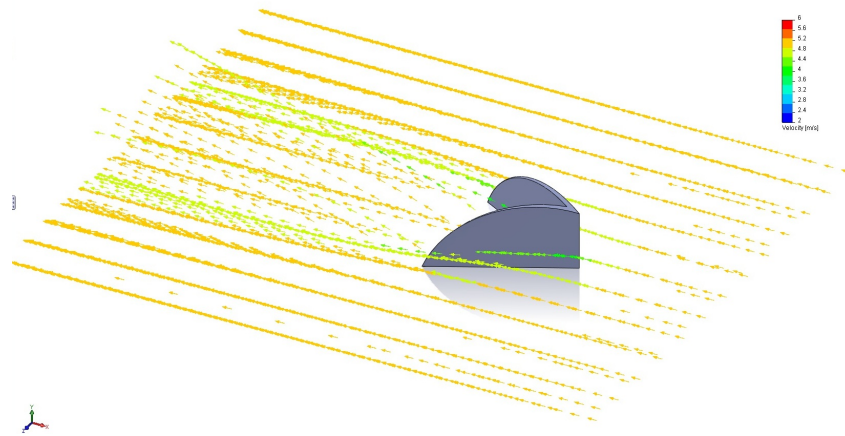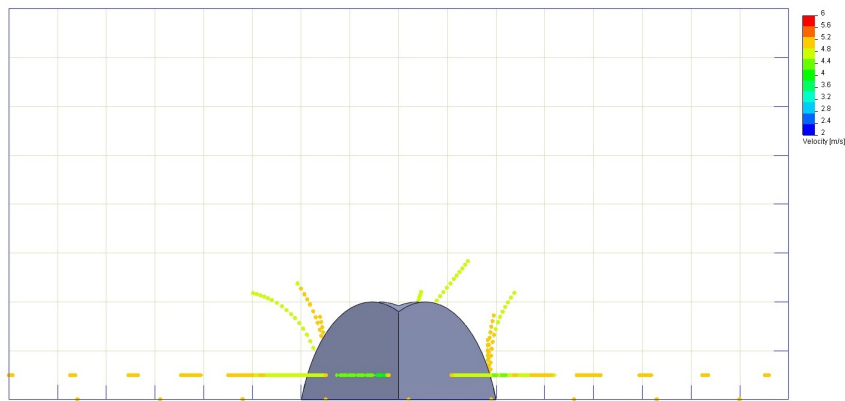Figure D-15: Vortex generator shape 5 with airflow at 5m/s. Side View

Figure D-16: Vortex generator shape 6 with airflow at 5m/s. Isometric View

Figure D-17: Vortex generator shape 6 with airflow at 5m/s. Front View
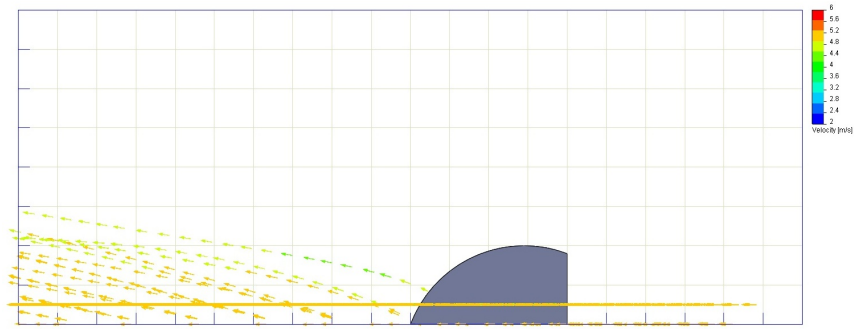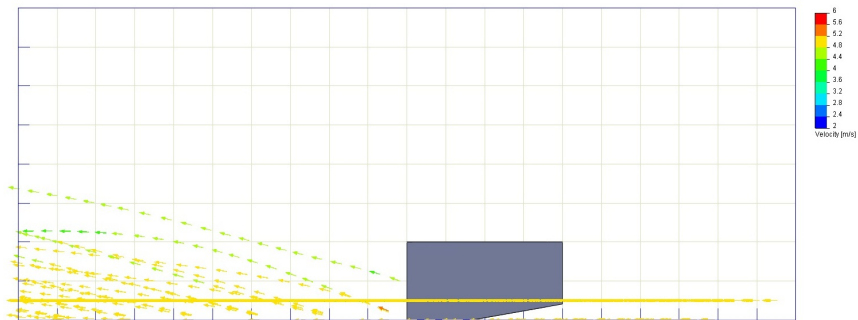

Figure D-18: Vortex generator shape 6 with airflow at 5m/s. Side View
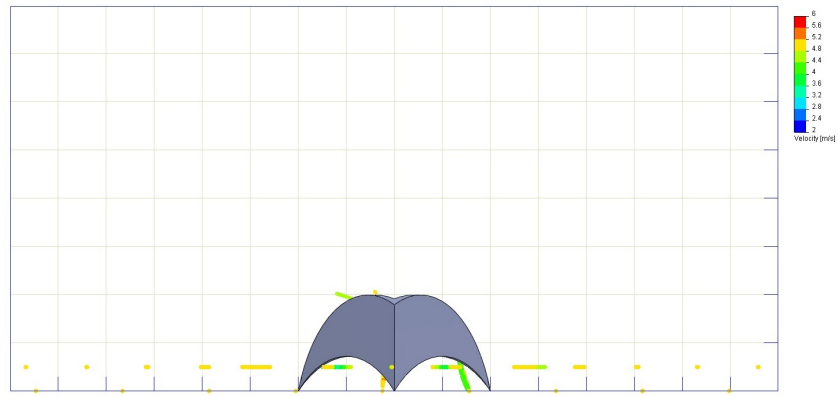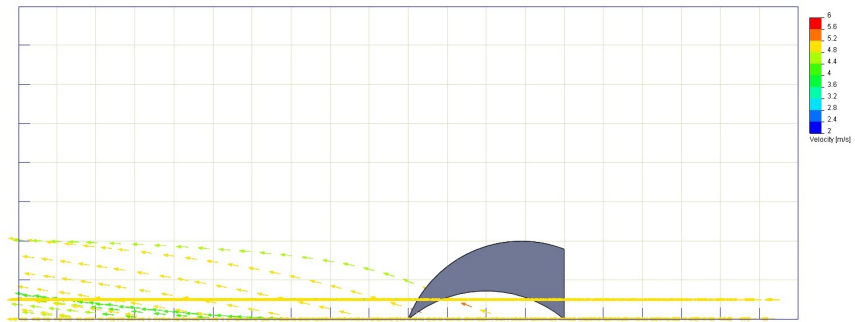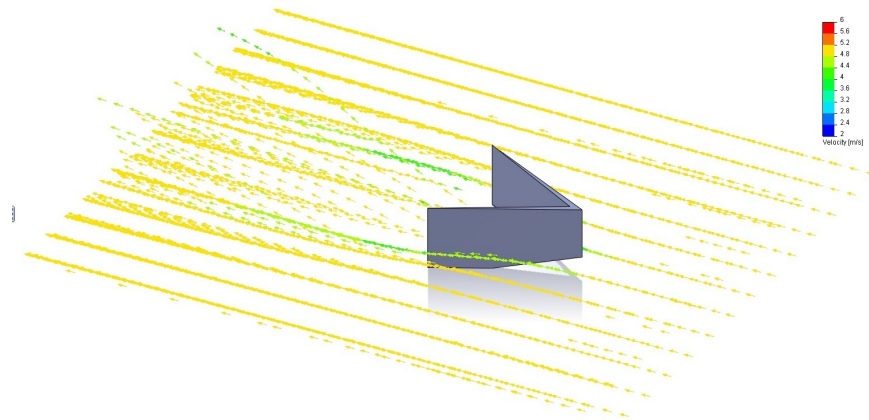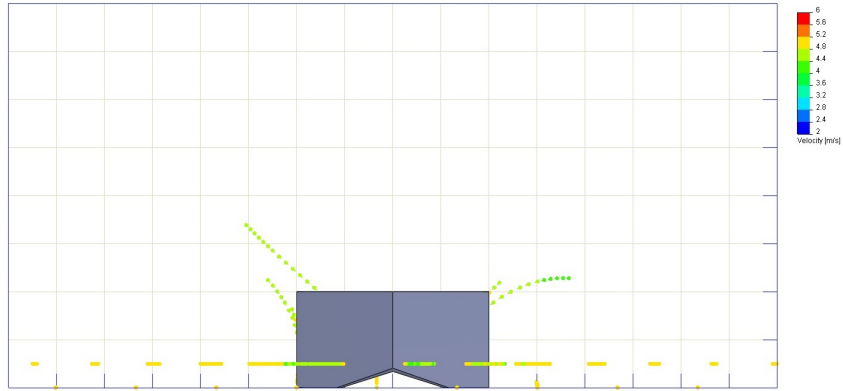
Bibliography

[1] (Energy Information Administration) EIA. 2007.

[2] R. Pitz-Paal, J. Dersch, B. Milow, F. Tellez, A. Ferriere, U. Langnickel, A. Steinfeld, J. Karni, E. Zarza, and O. Popel. Development steps for parabolic trough solar power technologies with maximum impact on cost reduction. *Journal of Solar Energy Engineering-Transactions of the ASME*, 129(4):371–377, 2007.

[3] G. N. Tiwari. *Solar energy : fundamentals, design, modelling and applications.* CRC Press ; Narosa Pub. House, Boca Raton, FL New Delhi, 2002.

[4] Kiehl and Trenberth. Earth's energy budget, 1997. `http://asd-www.larc.nasa.gov/SCOOL/budget.jpg`.

[5] SWERA. Solar and wind energy resource assessment (swera) dni resource maps, 2008. `http://swera.unep.net/index.php?id=solar\&no_cache=1`.

[6] Sol Wieder. *An introduction to solar energy for scientists and engineers.* Wiley, New York, 1982. Sol Wieder. ill. ; 25 cm.

[7] Soteris Kalogirou. *Solar energy engineering: processes and systems.* Elsevier/Academic Press, Burlington, MA, 2009.

[8] Abengoa. Operating scheme for parabolic trough technology. `http://www.abengoasolar.com/corp/web/en/technologies/concentrated_solar_power/parabolic_trough/index.html`.

[9] Stirling Engine Systems. Stirling dish. `http://i.i.com.com/cnwk.1d/i/ne/p/2008/StirlingDishes_500x359.jpg`.

[10] Ausra. Ausra frenel reflector. `http://www.ausra.com/technology/`.

[11] Geyer. From research to csp market introduction, March 2007. Trough Workshop `http://www.nrel.gov/csp/troughnet/pdfs/2007/geyer_international_market_overview.pdf`.

[12] NREL. U.s. parabolic trough power plant data. `http://www.nrel.gov/csp/troughnet/power_plant_data.html`.

[13] Sopogy. www.sopogy.com.

[14] Schott Solar. Schott ptr 70 receiver. `http://www.schottsolar.com/global/products/concentrated-solar-power/schott-ptr-70-receiver/`.

[15] Reflectech Mirror Film. Technical specifications. `http://www.reflectechsolar.com/technical.html`.

[16] H. M. Guven and R. B. Bannerot. Derivation of universal error parameters for comprehensive optical analysis of parabolic troughs. *Journal of Solar Energy Engineering*, 108(4):275–281, 1986.

[17] W.W. Shaner and H.S. Wilson. Cost of paraboloidal collectors for solar to thermal electric conversion. *Solar Energy*, 17(6):351–358, 1975.

[18] Sargent & Lundy LLC Consulting Group. Assessment of parabolic trough and power tower solar technology cost and performance forecasts, 2003.

[19] E.L. Ralph. Large scale solar electric power generation. *Solar Energy*, 14(1):11–20, 1972/12 1972.

[20] J. P. Reichling and F. A. Kulacki. Utility scale hybrid wind-solar thermal electrical generation: A case study for minnesota. *Energy*, 33(4):626–638, 2008.

[21] U. Minzer, D. Barnea, and Y. Taitel. Flow rate distribution in evaporating parallel pipes - modeling and experimental. *Chemical Engineering Science*, 61(22):7249–7259, Nov 2006.

[22] Raymond K. Cohen and Nevin K. Hiester. A survey of solar furnace installations in the united states. *Solar Energy*, 1(2-3):115–116, 1957/0 1957.

[23] Irene Henriques and Perry Sadorsky. Oil prices and the stock prices of alternative energy companies. *Energy Economics*, 30(3):998–1010, 2008.

[24] C. J. Winter. High-temperature solar-energy utilization after 15 years research-and-development - kick-off for the 3rd generation of technologies. *Solar Energy Materials*, 24(1-4):26–39, Dec 1991.

[25] United States. Congress. Office of Technology Assessment. *Application of solar technology to today's energy needs.* Congress of the United States, Office of Technology Assessment : for sale by the Supt. of Docs., U.S. Govt. Print. Off., Washington, 1978.

[26] F. Trieb. Competitive solar thermal power stations until 2010 - the challenge of market introduction. *Renewable Energy*, 19(1-2):163–171, Jan-Feb 2000.

[27] D. Mills. Advances in solar thermal electricity technology. *Solar Energy*, 76(1-3):19–31, 2004.

[28] E. Lupfert, K. Pottler, S. Ulmer, K. J. Riffelmann, A. Neumann, and B. Schiricke. Parabolic trough optical performance analysis techniques. *Journal of Solar Energy Engineering-Transactions of the Asme*, 129(2):147–152, May 2007.

[29] Peter Schwarzboezl, Reiner Buck, Chemi Sugarmen, Arik Ring, M. Jesas Marcos Crespo, Peter Altwegg, and Juan Enrile. Solar gas turbine systems: Design, cost and perspectives. *Solar Energy*, 80(10):1231–1240, 2006.

[30] Frank P. Incropera and David P. DeWitt. *Fundamentals of heat and mass transfer.* Wiley, New York, 5th edition, 2002.

[31] Robert O. Hughes. Effects of tracking errors on the performance of point focusing solar collectors. *Solar Energy*, 24(1):83–92, 1980.

[32] G. C. Bakos. Design and construction of a two-axis sun tracking system for parabolic trough collector (ptc) efficiency improvement. *Renewable Energy*, 31(15):2411–2421, 2006.

[33] A. V. Arasu and T. Sornakumar. Design, development and performance studies of embedded electronic controlled one axis solar tracking system. *Asian Journal of Control*, 9(2):163–169, 2007.

[34] G. C. Bakos, I. Ioannidis, N. F. Tsagas, and I. Seftelis. Design, optimisation and conversion-efficiency determination of a line-focus parabolic-trough solar-collector (ptc). *Applied Energy*, 68(1):43–50, 2001.

[35] W. S. Duff and G. F. Lameiro. Parametric performance and cost models for solar concentrators. *Solar Energy*, 17(1):47–58, 1975/4 1975.

[36] C. L. Bennett. Optimal heat collection element shapes for parabolic trough concentrators. *Journal of Solar Energy Engineering-Transactions of the Asme*, 130(2):–, May 2008.

[37] M. E. Van Valkenburg, R. L. Vaughn, M. Williams, and J. S. Wilkes. Thermochemistry of ionic liquid heat-transfer fluids. *Thermochimica Acta*, 425(1-2):181–188, Jan 20 2005.

[38] L. Moens, D. M. Blake, D. L. Rudnicki, and M. J. Hale. Advanced thermal storage fluids for solar parabolic trough systems. *Journal of Solar Energy Engineering-Transactions of the Asme*, 125(1):112–116, Feb 2003.

[39] M. Li and L. L. Wang. Investigation of evacuated tube heated by solar trough concentrating system. *Energy Conversion and Management*, 47(20):3591–3601, Dec 2006.

[40] D. Kearney, U. Herrmann, P. Nava, P. Kelly, R. Mahoney, J. Pacheco, R. Cable, N. Potrovitza, D. Blake, and H. Price. Assessment of a molten salt heat transfer fluid in a parabolic trough solar field. *Journal of Solar Energy Engineering-Transactions of the Asme*, 125(2):170–176, 2003.

[41] D. Feuermann and J. M. Gordon. Analysis of a 2-stage linear fresnel reflector solar concentrator. *Journal of Solar Energy Engineering-Transactions of the ASME*, 113(4):272–279, Nov 1991.

[42] CIEMAT, CRES, DLR, FICHTNER Solar, FLABEG Solar, INABENSA (co-ordinator), and SBP. Development of a low cost european parabolic trough collector eurotrough. Technical Report Contract: JOR3-CT98-0231, 2001.

[43] K. J. Riffelmann, A. Neumann, and S. Ulmer. Performance enhancement of parabolic trough collectors by solar flux measurement in the focal region. *Solar Energy*, 80(10):1303–1313, 2006.

[44] Eckhard Lupfert, Klaus Pottler, Steffen Ulmer, Klaus-J. Riffelmann, Andreas Neumann, and Bjorn Schiricke. Parabolic trough optical performance analysis techniques. *Journal of Solar Energy Engineering*, 129(2):147–152, 2007.

[45] A. V. Arasu and S. T. Sornakumar. Theoretical analysis and experimental verification of parabolic trough solar collector with hot water generation system. *Thermal Science*, 11(1):119–126, 2007.

[46] A. V. Arasu and T. Sornakumar. Design, manufacture and testing of fiberglass reinforced parabola trough for parabolic trough solar collectors. *Solar Energy*, 81(10):1273–1279, 2007.

[47] A. V. Arasu and T. Sornakumar. Life cycle cost analysis of new frp based solar parabolic trough collector hot water generation system. *Journal of Zhejiang University-Science A*, 9(3):416–422, 2008.

[48] G. Helsch, M. Krzyzak, G. Heide, and G. H. Frischat. Adherent antireflection coatings on borosilicate glass for solar collectors. *Glass Technology-European Journal of Glass Science and Technology Part A*, 47(5):153–156, 2006.

[49] Flabeg. Flabeg solar leading glass technology. `http://www.flabeg.com/index.php?id=103`.

[50] I. Martinez, R. Almanza, M. Mazari, and G. Correa. Parabolic trough reflector manufactured with aluminum first surface mirrors thermally sagged. *Solar Energy Materials and Solar Cells*, 64(1):85–96, Sep 1 2000.

[51] H. Tabor and H. Zeimer. Low-cost focussing collector for solar power units. *Solar Energy*, 6(2):55–59, 1962.

[52] G. M. Giannuzzi, C. E. Majorana, A. Miliozzi, V. A. Salomoni, and D. Nicolini. Structural design criteria for steel components of parabolic-trough solar concentrators. *Journal of Solar Energy Engineering-Transactions of the Asme*, 129(4):382–390, 2007.

[53] Paul B. Archibald. A method for manufacturing parabolic mirrors. *Solar Energy*, 1(2-3):102–103, 1957.

[54] M. Srinivasan, L. V. Kulkarni, and C. S. Pasupathy. A simple technique of fabrication of paraboloidal concentrators. *Solar Energy*, 22(5):463–465, 1979.

[55] N. Hosoya, J.A. Peterka, R.C. Gee, and D. Kearney. Wind tunnel test of parabolic trough solar collectors. Technical report, 2008.

[56] American Society of Civil Engineers and Structural Engineering Institute. *Minimum design loads for buildings and other structures*. American Society of Civil Engineers, Structural Engineering Institute, Reston, Va., special edition, 2003.

[57] D. E. Randall, R. E. Tate, and D. A. Powers. Experimental results of pitching moment tests on parabolic-trough solar-collector array configurations. *Journal of Solar Energy Engineering-Transactions of the Asme*, 106(2):223–230, 1984. t:3.

[58] N. Naeeni and M. Yaghoubi. Analysis of wind flow around a parabolic collector (1) fluid flow. *Renewable Energy*, 32(11):1898–1916, Sep 2007.

[59] D. E. Randall, D. D. Mcbride, and R. E. Tate. Mean wind loading on parabolic-trough solar collectors. *Journal of Solar Energy Engineering-Transactions of the ASME*, 103(4):313–322, 1981.

[60] Wright Brothers Wind Tunnel. *Wright Brothers Wind Tunnel; information for use by industry.* M.I.T., [Cambridge, Mass.], rev., oct. 1947. edition, 1947. illus. 28 cm.

[61] Jewel B. Barlow, William H. Rae, Alan Pope, and Alan Pope. *Low-speed wind tunnel testing.* Wiley, New York, 3rd edition, 1999.

[62] J.R. Markham. The m.i.t. wright brothers wind tunnel and its operating equipment. *S.A.E. transactions*, 49(3):380–388, 1941.

[63] Eugene E. Covert. A student's introduction to the wright brothers wind tunnel at mit, July 2004 2004.

[64] C. E. Kennedy and K. Terwilliger. Optical durability of candidate solar reflectors. *Journal of Solar Energy Engineering-Transactions of the Asme*, 127(2):262–269, May 2005.

[65] A. H. Slocum. *Precision machine design.* Prentice Hall, Englewood Cliffs, N.J., 1992.

[66] Sheldon K. Friedlander. *Smoke, dust, and haze : fundamentals of aerosol dynamics.* Oxford University Press, New York, 2nd edition, 2000.

[67] William C. Hinds. *Aerosol technology : properties, behavior, and measurement of airborne particles.* Wiley, New York, 2nd edition, 1999.

[68] Frank M. White. *Fluid mechanics.* WCB/McGraw-Hill, Boston, Mass., 4th edition, 1999.

[69] Rajiv Kohli and K. L. Mittal. Developments in surface contamination and cleaning - fundamentals and applied aspects. William Andrew Publishing, 2007.

[70] V. Adrian Parsegian. *Van der Waals forces : a handbook for biologists, chemists, engineers, and physicists.* Cambridge University Press, New York, 2006.

[71] J. N. Israelachvili. *Intermolecular and surface forces.* Academic Press, Burlington, MA, 3rd edition, 2011.

[72] Stellarnet. Detector technical specifications. `http://www.stellarnet-inc.com/`.

[73] Forbes. Energy recovery, 2008. `http://www.forbes.com/technology/2008/05/08/mitra-energy-recovery-tech-science-cx_sm_0509mitra.html`.

[74] R. Sherman, J. Grob, and W. Whitlock. Dry surface cleaning using co2 snow. *Journal of Vacuum Science & Technology B*, 9(4):1970–1977, Jul-Aug 1991.

[75] R. Sherman. Carbon dioxide snow cleaning. *Particulate Science and Technology*, 25(1):37–57, Jan-Feb 2007.

[76] M. Corn and F. Stein. Re-entrainment of particles from a plane surface. *American Industrial Hygiene Association Journal*, 26(4):325–&, 1965.

[77] G. A. Landis. Dust obscuration of mars solar arrays. *Acta Astronautica*, 38(11):885–891, Jun 1996.

[78] G. A. Landis. Mars dust-removal technology. *Journal of Propulsion and Power*, 14(1):126–128, Jan-Feb 1998.

[79] Vaupell Rapid Prototyping. Stereolithography resin. `http://www.vaupell.com/stereolithography-sla`.